Title

Monotonic and Cyclic Resistance of MICP Cemented Silica and Carbonate Sands

Author

Blair, Benjamin E

Publication Date

2024

Peer reviewed|Thesis/dissertation

Monotonic and Cyclic Resistance of MICP Cemented Silica and Carbonate Sands

By

BENJAMIN EMMETT BLAIR

THESIS

Submitted in partial satisfaction of the requirements for the degree of

MASTER OF SCIENCE

in

Civil and Environmental Engineering

in the

OFFICE OF GRADUATE STUDIES

of the

UNIVERSITY OF CALIFORNIA

DAVIS

Approved:

_____

Jason T. DeJong, Chair

_____

Katerina Ziotopoulou

_____

Michael H. Gardner

Committee in Charge

2024

Monotonic and Cyclic Resistance of MICP Cemented Silica and Carbonate Sands

ABSTRACT

Earthquake-induced cyclic loading poses a concern to infrastructure founded on liquefiable soils, often resulting in severe damage like foundation bearing failure and lateral spreading. To mitigate these risks, ground improvement methods can be implemented to increase the soil's resistance to liquefaction triggering and thus any ensuing deformations. This research investigates the behavior of biocemented soils using a triaxial device, focusing on how monotonic and cyclic responses change with varying levels of Microbially Induced Calcite Precipitation (MICP) treatment, soil composition, and loading conditions. Previous studies have explored MICP at different scales, but few have utilized triaxial testing, which offers control over stress conditions and allows for localized specimen response. This study builds on prior work by conducting twenty-one monotonic and twenty-nine cyclic tests on carbonate and silica sands, with mixed sands also tested to examine the influence of carbonate content. The results indicate that MICP treatment enhances cyclic resistance significantly, with shear wave velocity measurements providing novel insights into fabric changes. Uncemented specimens behaved as expected, showing rapid pore water pressure generation and liquefaction triggering, while cemented specimens exhibited increased strength and stiffness, particularly under cyclic loading. The findings suggest that MICP treatment is more effective for improving cyclic resistance than monotonic strength, underscoring its potential as a method for liquefaction mitigation.

ACKNOWLEDGMENTS

First and foremost, I would like to express my deepest gratitude to my advisor and thesis chair, Jason T. DeJong, for his unwavering support and guidance throughout this process. His mentorship has been instrumental in my professional development. I would also like to extend my thanks to the rest of my thesis committee: Katerina Ziotopoulou and Michael Gardner, for their invaluable instruction in my courses and their insightful feedback on my research.

This work would not have been possible without the assistance of Alexandra San Pablo, who mentored me on the chemical, biological, and geotechnical ground improvement method known as MICP. My time working with Dr. San Pablo on centrifuge experiments greatly contributed to my growth and understanding in this field. Additionally, I would like to thank Charles Graddy for his microbiology expertise and his skill in overcoming research challenges.

I would like to extend my gratitude to my colleagues at the University of Washington, Professor Michael Gomez and Bruna Ribeiro, for graciously hosting me at their research facility and for generously sharing their expertise and procedures in performing MICP.

To all my colleagues at UC Davis: I am grateful for the friendship, insightful discussions, and unwavering support in the lab during our experiments. I feel honored to be part of the Center for Biomediated Bioinspired Geotechnics community.

The presented study involves work supported by the Engineering Research Center Program of the National Science Foundation under NSF Cooperative Agreement No. EEC-1449501. Any opinions, findings, conclusions, or recommendations expressed in this manuscript are those of the authors and do not necessarily reflect the views of the National Science Foundation.

TABLE OF CONTENTS

LIST OF TABLES

LIST OF FIGURES

INTRODUCTION

Earthquake-induced cyclic loading poses a concern to infrastructure on liquefiable soils, often resulting in severe damage including foundation-bearing failure and lateral spreading. To mitigate these risks, ground improvement methods can be implemented to increase the soil's resistance to liquefaction triggering and induced deformations. However, most current methods, such as deep soil mixing, vibratory compaction, and pressure grouting, require large amounts of materials (i.e., Portland cement) and energy, leading to significant greenhouse gas emissions (GHG) (Karol 2003; DeJong et al. 2010; de Melo et al. 2023). Growing concerns regarding GHG emissions motivated researchers in the field of biogeotechnics to develop various biomediated techniques to replace or improve current geotechnical ground improvement methods (DeJong et al. 2017; Lu and Mitchell 2019; Faruqi 2023). Microbial induced calcite precipitation (MICP) is a biomediated ground improvement technique that uses the ureolytic properties of bacteria to precipitate calcium carbonate and cement the surrounding soil (DeJong et al. 2022). Prior research has shown that MICP increases resistance to liquefaction triggering and reduces consequences if liquefaction triggering occurs (Darby et al. 2019; Lee et al. 2021; Kortbawi 2022; San Pablo 2024). A comprehensive review of MICP as a ground improvement technology, including issues related to upscaling, have been discussed by DeJong et al. (2022).

MICP Treatment Process

MICP uses microorganisms, *Sporosarcina pasteurii* (*S. pasteurii*, ATCC 11859), capable of ureolytic activity to hydrolyze urea and produce carbonate ions, thus achieving biocementation (Stocks-Fischer et al. 1999; Fujita et al. 2008; San Pablo et al. 2020). Super-saturated conditions, which occur when carbonate ions are in the presence of calcium ions, trigger the precipitation of calcium carbonate solids. In laboratory scale studies, MICP treatment has often been executed

through augmentation, wherein the *S. Pasteurii* are injected into the specimen. This is followed by treating the soil specimen with a solution containing both urea and calcium ions; the bacteria degrade the urea, and the resulting solution precipitates calcium carbonate. Specimens treated with MICP will hereafter be referred to as biocemented or cemented specimens.

DeJong et al. (2010) proposed that calcium carbonate precipitation alters conditions of the soil matrix through three mechanisms: *bridging*, where the soil particles are cemented together; *coating*, where cementation bonds to the outside of the particle; and *infilling*, where the precipitate fills the voids. Of these, infilling is believed to be the least prevalent as the permeability remains relatively unchanged, typically within one order of magnitude for moderately cemented sands (Gomez and DeJong 2017; Montoya et al. 2021; Baek et al. 2022).

Microstructure studies using scanning electron microscopes (SEM) have evaluated the precipitated mineralogy and crystal formations in biocemented specimens (DeJong et al. 2022). These studies have shown that the precipitates primarily form calcite, with lesser amounts of vaterite, aragonite, and amorphous calcium carbonate (Nafisi et al. 2018; Burdalski and Gomez 2020; Burdalski 2020). For this paper, calcite will be used to generically describe calcium carbonate precipitation as it is the most common.

MICP Treatment Metrics

Calcite content (C_C) and shear wave velocity (V_s) measurements are the primary metrics used to evaluate the magnitude and effectiveness of the calcite precipitate (Kortbawi 2022). Shear wave velocity measurements are non-destructive and can be used to monitor the level of cementation throughout the treatment process. Shear wave velocity is calculated using:

$$V_s = \frac{L}{t} \tag{1}$$

where L is the distance of propagation and t is the travel time of the wave. In contrast, measuring calcite content requires a soil sample and can only be performed destructively post-completion of specimen testing. Calcite content is the percent mass of calcium carbonate (m_c) in the total sample mass (m_s):

$$C_c = \frac{m_c}{m_s} * 100\% \quad (2)$$

Shear wave velocity, which depends on the soil stiffness and increases with cementation, has been confirmed as an effective indicator for calcite content in multiple studies (Darby et al. 2019; Lee et al. 2021; Kortbawi 2022; Na et al., 2023; DeJong et al. 2022; San Pablo 2024). The V_s is directly related to the shear modulus of the small strain stiffness (G_{max}):

$$\mathrm{G_{max}} = \rho V s^2 \quad (3)$$

where ρ is the bulk soil density (Montoya and DeJong 2015). Since G_{max} is sensitive to the stress state of the specimen, it is common to normalize the small strain stiffness by the mean effective stress (p'):

$$\mathrm{G_{max}}/(\mathrm{P_a p'})^{\mathrm{n}} \quad (4)$$

where n is 0.5 and $\mathrm{P_a}$ is 101 kPa (Montoya and DeJong 2015). However, as the cementation level increases, the stiffness becomes independent of the stress state, and the n parameter goes to zero. It has been shown that this effect is not very significant when the cementation level is less than about 4% calcite (Nafisi et al. 2018). Furthermore, if the specimen is idealized as a series of layers, then the bender element measurement actually measures the harmonic mean travel time between the sender and receiver bender elements. This average measurement across the specimen provides limited information about the spatial variability of cementation within the specimen, which can be

significant during shearing when localized shear bands form. In this case, during shear localization, the measured shear wave velocity is the harmonic mean of the specimen's intact and degraded cementation portions (Santamarina et al. 2001).

Local calcite content measurements should be taken throughout a specimen due to the fact that spatial uniformity of the cementation in the specimen significantly affects its mechanical properties. This is accomplished by collecting a small sample (between 2-15 grams) and placing it in a pressure chamber with hydrochloric acid, which reacts with the calcite to produce carbon dioxide. This increases pressure, which can be measured and correlated to calcite content (DeJong et al. 2022). One of the primary factors for producing a uniformly cemented specimen is ensuring the bacteria are distributed evenly throughout the sample. Lee et al. (2021) developed a procedure to achieve high uniformity with multiple flushes of bacteria in a soil column in both directions.

Calcite content and shear wave velocity metrics tend to increase linearly with cementation level (DeJong et al. 2022). Kortbawi (2022) found that to quantify cementation, most studies use qualitative bins of light, moderate, and heavy cementation and define these using calcite content or the change in shear wave velocity, ΔV_s. While definitions of cementation level (light, moderate, heavy) vary across studies, common bins include:

Light Cementation = $C_c < 1.5\ \%, \Delta V_s < 150\ \frac{m}{s}$,

Moderate Cementation = $1.5\ \% < C_c < 5\ \%,\ 150 \frac{m}{s} < \Delta V_s < 300\ \frac{m}{s}$,

Heavy Cementation = $C_c > 5\ \%,\ \Delta V_s > 300\ \frac{m}{s}$.

Effect of MICP on Strength

The strength and dilative tendencies of loose sands significantly improve from cementation due to bridging bonds and densification (Lin et al. 2016; Montoya and DeJong 2015; Riveros and Sadrekarimi 2020; Terzis and Laloui 2017). Research shows MICP treatments enhance both the cohesive intercept and friction angle, following the Mohr-Coulomb failure criteria. The cohesive intercept increases due to particle bonding, while the friction angle increases due to increased particle roughness, angularity, and fines content, although the quantitative contributions of MICP due to these factors are not fully known (Kortbawi 2022). Kortbawi (2022) found that the cohesive intercept ranges from 15 to 25 kPa for lightly to moderately cemented specimens, with the peak friction angle increasing by up to 25% for moderately cemented specimens. Note that the reported friction angle has been typically calculated assuming a cohesion intercept of zero:

$$\emptyset' = 2\left(\arctan\left(\sqrt{\frac{\sigma_1'}{\sigma_3'}}\right) - 45\ deg\right) \tag{5}$$

where σ_1' is the major principle stress and σ_3' is the minor principle stress. This means that as cohesion is added through cementation, it is not accounted for, and the friction angle may be overcalculated. However, at large strains, the cohesion within a specimen is expected to be degraded, and the assumption is again valid. When describing cemented soil or those with cohesion, the best practice is to describe the principle stress ratio rather than the friction angle.

Bridging bonds are the primary contributors to peak strength at lower strains. Initially, under compressive loads, the cemented specimen acts elastically; minor breaking of bonds occurs, but the stress is redistributed to other bonds, and the volumetric tendencies are minimized (Kortbawi 2022; Terzis and Laloui 2019). Following this behavior, the bonds degrade to a point where an increasing amount of stress is carried by interparticle friction, and the specimen exhibits

dilative tendencies. At critical state, bonding has fully degraded, and increased shear strength is mainly due to higher fines content, particle angularity, and roughness (Feng & Montoya 2015; Montoya and DeJong 2015; Riveros & Sadrekarimi 2020). This results in a lower critical state void ratio and a steeper critical state line (Darby 2019; Riveros and Sadrekarimi 2020).

Montoya and DeJong (2015) performed a series of undrained and drained triaxial tests on biocemented specimens. Six specimens were prepared to a loose relative density (D_R) of approximately 35% using air pluviation before MICP treatment and shearing. Specimens were treated to light, medium, and heavy cementation levels and subjected to undrained loading to observe shear strength and volumetric behavior. They found that biocemented soils experienced significant improvements in strength and stiffness, with peak strength increasing substantially, while the critical state remained largely unaffected. Shear wave velocity was measured during shearing to evaluate cementation degradation relative to strain level. The study highlighted that shear wave velocity could be a valuable metric not only in laboratory testing but also for monitoring MICP treatments in the field during cementation and checking integrity after an earthquake event.

While MICP may be useful in a wide range of engineering applications, it has been most prominently studied as a liquefaction mitigation technique. Therefore, understanding the response of treated soils to cyclic loading is a priority. Previous research has used direct simple shear (DSS) testing, triaxial testing, and scaled centrifuge modeling to investigate the efficacy of MICP treatment on the resistance to liquefaction triggering.

Lee et al. (2021) performed thirty-four uncemented and twenty-eight lightly cemented DSS cyclic tests to quantify how cementation increases the resistance to liquefaction triggering. The tests were prepared with Ottawa F-65 sand at a loose state with a relative density of approximately

30%. Light levels of cementation improved resistance to triggering, which manifested as a reduction in generated excess pore water pressure and strains for the same undrained loading. It was observed that the greater shear strength of bio-cemented specimens can be attributed to increased specimen stiffness and dilative tendency. The paper also provides quantitative cyclic stress ratio (CSR) versus the number of cycles to liquefaction (N_L) curves under light levels of cementation for Ottawa F-65 subjected to DSS loading.

Xiao et al. (2018) investigated the liquefaction resistance of bio-cemented calcareous sand through a series of thirty-two cyclic triaxial tests. Tests were prepared using air pluviation to approximately D_R = 47%. Two metrics for cementation level were used - the number of treatments applied and the increase in dry mass due to treatment. Unfortunately, both indices cannot be directly compared with calcite content or shear wave velocity increase, as is common in other studies (Montoya and DeJong 2015; Lee et al. 2021; San Pablo et al. 2024). Xiao et al. (2018) noted that measuring the calcite content using the dissolution approach was impossible due to its inability to distinguish between natural and MICP-induced calcium carbonate. SEM images revealed significant particle coating at lower cementation levels and bridging at higher levels, making the original sand particles indistinguishable from uncemented sand. After testing, a selection of specimens were sieved to check for particle crushing. Cyclic tests with confining pressures between 50 and 200 kPa indicated no particle crushing (Xiao et al. 2018).

Several researchers have investigated the cyclic resistance of biocemented sand using centrifuge modeling (Montoya and DeJong 2015; San Pablo 2020; Darby et al. 2019; Zamani et al. 2021). Among these centrifuge studies, the testing program by Darby et al. (2019) focused primarily on liquefaction triggering, considering both cone penetration test tip resistance (q_c) and shear wave velocity methodologies. Darby et al. (2019) performed a series of four reduced scale

centrifuge models: uncemented to heavily cemented (calcite content of approximately 0, 0.8, 1.4, 2.2%). The models were composed of Ottawa F-65 sand and were prepared to a loose initial state with a D_R of 38%. Each model was subjected to 80g of hypergravity acceleration before undergoing a series of shaking events. Between shakes, a cone penetration test was performed, and the shear wave velocity was recorded in order to monitor soil densification and cementation degradation. For light and heavy cementation, the liquefaction triggering resistance was found to be 0.2 CSR and 0.85 CSR, while the q_c doubled from about 35 to 85 MPa (Darby et al. 2019).

MICP Efficacy in Different Soil Types and Mineralogizes (Silica and Carbonate Soils)

Research has primarily investigated MICP treatment on siliceous soils due to their pervasiveness in nature and past geotechnical work on liquefiable sands. However, a substantial portion of the earth's surface is covered by carbonate-rich siliceous sands, wherein most of the sand is silica and up to 50% is carbonate (Watson 2019). One of the most common siliceous sands used is Ottawa-F65 sand, though Ledge Point carbonate sands have also been used in studies.

Ottawa F-65 is a poorly graded sand with sub-angular edges and less than 1% fines used in a broad range of studies, including DSS, triaxial, and centrifuge tests. These studies investigate soil behavior and cyclic strength with and without MICP biocementation and include the aforementioned laboratory tests (Darby et al. 2019; Lee et al. 2021; San Pablo 2020; Zamani et al. 2021). In addition to these, Ottawa F-65 was used in the Liquefaction Experiments and Analysis Projects (LEAP), a collaborative initiative to produce reliable experimental data that could calibrate and validate constitutive and numerical models. LEAP covers a breadth of experimental and numerical analysis for Ottawa F-65 sand, including soil properties, triaxial testing, and twenty-four centrifuge experiments across nine facilities (Kutter et al. 2017). Collectively, these studies

provide a strong basis for investigating the effect of biocementation on silica sands using Ottawa-F65 sand.

Carbonate sands cover a significant portion of the ocean floor but are less studied than silica sands for engineering applications. Ledge Point sand is a coastal aeolian calcareous soil sourced from Ledge Point, Australia, a small region north of Perth, Australia (Cai and Rutherford 2023; Sharma 2004). It is composed of bioclastic grains with discernible marine organisms (Sharma and Ismail 2006). Similar to Ottawa F-65, Ledge Point sand has less than 5% fines and sub-angular edges. Differences include a higher aspect ratio, surface roughness, and interparticle voids (Cai & Rutherford 2023; Li et al. 2021; Kutter et al. 2017). Due to the soil's carbonate mineral composition and structure, particle breakage begins around 800-1,000 kPa when loaded in isotropic compression (Sharma and Ismail 2006). Cai et al. (2023) observed that significant particle breakage occurs during drained triaxial shearing with confining pressures of 400 kPa, likely due to the anisotropic shear loading.

A comparison of the effectiveness of biocementation on siliceous sand (Ottawa F-65) with varying percentages of carbonate sand (Ledge Point) would help establish the potential for MICP to be used in a broader range of soils. Brandes (2011) performed one such comparison, with no cementation, between silica sand (Nevada Sand) and multiple carbonate-based sands and found increased frictional resistance and cyclic strength in the carbonate sand. This was attributed to differences in geometry, hardness, and interparticle voids of the soil (Brandes 2011). Sharma and Ismail (2006) performed monotonic undrained and cyclic tests on Ledge Point sand and compared the results to siliceous sands. They found that Ledge Point's monotonic and cyclic response had a similar overall behavior but a higher friction angle than siliceous sand.

Scope of Work

MICP research has been conducted at various scales, from the microbiological level to reduced-scale system response, but research conducted with the triaxial device has been limited. Triaxial testing allows for control over the stress and loading conditions of a soil specimen, importantly allowing for tracking of the stress path, while still allowing specimen localization. This arguably provides an intermediate condition between scaled centrifuge models, which allow inquiry into the system response, and DSS laboratory tests, which impose a uniform shear strain across a smaller specimen. Building on prior work, twenty-one monotonic and twenty-nine cyclic laboratory tests were performed to evaluate how the monotonic and cyclic behavior changes as a function of MICP treatment level, loading conditions, and soil composition. The stress-dilatancy behavior and critical state line change as the biocementation level increases and when carbonate sand is present. The liquefaction triggering behavior observed is lower than that found with DSS tests and higher than in centrifuge studies. This is attributed to the differences in length scales and boundary conditions affecting failure localization. This study also evaluated the influence of carbonate-based and pure silica sands by systemically testing mixed silica and calcareous sand throughout the three testing phases of specimen preparation, biocementation (when applicable), and triaxial testing. Shear wave velocity measurements performed throughout shearing provided novel and unique insights into changes in fabric and behavior. Finally, post-test calcite content measurements were used to quantify and verify the effective cementation level of the specimens.

MATERIALS AND METHODS

Soil Materials

This study tested two soils: Ottawa F-65 sand (100S) and a mix of 70% Ottawa F-65 to 30% Ledge Point sand (70S30C) by mass. The abbreviated names 100S and 70S30C use the S

(silica) and C (carbonate) to denote the sand's mineral constituents. The Ledge Point sand was sieved to remove grains larger than the #50 sieve (297 microns), resulting in a grain size distribution that is practically identical to Ottawa F-65. The 70S30C mixture was then created by weighing and mixing 30% C to 70% S by mass. The resulting 70S30C mixture also has a reasonably similar gradation to 100S (Figure 1). The differences in mineralogy, angularity, and roughness can be observed in photos of each sand (Figure 2).

The properties of Ottawa F-65 (100S), 70S30C, and Ledge Point (100C) sand are summarized in Table 1. The grain size distribution and minimum and maximum void ratios were measured per ASTM Standards, except that the sieve analysis and minimum void ratio were modified to allow testing of a smaller sample size. The results were similar to soil properties reported by Kutter et al. (2017) and Sharma (2004), with some deviations from the minimum and maximum void ratios. The measured void ratios are consistent with the laboratory test protocols used and were therefore used in place of literature values.

Specimen Preparation

Specimen preparation was performed as follows. First, a membrane was placed on the triaxial base pedestal and on a 140 mm × 70 mm cylindrical mold. The membrane was stretched tight with an applied vacuum behind the mold. The sand was air pluviated into the model following processes and equipment used in previous centrifuge and laboratory studies to achieve the target density (D_R ~ 35 %) (Kutter et al. 2017; San Pablo et al. 2024; Lee et al. 2021). After installing the specimen top cap and sealing the specimen, a vacuum was gradually applied to approximately -100 kPa, effectively consolidating the specimen. The mold was then removed, initial dimensions were recorded, and the cell was installed over the specimen to surround the specimen in water. Cell water pressure was then increased while the vacuum applied inside the specimen was

decreased, maintaining a constant confinement differential. The specimen was next purged with carbon dioxide to achieve maximum saturation and then flushed with de-ionized, de-aired water (Jefferies and Been 2019). Biocemented specimens then underwent MICP augmentation and cementation treatments. Following this, all specimens, including those that were uncemented, were back pressure saturated until a minimum saturation (B-value) of 0.95 was achieved, docked with the fixed-end loading ram, and consolidated to the final target pressure. An in-depth, step-by-step procedure is provided in Appendix A.

Bio-Cementation Treatment

Cell Culturing

The *S. pasteurii* bacteria was sterilely transferred from a verified culture to an agar plate designed to support *S. Pasteurii* growth. The agar plate was incubated at 28°C for 24 hours before storing at 4°C. A new plate was remade every 2-3 weeks to maintain a fresh culture. Growing *S. pasteurii* on an agar plate allows contamination to be visually identified; if a variation in phenotype was observed, the plate would be discarded and remade (Graddy et al. 2021; San Pablo 2024).

An isolated colony was removed from the agar plate following sterile procedures and placed in a test tube of liquid growth medium comprised of 15.75 g/L tris base, 20 g/L yeast extract, and 10 g/L ammonium sulfate ($(NH_4)_2SO_4$). Each chemical was autoclaved separately at 121°C before mixing (Ribeiro and Gomez, 2023). The inoculated growth medium was incubated in a 28-30°C water bath and orbitally shaken at 200 rpm for 36 hours. The growth test tube was kept at room temperature for the remainder of the week.

Larger volumes of the growth medium, usually 200 mL (to make 4 pellets), were then grown by adding a 1/500 mix of test tube culture to the sterile growth medium. This was incubated

under the same conditions for approximately 36 hours. The fully grown medium was pelleted by spinning down cells and discarding supernatant liquid (Ribeiro and Gomez, 2023). Pellets were made by placing 50 mL bacteria growth medium in a Falcon centrifuge tube and spinning it at 4600 RPM for 30 minutes. After discarding the supernatant, 40 mL of 9 g/L saline solution was added, and the mixture was centrifuged for 15 minutes. The supernatants were again poured off, and 10 mL of saline was added to suspend the bacteria in the final pellet. The optical density was measured with a microplate spectrophotometer using a wavelength of 600nm (OD600). This was then converted to a cell density using a conversion of 1.44×10^9 cells/OD (Graddy et al. 2021; Burdalski et al. 2022) and verified to have a minimum density of 1.77×10^9 cells/mL (Ribeiro and Gomez 2023). Recipes for solution preparation are provided in Table 2. An in-depth, step-by-step procedure is provided in Appendix B.

Treatment Injection

Augmentation injections followed procedures proposed by Lee et al. (2021). First, one pore volume (approximately 230 mL) of inoculum was injected from bottom to top in the specimen, flushing out the initial pore water, which was discarded. A second pore volume was pumped from bottom to top, and the effluent was collected. Third, two pore volumes were pumped from top to bottom, and all the effluent was collected. The three pore volumes of collected effluent were mixed and returned for reinjection. Fourth, one pore volume was injected from bottom to top, and the effluent was mixed back into the injection solution. Finally, one last pore volume was injected from top to bottom. Measurements of initial and final shear wave velocity were recorded along with samples of augmentation solution to verify cell count reduction. This method was believed to improve spatial uniformity and maximize bacteria attachment. As shown in Figure 3, the shear wave velocity increased by approximately 10 m/s pre- to post-augmentation. Since no cementation

solution was present, this increase is likely due to a slight increase in bulk density, as trapped air in the pore space either dissolved into the solution or was pushed out.

For each cementation treatment, two pore volumes of treatment solution were injected from the bottom to the top of the specimen. Shear wave velocity was monitored prior to and immediately after injection. Additionally, after treatment, an hourly automated shear wave velocity measurement was used to monitor the ongoing progress of V_s during treatment, as seen in Figure 3.

When the target shear wave velocity was reached, specimens were flushed with three pore volumes of de-ionized de-aired water. Shear wave velocity was measured before and after the final rinse. During analysis, the total change in shear wave velocity (ΔV_S) due to cementation was recorded as the difference between V_s after the rinse and before the first cementation treatment. Refer to Figure 3 for the V_s measurements taken throughout all biocementation treatments.

Bromide Tracer Test

Bromide tracer tests were performed on two cemented specimens to quantify the advective dispersive transport properties of the specimen. The test was performed by injecting three pore volumes of 15 mM sodium bromide (NaBr) solution, followed by three pore volumes of deionized water. The solutions were pumped using a peristaltic pump calibrated to a 20 mL/min flow rate. Specimens were collected every 50 mL and tested for conductivity to measure the level of passive tracer ions present. The results were normalized by the initial conductivity of the 15 mM NaBr solution, and the volume that passed through the specimen was normalized by the pore volume calculated from the specimen's properties (Ribeiro and Gomez, 2023).

Figure 4 shows the breakthrough curves from the two passive tracer tests. The results are consistent with similar tests by Ribeiro and Gomez (2023) and show that 1.5-2.0 pore volumes (PV) are adequate to saturate the entire specimen with more than 95% concentration throughout the specimen.

Cyclic Triaxial Device

GDS Instruments Inc. manufactured the triaxial system (Figure 5), which includes a 50 kN load frame, 2 MPa pressure controllers for regulating cell and pore pressure conditions, and bender elements embedded in the base pedestal and top cap to measure shear wave velocity. The system is controlled digitally through the GDS Lab software. Data during the test was recorded from a linear variable differential transformer (LVDT) for displacement, an internal submerged load cell for axial force, a pore pressure transducer mounted to the base pedestal for pore pressure, pressure controller measurements for volume, and embedded bender elements for shear wave velocity. No corrections were applied to the load cell measurements as the ram shaft friction was bypassed with the GDS load cell design.

Shear Wave Velocity Measurements

The shear wave velocity was measured using GDS bender elements embedded in the specimen top cap and base pedestal. The bender elements were wired to a GDS data acquisition system operated by the GDS BES program, and the input motion was comprised of a square wave with a 10 kHz frequency. The signal was captured with a resolution of 2 MHz and saved in stacks of 60 triggers when possible. With the current software, stacked measurements were only possible by manually triggering the signal. Automated periodic unstacked single measurements were recorded for periodic measurements where manually triggering was impractical. In post-processing, a 2nd order Butterworth filter was applied when the signal was muddled by signal

noise or signal measurements were not centered around the x-axis, as was the case for single-shot measurements. This is because the Butterworth filter centers the signal along the x-axis. The Butterworth filter was set using a low pass frequency of 4-7 kHz and a high pass frequency of 13-40 kHz to bracket the 10kHz input frequency and reduce higher and lower frequency noise (Montoya et al. 2012). The signal travel time was measured from the start of the square wave to the start of the arriving signal (Basson 2021). A trigger system lag of 13 ms was removed from each measured arrival time to account for the data acquisition system lag time. Measurements were acquired before and after each treatment, during the cementation process, and triaxial loading. Some measurements during the cementation process and triaxial loading could not be stacked due to software limitations, leading to a higher error than stacked measurements. The recorded signals were analyzed using a custom Python code developed by the author, which helped ensure consistency and repeatability in interpretation. Measurements during shearing had the travel distance adjusted by adding or subtracting displacement measurements recorded in the triaxial data.

Interpreting shear wave velocity data is often challenging due to the intrusion of signal noise, unknown frequency content, and analysis choices. The analysis of monotonic compression tests was comparatively straightforward as the stress states during tests gradually increased or decreased. In this case, the confidence of the shear wave velocity is estimated to have an uncertainty of ±5 m/s. In contrast, cyclic tests can be more challenging to analyze. The compression and tension stress cycling causes a variety of anisotropic stress states, which changes the specimen's resonant frequency and amplifies secondary frequency content. Additionally, as the effective stress goes to zero and the specimens liquifies, the shear wave velocity signal can disappear in the measured signal, making it difficult to track from one measurement to the next.

For these reasons, the uncertainty of the shear wave velocity of cyclic tests is higher, especially at lower effective stresses.

Calcite Content

After shearing was complete, bio-cemented specimens were cut into seven equally spaced segments to capture the special variability along their lengths, as seen in Figure 6. Each specimen segment was dried, homogenized, and sampled to measure calcium carbonate content. The calcium carbonate content of a sample was measured by reacting it with hydrochloric acid and measuring the produced carbon dioxide gas (Eq. 6). The reaction was performed in a closed chamber with a pressure transducer to measure the increase in pressure and, consequently, the carbon dioxide. Since the reaction's stoichiometry controls the conversion of calcium carbonate to carbon dioxide, the two properties have a linear relationship.

$$CaCO_3(s) + 2HCl(aq) \leftrightarrow CaCl_2(aq) + H_2O(l) + C0_2(g) \quad (6)$$

The calcite content measured for the 100S biocemented specimens can be entirely attributed to biocementation, as the pure silica sand has no calcium carbonate. However, measuring the calcite content of the 70S30C introduced two complications. First, the sand naturally contains 30% Ledge Point sand, which is almost entirely calcium carbonate, meaning a baseline of uncemented 70S30C must be subtracted from bio-cemented sand to quantify the amount due to biocementation. Second, the weight of the sample tested would have to be reduced to around 2 g to stay within the pressure range of the pressure transducer.

In developing the baseline calcite content for the 70S30C, 12 samples were tested, resulting in an average calcite content of 24.85% and a standard deviation of 0.70%. If the variation in the measurements is assumed to be entirely due to aleatory uncertainty, then 95% of the time (two

standard deviations), the baseline will be 24.85±1.4%. Since the expected contribution of calcite content due to biocementation is expected to be 1%-3%, the resulting calcium carbonate content of 70S30C specimens is quantitatively insignificant. This can be corroborated in the samples that produced negative calcite content estimates after subtracting the above baseline value. Negative values were removed as there is only a physical basis for positive calcite contents.

Specimen Loading

Isotropic consolidation was performed by gradually increasing the cell pressure to 400 kPa per hour until the target effective stress was reached. For example, ramping a sample to 100 kPa effective stress occurred in fifteen minutes. After the ramp was complete, specimens were allowed to consolidate until less than 10 mm^3 of pore fluid changed in five minutes.

The drained and undrained tests were loaded at a constant displacement of 0.25 mm/min and 0.5 mm/min, respectively. This was sufficient to allow drainage for dissipation of excess pore pressures during drained loading.

The cyclic loading stage used a load-controlled feedback system to create a stress-controlled sinusoidal deviatoric stress path with a characteristic input period and deviatoric stress amplitude. Though primarily designed for monotonic tests, this system has software and a load feedback loop to perform cyclic tests, thus making it a quasi-dynamic triaxial. To allow the cell pressure controller to hold constant pressure during the test, the loading rate was reduced to a frequency of 0.0017 Hz, or a period of 10 minutes. Cyclic deviatoric amplitude was set using Eq. 7. All tests were performed by two-way loading with a static offset of zero.

$$CSR_{TX} = \frac{q}{2\sigma_c'} \tag{7}$$

CSR is the cyclic stress ratio, q is the deviatoric stress amplitude, and σ'_c is the effective consolidation stress.

RESULTS

Monotonic Response and Critical State Line

To understand the monotonic response, thirteen isotopically consolidated drained (ICD) tests and eight isotopically consolidated undrained (ICU) tests were performed. Table 4 tabulates the main results of the drained tests, while Table 5 tabulates the main results from the undrained tests. These include details about the specimen's initial conditions, cementation properties, peak strength, and 20% (high) strain strength.

Isotopically Consolidated Drained

Uncemented 100S

As a baseline, six tests were performed at confining pressures from 100 kPa to 900 kPa, with four of the specimens being prepared in a loose state (i.e., relative density below 40%) and two specimens prepared to a medium relative density of 56% and 64%. The results show that all specimens' deviatoric stress (q) increases with axial strain, indicating a strain-hardening behavior (Figure 7a). As the confining pressure was increased from 100 kPa to 900 kPa, the deviatoric stress increased from 230 kPa to 2000 kPa. Additional evidence of suppressed dilation includes a decrease in peak friction angle from 33.0 deg at 100 kPa to 31.7 deg at 1000 kPa, as seen in Table 4 and Figure 7b, and decreases in volumetric strains (Figure 7c).

The denser specimens exhibited increased peak shear strength due to increasing dilative behavior, as evident in the volumetric strain (Figure 7c). Increased density also caused stronger strain localization along the failure plane(s). This is most evident in the densest specimen, which

had a drop in deviatoric stress and a decrease in the rate of negative pore pressure generation at approximately 9% (Figures 7a and 7c).

Shear wave velocity (V_s) was measured throughout the shearing process for the four loose tests at confining pressures of 100, 300, 500, and 900 kPa (Figure 7d). The V_s values show a general trend of increased axial strain due to the corresponding increase in mean effective stress. The initial V_s values exhibited a broad range, indicating the dependence of V_s on initial confining stress, consistent with the empirical relationships. To remove the effect of the confining stress, the shear modulus, $G_{max,}$ was normalized by the square root of the mean effective stress (p′) (Figure 7e). The normalization effectively removed the stress-dependent component, resulting in a constant trend showing the minimal change in fabric. This will be used as the baseline when comparing cemented specimens to understand cementation degradation (Figure 7d).

Uncemented 70S30C

Three loose uncemented drained tests were performed on the 70S30C at 100, 300, and 500 kPa confining pressures to establish an uncemented baseline and compare the response against the 100S. The 70S30C consistently shows higher deviatoric stress values at both peak and critical state compared to the 100S for all confining pressures. Figures 8a and 8b indicate that 70S30C has a greater resistance to deformation under shear stress. The volumetric strain of the 70S30C soil compressed less than the 100S and began dilating at lower axial strains. For example, the 70S30C began to dilate at 3% strain compared to the 100S, which started dilating at 4.5% strain. The earlier dilation in 70S30C can be attributed to the more angular shape of the carbonate sand, which promotes dilative behavior under shear stress (Sharma and Ismail 2006). V_s trends, as shown in Figure 8d, are similar overall, with the exception that 70S30C sand appears to be decreasing more with axial strain. Normalized G_{max} in Figure 8e was constant with axial strain, implying that the

force chains within the particle matrix, though evolving, produced consistent stiffness throughout shearing. This is expected since no cementation degradation was present. This is consistent across all 100S and 70S30C uncemented specimens.

Biocemented 100S and 70S30C

Loosely prepared specimens underwent biocementation at two different levels (lightly cemented, $\Delta V_s \approx 150$ m/s and moderately cemented, $\Delta V_s = \sim 300$ m/s) using both 100S and 70S30C. Both sands show an increase in peak deviatoric stress with higher cementation levels (Figure 9a). Additionally, Figure 9b shows that the normalized deviatoric stress increases with cementation level, indicating enhanced shear strength and stiffness with MICP treatment. The observed behavior can be categorized into three trends: initial small strain response (first 2% strain), strain hardening (2% - 7.5% strain), and steady-state (after 7.5% strain).

At the initial small strain response (~2% axial strain), the deviatoric stress shows nearly vertical increase, indicating the high initial stiffness attributed to the biocementation bonding at particle-particle contacts. As the bonds break, the stress is redistributed to other bonds, which results in a cascading rapid degradation in bonding. This is reflected in the normalized G_{max} trend, which drops quickly to levels similar to those of the uncemented specimen (Figure 9e). For example, for 100S lightly cemented and 100S moderately cemented specimens, the normalized G_{max} values were initially 2200 and 5500, respectively, but decreased to 1200 after 2% strain, comparable to that of the uncemented 100S. It is noted, however, that actual degradation is even faster within shear bands as the G_{max} trend is based on the measured harmonic mean V_s value across the entire specimen height.

The behavior of all loose biocemented specimens shifted from a stiff elastic to a strain hardening behavior as the cementation degraded. The strain hardening trends were similar to the

loose uncemented specimens, but the cemented specimens had higher deviatoric stress (Figure 9a). This indicates that even though the biocementation degraded, it still contributed to soil structure compared to the uncemented specimens. The volumetric strain analysis revealed that the soil became more dilative with increasing cementation, as shown in Figure 9c. The dilation began at lower strains and produced greater volumetric dilation than its uncemented counterpart. For example, the 100S specimens began to dilate at ~5% strain when uncemented, 4% strain for lightly cemented, and within the first percent for moderately cemented.

At strains above 7.5%, where the specimen is approaching critical state conditions, a clear shear band(s) where cementation is fully degraded is established (Figures 10 and 11). The strength continues to degrade towards the uncemented strength, indicating that the benefits of MICP treatment are limited at the cementation levels tested herein.

Throughout the drained tests, the 70S30C had higher strength at all cementation levels than their 100S counterparts. For example, the loose moderately cemented specimen of 70S30C reached a peak deviatoric stress of 306 kPa, while its 100S counterpart reached 275 kPa. This indicates that the initial mineralogy and increase in friction observed in the uncemented comparison led to a continued benefit when cemented.

For further context, the behavior of the biocemented specimens can be compared against the dense uncemented specimens (Figure 12). In this case, uncemented dense specimens were found to have higher peak strength and volumetric dilation compared to light and moderately cemented loose specimens.

Isotopically Consolidated Undrained

Uncemented 100S

A baseline set of three loose (D_R=35%) 100S specimens were tested under undrained conditions at confinement of 100, 300, and 1000 kPa, and one medium-dense (D_R=56%) 100S specimen was tested under undrained conditions at a confinement of 100 kPa. As expected, the results in Figure 13 show that with increased confining pressure, the normalized deviatoric stress decreases (Figure 13a) and the normalized excess pore pressure increases (Figure 13b). Both of these are normalized by p_c', the mean effective stress at consolidation. Furthermore, when comparing the influence of specimen density on the behavior, it was observed that the dense specimen exhibited a much stronger dilative response, resulting in larger negative excess pore pressure (Figure 13b). This is consistent with Montoya and DeJong (2015). Note that the dense specimens were stopped at 7.5% strain to prevent the pore pressure from dropping to a point that could cause cavitation within the specimen.

As seen in the drained tests, the shear wave velocity measured throughout each test increases with the stress state. However, unlike the drained tests, the V_s increases more because the soil's dilative tendencies produce a larger increase in the effective stress. When normalized by the mean effective stress, all four specimens exhibit a constant normalized G_{max}, consistent with all of the uncemented drained tests.

70S30C

Two loosely prepared undrained tests were performed on the 70S30C to compare the uncemented behavior (Figure 14). The responses were initially similar, with slightly more dilation in the 70S30C soil. One noticeable difference was that the dilative pore pressure response plateaued at larger strains, whereas the 100S kept dilating. An example of this, Figure 14b, are the specimens

confined to 100kPa where pore pressure trends are almost identical up until 12% strain, at which time the dilation rates changed; by 20% strain, the 100S specimen had reached -400kPa while the 70S30C specimen had only reached -170 kPa. This could be due to a steady state condition being met or possibly particle crushing at the higher shear stress, causing contraction due to particle crushing, which counteracts the dilative behavior.

Biocemented 100S

Undrained tests were performed on the 100S at cementation levels of ΔVs = 150 and 300 m/s, in addition to the uncemented case (ΔVs = 0), under a confinement of 100 kPa (Figure 13). All tests generated positive pore pressure initially (contractive tendency), followed by negative pore pressures (dilative tendency). The specimens with higher cementation levels exhibited less positive pore pressure generation and transitioned to negative pore pressures at lower strain levels. The excess pore pressures became negative at strains of 12%, 1.5%, and 0.5% for the ΔVs = 0, 150, and 300 m/s specimens, respectively.

The shear wave velocity and normalized G_{max} showed a rapid degradation within the first 1% of axial strain for cemented specimens, followed by a more gradual convergence as the strain reached 5%. This behavior is consistent with the uncemented specimens at larger strains and with the drained response discussed in the previous section.

It is noted that the initial deviation in the stress-strain data of the 300m/s specimen is due to a tilted top cap and docking with the fixed-end loading ram (Figure 15). This is not believed to affect the overall test response.

Critical State

Critical state is, classically, a state in which soil continues to deform yet has no propensity to change its void ratio (Jefferies and Been 2019). This condition is synonymous with constant volumetric strain and constant pore pressure in drained and undrained tests, respectively. The soil must be loose enough to deform globally (in order to avoid localization effects in triaxial specimens where global measurements of strain are not representative of conditions inside the shear band) to a sufficient strain level such that a steady state condition is reached. The monotonically tested specimens herein did not reach complete critical state conditions of constant volumetric strain or excess pore pressure at 20% axial strain. The soil was either not loose enough and/or not strained to a high enough level to reach critical state. Volumetric strain and pore pressure generation rates were observed to decrease towards the end of loose tests. The strain conditions at the end of each test (20% strain) were noted to be at or just below the critical state, and a line was manually fit accordingly (Figure 16). The results were fitted to the logarithmic function:

$$e_{cs} = a - b\left(\frac{p'}{p_{atm}}\right)^{c} \tag{8}$$

as recommended by Jefferies and Been (2019), where e_{cs} is the void ratio at critical state, p' is the mean effective stress at critical state, p_{atm} is the atmospheric pressure, and *a, b,* and *c* are the fitting coefficients. The resulting coefficients were a = 0.909 and 0.767, b = -0.035 and -0.011, and c = 0.42 and 0.50 for 70S30C and 100S, respectively. This also follows the trends by Vasko (2013) (Eq. 9) and El Ghoraiby (2020) (Eq. 10) as shown in Figure 17.

$$e_{cs} = 0.78 - 0.0112\left(\frac{p'}{p_{atm}}\right)^{0.715} \tag{9}$$

$$e_{cs} = 0.74 - 0.035\left(\frac{p'[MPa]}{p_{atm}[kPa]}\right)^{1.218} \quad (10)$$

The minimum and maximum void ratios differ for each soil type, resulting in a shifted vertical axis. The curvature of the 70S30C was observed to have a steeper slope, which was hypothesized to be due to particle crushing. The critical state lines (CSLs) for 100S and 70S30C approach each other around 3 MPa, which is outside the testing range of this study.

The critical state behavior was compared to the literature values of El Ghoraiby (2020) and Vasko (2013) in Figure 17. The critical state line for 100S remained below that of Vasko (2013) until about 800 kPa and remained above El Ghoraiby's (2020) for the range of effective stress. The trend also has less curvature than both the Vasko and El Ghoraiby fitted trend lines. The 70S30C created for this study is unique and has no literature to compare to. However, considering the 70S30C's increased minimum and maximum void ratio, the critical state line is within the expected range.

Biocemented 100S and 70S30C

The void ratios at the end of the drained tests were used to indicate the direction of shift of the CSL for the bio-cemented drained and undrained tests, as there was insufficient data to develop a complete CSL. Additionally, because the cemented specimens exhibited localized shearing, a true critical state condition was not reached. Nonetheless, it can still be observed that the end condition and CSL in both cases shift down with increasing cementation levels (Figure 16). It is inconclusive if the curvature of the critical state line changes with increasing cementation.

Undrained Cyclic Response

Cyclic load-controlled triaxial tests were performed on 100S and 70S30C soil types to understand the improvement effects due to biocementation, soil type, and density. Each specimen was isotopically consolidated to an effective stress of 100 kPa before being subject to undrained load-controlled cycles. The performance of each specimen was examined by comparing the loading intensity with the number of cycles to reach excess pore water and axial strain thresholds. A summary table of the results is shown in Table 6. Herein, liquefaction is defined in two ways: an increase in pore pressure to a $r_u > 0.95$, where r_u is the ratio of excess pore pressure to initial effective stress, and 3% axial strain. The following notation will be used to indicate the number of cycles to liquefaction of both criteria: $N_{cycles\ to\ ru>0.95} | N_{cycles\ to\ 3\%\ strain}$. Post-liquefaction cycles will be described as the number of cycles between 3% and 9% strain.

100S

The 100S was prepared in both loose and dense conditions and biocemented to ΔVs of 0 (uncemented), 150 (lightly cemented), or 300 m/s (moderately cemented). Figures 18 and 19 show the behavior of the loose ($D_r \approx 30\%$) and dense ($D_r \approx 58\%$) tests, respectively, from which several trends can be observed.

Uncemented behavior

The uncemented specimens exhibited behavior typical of uniform sub-angular uncemented silica sands, which include rapid pore pressure generation, strength loss, and liquefaction triggering in relatively few cycles, followed by significant strain accumulation. Figure 18 shows the loose specimens, and Figure 19 shows the dense specimens. The CSR magnitude range required to trigger liquefaction was relatively low (0.09 to 0.15), and strong sensitivity between the CSR level and the number of cycles to liquefaction was observed.

As seen in Figure 18 a-c, loose uncemented specimens exhibited a rapid increase in pore pressure generation and strain during tensile loading, typically corresponding to when the pore pressure had risen between $r_u = 0.3$ and 0.7. The spike in pore pressure generation caused the stress state to collapse on the critical state line and dilate for the remainder of the tensile loading, as most clearly evident in Figures 18 and 19 (column 3-4). The following positive loading follows the failure envelope, resulting in liquefaction. This phenomenon is attributed to soil structure instability, similar to flow liquefaction (Ye et al. 2018; Yang and Pan 2017). In these loose uncemented tests, the number of additional cycles to reach -10% strain was minimal (1 to 2 cycles). Dense uncemented specimens exhibited increased cyclic resistance leading up to liquefaction as well as more cycles after liquefaction and before reaching 10% strain (Figure 19 a-c). For example, in comparing 0.10 CSR loose (Figure 18b) and 0.10 CSR dense (Figure 19c) specimens, the loose specimen reached liquefaction at 7.8 *cycles to ru>0.95*|7.8 *cycles to 3% strain* while the dense specimen reached liquefaction in 53 *cycles to ru>0.95*|53.6 *cycles to 3%* strain. This means there was approximately one order of magnitude increase in the number of cycles. Additionally, post-liquefaction, the loose specimen reached 9% strain in 1.1 additional cycles, while the dense specimen reached it in 4.1 additional cycles (Table 6).

Biocemented behavior

The effect of cementation on the cyclic behavior is pronounced, as evident in the CSR ranging from 0.2 to 0.4, to trigger liquefaction in a similar number of cycles as the uncemented specimens (Figure 20 and Figure 21). This also means uncemented and lightly cemented specimens do not have overlapping CSR trend lines. Before triggering, the lightly cemented specimen (ΔVs = 150 m/s) behavior showed increased stiffness and dilative strength, similar to their monotonic counterparts, which suppressed pore pressure generation. This resulted in more cycles or higher

stress needed to reach liquefaction, confirming that the cyclic resistance increases with the cementation level. Specimens with light cementation mainly exhibited a global shear failure mode similar to uncemented specimens; however, only specimens at loading of 0.35 CSR and above exhibited instability, as seen in Figures 20a and 21a-b. Tracking of shear wave velocity during cycles after liquefaction triggering produced unique trends, as shown in Figure 17c. The V_s consistently varies during an individual cycle, as the degraded cementation makes the V_s primarily dependent on confining stress. As the plot shows, the shear modulus decreases rapidly, approaching a value of 0 MPa, as the stress path approaches zero effective stress.

Loose (D_R = 26%) and dense (D_R = 52%) specimens were both tested at a CSR of 0.35 and liquefied within the first cycle due to instability failure (Figures 20a and 21b). However, the test with higher density in Figure 21b needed 2.2 cycles to reach 9% strain compared to the loose test, which needed only 1 cycle to reach 9% strain. This increase in post-liquefaction resistance is attributed to the denser soil's stronger dilative tendency. The dense (D_R = 58%) specimen tested at 0.30 CSR demonstrated greater pre-liquefaction (43 $_{cycles\ to\ ru>0.95}$|45.6 $_{cycles\ to\ 3\%\ \text{strain}}$) and post-liquefaction cyclic resistance (7 cycles) than the loose (D_R = 30%) specimen tested at 0.25 CSR which liquified in 6 $_{cycles\ to\ ru>0.95}$|6.6 $_{cycles\ to\ 3\%\ strain}$ and had 3 post-liquefaction cycles.

The benefit of biocementation was even more pronounced in the moderately cemented specimens treated to a ΔV_s = 300 m/s (Figure 18). These specimens did not exhibit instability but instead stronger dilative behavior as they approached liquefaction triggering (Figures 22 and 23). Due to the higher levels of cementation, these tests also exhibited more localization of the failure, which, in some cases, could be correlated to the least cemented portion of the specimen (determined post-test by calcite measurements along the specimen length). One of the most extreme cases of localized failure was observed in the loose 300 m/s specimen tested at 0.6 CSR

(Figures 22 and 23). Liquefaction occurred in $1_{cycle\ to\ ru>0.95}|1.6_{cycles\ to\ 3\%\ strain}$, followed by 3.1 cycles post-liquefaction. The initial failure was observed to be a shear band in the lower part of the specimen in the first cycle, the location was later identified as having the least calcite content. The unique progressive failure observed in the final 3-5 cycles is shown in Figure 23 and is described in detail as follows. During the compressive loading of cycle 3, a slight bulging occurred at the bottom of the specimen (1a). During the following tensile loading, shear zones expanded, and the bulge showed a reduction in its cross-section (i.e., necking) (1b). With each of the following cycles, the failure area progressively moved upward, forming small shear fractures (shear zones) under compression and pulling those zones apart under tension (2a-2b). The final failure zone was localized at the center of the specimen when it reached the maximum shear strain of -10%. This progressive failure pattern is consistent with the calcite content distribution within the specimen. The minimum calcite content of 0.9% was located at the bottom of the specimen, while the average calcite content for the entire specimen was 2.2%. It is worth noting that the progressive failure also occurred in the first 2 cycles that were not described, but due to the small strain, they were not as visible.

As expected, dense, moderately cemented specimens exhibited higher pre- and post-cyclic resistance (Figure 24). As they approached liquefaction, they exhibited dilative behavior rather than instability during failure.

Based on the above observations, it is hypothesized that cementation bonding contributed to pre-triggering resistance, whereas the density, particle roughness, and particle angularity have a more negligible impact. Post-liquefaction, the effect of cemented bonds appears to be minimal, as they have broken down, and the increased density, angularity, and roughness of the degraded cementation became more significant.

70S30C

Untreated sand

Uncemented loose 70S30C specimens exhibited a slight increase in cyclic resistance compared to the loose 100S counterparts and were similar to the 100S dense specimens (Figure 25). The increased resistance to liquefaction triggering and subsequent strain accumulation in the 70S30C specimen is attributed to the greater angularity of the carbonate fraction of the sand mixture. For example, the 0.12 CSR loose 70S30C specimen (Figure 25b) triggered in 17.8 *cycles to ru>0.95*|17.8 *cycles to 3% strain*, while the 100S (Figure 18a) counterpart liquified in 1.7 *cycles to ru>0.95*|1.8 *cycles to 3% strain*. The loose 70S30C was still lower than the dense 100S specimen that liquified in 25 *cycles to ru>0.95*|27.6 *cycles to 3% strain*.

Biocemented behavior

Two lightly cemented 70S30C specimens, treated to a ΔV_s = 150 m/s, produced systematically consistent results (Figure 27). The biocementation increased the resistance to liquefaction triggering, and some benefits remained post-triggering. When comparing loose lightly cemented specimens with 100S (Figure 20c) to 70S30C (Figure 27b), the 70S30C liquified in 48 *cycles to ru>0.95*|48.7 *cycles to 3%strain* with 1 post-liquefaction cycle to reach an axial strain of 9% while the 100S liquified in 35 *cycles to ru>0.95*|35.7 *cycles to 3% strain* with 3.1 post-liquefaction cycles.

Three tests with 70S30C were moderately cemented to ΔVs = 300 m/s (Figure 28). However, while the target *Vs* was achieved according to the bender element measurements, the shearing behavior and calcite content indicated that the specimens were less cemented than the corresponding 100S specimens. The specimen behavior of this set of tests was inconsistent with all other tests. The source of the difference could not be conclusively identified due to the high baseline carbonate content of 70S30C. Despite this, the following factual differences in behavior

were identified. Specimens at 0.55 (Figure 28a) and 0.35 (Figure 28c) CSR exhibited similar behavior of flow liquefaction after three-quarters of a cycle. The specimen tested at 0.45 CSR (Figure 28b) had an instability failure after 1.75 cycles but had shear wave velocity and calcite content between the tests with CSR values of 0.35 and 0.55. Additional analysis is needed to understand if the inconsistency between shear wave velocity and calcite content is a bender analysis error, calcite content baseline error, or a spatial variability issue. However, calcite measurements along the specimen length indicated a relatively uniform condition.

The cementation degradation, indicated by the V_s measurement, was very minor initially during the pre-triggering cycles until excess pore pressure began to increase. When excess pore pressures began to accumulate, the biocementation degraded, enabling strain levels to increase. Once liquefaction occurred, the cementation became fully degraded, and the normalized shear modulus degraded to a condition similar to the uncemented state. This trend is consistent across both soil types.

DISCUSSION

The testing program performed, with unique test measurements and specimen conditions, provides the opportunity to develop additional insights regarding the soil state during cyclic loading and the influence of biocementation level and soil mineralogical composition.

G_{max} Variation within Loading Cycles

As discussed above, the shear modulus varies significantly across the full range and within individual cycles. In early cycles, the shear modulus remains largely unchanged, but then decreases as cementation degradation occurs in the cycles prior to liquefaction trigging. The shear modulus during post-triggering cycles continues to decrease until the cementation is degraded, after which

the behavior stabilizes. This is shown in Figure 29, which is separated into columns of uncemented, lightly cemented, and moderately cemented. This plot highlights variability but clearly shows the baseline normalized G_{max} in uncemented tests residing around 1,000 (defined as a dimensionless parameter of $G_{max}/(p'p_a)^{0.5}$) and cemented tests initially starting around 2,000 for light cementation and 4,000 for moderate cementation degrade to around 1,000 during liquefaction.

The variation of shear modulus within individual cycles is more interesting, as the value changes with cementation degradation and the effective shear stress. Building on the discussion in the previous section, Figure 30 shows the relationship between deviatoric stress on the Y axis and mean effective stress on the X axis with points colored by the normalized small strain stiffness for the three dense lightly cemented 70S30C specimens. The relationship of deviatoric stress to mean effective stress shows a decrease in the shear strength of the soil with increasing pore pressure, as it relates to compression and tension with each cycle. The test shows that the mean effective stress decreases with each cycle as the pore pressure increases. The normalized G_{max} in this uncemented specimen is expected to be similar to a monotonic test where the soil fabric and normalized G_{max} remain unchanged. In reality, particle rearrangement occurs more in a cyclic test than in a monotonic test because when the mean effective stress goes to zero, it is easier for particle rearrangement to occur. It is observed that during the butterfly curve in post-liquefaction, the normalized G_{max} is greater during the compressive cycle and weaker during the tensile cycle. This difference in shear wave velocity is related to the stress anisotropy during that cycle. Since the shear wave velocity is controlled by the stress in the direction of and perpendicular to the wave propagation but in line with the wave polarization, the stress in the out-of-wave direction perpendicular to propagation, is not a controlling variable. Therefore, the shear modulus should only be normalized by stresses contributing to wave speed. The hypothesized model normalizes

the stress in the direction of the shear wave propagation (vertical) multiplied by the stress perpendicular to the direction of the shear wave (horizontal).

Calcite Content and Shear Wave Velocity

The numerous specimens treated with biocementation and monitored with shear wave velocity measurements during treatment enable the correlation between the measured calcite and the final pre-shearing shear wave velocity to be examined. Figure 31 shows the average calcite content by location along specimen length for light and moderate cementation. For both levels of cementation, the middle of the specimens was found to be the lowest, and the top was found to be the highest. Figure 32 shows the correlation between calcite content and change in shear wave velocity. The trend roughly follows 1% calcite for every 100 m/s of *Vs*. Error bars indicating the minimum and maximum calcite content for each specimen are also shown.

CSR versus Number of Cycles Curves (Liquefaction Triggering Curves)

The relationship between the CSR and the number of cycles required to achieve liquefaction triggering can be considered for all loading conditions examined in this study (Table 6). Liquefaction triggering curves were fit with the power law equation:

$$\mathrm{CSR} = \mathrm{a}\mathrm{N}_{\mathrm{L}}^{-\mathrm{b}} \tag{11}$$

where N_L is the number of cycles to the liquefaction criterion, and *a* and *b* are fitted constants. As previously defined, the N_L value is the number of cycles when $r_u > 0.95$ or 3% axial strain is reached. The plots here are presented first on a $r_u > 0.95$ basis (Figure 33) and subsequently presented for a 3% axial strain (Figure 34). In most cases with 100S, r_u of 0.95 was reached immediately prior to 3% strain; however, in most cases for the 70S30C, 3% strain was reached immediately prior to r_u of 0.95 (Table 6 – Cycles between 3% and $r_u = 0.95$). The *a* and *b* values

determined for each suite of tests are tabulated in Figure 36. It is important to note that fitting the trends required subjective judgment due to both typical experimental variability and variations of calcite cementation within an individual specimen. Table 5 presents the calcite content variation across each specimen. The initiation was expected to occur in the area with the least calcite content, as shown in Figure 23. However, the final failure often occurred in an alternative location. This is likely due to failure propagation during post-liquefaction.

The following overall trends can be observed from these tests. An increase in cementation produced a significant increase in cyclic resistance. For example, the trend for ΔV_s = 150 m/s has a CSR = 0.52 for an N_L = 15 while the CSR = 0.20 for the untreated (ΔV_s = 0 m/s) trend. Additionally, an increase in relative density from loose to medium resulted in a measurable but less notable increase in cyclic resistance. The cyclic resistance of the uncemented and lightly cemented 70S30C specimen was observed to be similar, if not slightly higher, than that of the 100S specimen. Further research could analyze whether the effect of cementation on carbonate soils decreases at a higher CSR due to particle crushing.

CSR versus N Trends Compared to Literature

To validate the trends developed in this experimental program, results were compared with those of previous studies in the literature. Prior testing has been performed using DSS tests. In order to make a direct comparison, the CSR versus N value trends presented were converted using the following equation:

$$CSR_{DSS} = \left(\frac{1+2(K_0)_{DSS}}{3}\right) CSR_{TX} \quad (12)$$

as presented by Idriss and Boulanger (2008). The critical state friction angle for uncemented 100S sand for DSS tests by Lee et al. (2021) was reported to be near 29.1 degrees. Using the stress

conditions at the end of consolidation and assuming K_0 can be reasonably estimated as $1 - \sin(\phi_{cs}')$ resulted in a constant multiplier of 1.48, which was applied using the rearranged and simplified form of Eq. 12, seen in Eq. 13:

$$CSR_{TX} = 1.48 CSR_{DSS} \quad (13)$$

The fitting coefficients for the 100S uncemented specimens are compared to the equivalent triaxial (TX) trends from Lee et al. (2021) and the TX trends of Kutter et al. (2020) in Figure 37. As evident, the liquefaction triggering curves from 100S uncemented specimens are in reasonable agreement with published values when considering soil type, preparation technique, and testing apparatus. Both loose and dense uncemented 100S specimens have a lower *a* value than those found in Kutter et al. (2017). This is likely attributed to Kutter et al. (2017) specimens' higher relative density (D_R=82%), thus making them less susceptible to liquefaction. The loose uncemented specimens had marginally flatter liquefaction triggering curves than those established in Lee et al. (2021).

Similarly, the uncemented 70S30C specimens have a slightly flatter slope (*a* = 0.18*)* than the triaxial tests of unsieved Ledge Point sands (*a* = 0.18), as shown in Figure 36. (Sharma and Ismael 2006). This may be attributed to the broader gradation, as Sharma and Ismael (2006) used unsieved Ledge Point that had a higher proportion of carbonate (100% compared to 30% in the 70S30C).

When examining the lightly cemented trends, the resulting cyclic resistance curves for the loose 100S and 70S30C are both below the literature values of the loose DSS specimens prepared at 100 m/s by Lee et al. (2021). However, the dense 100S specimen prepared at 150 m/s was above the literature value presented by Lee et al. (2021). Notably, the 100S and 70S30C specimens were

prepared to 150 m/s for this experiment, whereas specimens by Lee et al. (2021) were prepared to 100 m/s. Had they been prepared to the same cementation level, it is expected that the TX tests would have a lower cyclic resistance curve than the DSS test since it is more susceptible to localization within the specimen compared to DSS, as discussed further below.

Effect of Specimen Size on Cyclic Resistance Curve

Specimens of varying sizes play an important role in research progress. Those of smaller scales (DSS tests) only test single variables and establish fundamental behavior, while those of larger scales (centrifuge experiments) examine a system response with numerous variables expected to be found in field conditions.

DSS specimens allow for consistent specimen density and fabric with minimal variation, enabling more uniform MICP treatment. During shearing, boundary conditions enforced by shear rings apply even shear strain across the specimen, thereby forcing a more uniform failure across the specimen and preventing/limiting the formation of shear bands. This causes a higher soil resistance; and subsequently, a specimen forms a preferential shear location.

In field conditions, shearing is expected to follow the path of least resistance across a site and is thus captured better in a reduced-scale centrifuge test. The specimen size of a centrifuge test is larger and, despite layers of pluviation, has the most spatial variability in density. Additional variability is introduced in cementation due to the treatment of larger volumes and boundary conditions. Finally, loading conditions are quite challenging, with complex cyclic loading at the bottom container propagating up through the model. This is only compounded by flexible shear beam container boundary conditions designed to allow the specimen to deform in its preferred manner. Collectively, this results in failure propagation from the bottom up and the potential of initial failure occurring in weaker zones first.

Triaxial testing can be considered transitional from DSS to centrifuge in terms of uniformity and failure localization. Specimens are intermediate in size, so some density and treatment variability can occur, as shown in this study. Further, the boundary conditions provide control of the p-q stress path while allowing specimens to fail locally. This freedom to localize allows failure along the weakest zone, whereas DSS testing forces more uniform shearing throughout the specimen.

CONCLUSIONS

A series of twenty-one monotonic and twenty-nine cyclic triaxial tests were performed to investigate the improvement of monotonic and cyclic strength due to biocementation, soil type, and density. Specimens were prepared using 100S and 70S30C soil to examine the influence of carbonate grains within a siliceous soil matrix. Each specimen was prepared to one of three biocementation levels (uncemented, lightly cemented, moderately cemented) to understand the effect of MICP treatment on the improvement of stiffness and liquefaction resistance (small-strain) and dilative strain hardening and critical state (large-strain). Density was also varied to compare the influence of density to improvement to light and moderate cementation. After analysis of the results, the following conclusions can be made:

1. Uncemented 100S and 70S30C specimens with higher confinement under ICD loading produced larger volumetric strains, higher deviatoric response, and suppression of peak friction angle (Figure 7). The effects of higher density increased the peak shear strength by increasing the dilative behavior, as evident in the volumetric strain (Figure 7b). Increased density also caused stronger strain localization along the failure plane(s). These observations are in agreement with uncemented monotonic behavior.

2. Critical state lines were developed for both the 100S and 70S30C soils. This showed that the 70S30C soil had a higher CSL and curvature than the 100S soil.
3. Light and moderate cementation on loose specimens showed increased peak deviatoric stress and soil stiffness compared to its uncemented counterpart (Figures 9 and 15). Shear wave velocity measurements were used to calculate the G_{max} and normalized G_{max}. This showed that cementation bonds degraded rapidly (within the first 1% of shearing) and were fully degraded to that similar to an uncemented sand by 5% strain (Figured 9 and 15).
4. Light and moderately cemented specimens were found to have a similar if not lower volumetric dilation and peak deviatoric strength, ranging from 255 to 275 kPa compared to dense uncemented specimens with peak drained strengths of 280 to 334 kPa (Figure 12 and Table 4). At larger strains (i.e., 20%), mean effective stress was in a similar range between 177 and 181 kPa.
5. The addition of carbonate resulted in similar overall behavior between the 100S and 70S30C specimens, with the latter presenting a higher peak (deviatoric stress of 268 versus 239 kPa) and critical state friction angle (35.1 versus 33 deg) (Figure 8 and Table 4). The volumetric strain of the 70S30C soil also compressed less than that of the 100S and dilated earlier (Figure 8c). These observations are attributed to the increased particle roughness, decreased hardness, and elongation of the carbonate soil.
6. The uncemented specimens exhibited behavior typical of loose uncemented sands, which include rapid pore pressure generation, strength loss, and liquefaction triggering in relatively few cycles, followed by significant strain accumulation. CSR curves for 100S and 70S30C show a minor increase in cyclic resistance from a = 0.14 to 0.18 for 100S and 70S30C, respectively). Dense uncemented specimens exhibited increased cyclic resistance

leading up to liquefaction, as well as more cycles after liquefaction and before reaching 10% strain (Figure 19 a-c). This means there was approximately one order of magnitude increase in the number of cycles.

7. Overall, the cyclic stress ratio necessary to trigger liquefaction doubled with every 150 m/s increase in shear wave velocity. This was observed by analyzing average *a* values at each cementation level: 0.16, 0.36, and 0.64 for uncemented, light, and moderate cementation. The observed improvement of MICP cementation for cyclic resistance is more significant than the improvement during monotonic response, supporting the use of MICP as a ground improvement method for liquefaction mitigation. Specimen relative density increases dilative tendency and plays a noticeable role at the two levels of cementation tested. However, while the influence on monotonic behavior was found to be similar to or less than that of dense specimens, the cementation on cyclic behavior was found to have a larger impact than density.
8. The DSS equivalent CSR versus N trends for the data generated herein are consistent with the limited data sets in literature and provide evidence that location within the triaxial specimens results in reduced cyclic resistance compared to simple shear conditions for the uncemented specimens.

DATA AVAILABILITY

Some or all of the data, models, or code generated or used during the study are available from the corresponding author upon request.

REFERENCES

Baek, S.-H., T.-H. Kwon, and J. T. DeJong. 2022. "Impact of microbially induced calcite precipitation (MICP) on hydraulic conductivity of coarse sands." *20th International Conference on Soil Mechanics and Geotechnical Engineering*. Sydney, Australia.

Basson, M. S., J. Miller, and A. Martinez. 2021. "Experimental Estimation of Fabric in Granular Materials Using Shear Wave Velocity Measurements." *Soil Dynamics*, Lecture Notes in Civil Engineering, T. G. Sitharam, S. V. Dinesh, and R. Jakka, eds., 311–323. Singapore: Springer Singapore.

Brandes, H. G. 2011. "Simple Shear Behavior of Calcareous and Quartz Sands." *Geotech Geol Eng*, 29 (1): 113–126. https://doi.org/10.1007/s10706-010-9357-x.

Burdalski, R. J. 2020. "Investigating the effect of biological and chemical factors on the reaction kinetics and mineralogy of ureolytic bio-cementation." Master of Science in Civil & Environmental Engineering. Seattle, Washington: University of Washington.

Burdalski, R. J., and M. G. Gomez. 2020. "Investigating the effect of microbial activity and chemical concentrations on the mineralogy and morphology of ureolytic bio-cementation." *Geo-Congress 2020*, Proceedings, 83–95. Minneapolis, Minnesota: American Society of Civil Engineers.

Cai, W., and C. J. Rutherford. 2023. "Monotonic Behavior of Ledge Point Calcareous Sands with Increasing Particle Crushing." *Geo-Congress 2023*, 488–493. Los Angeles, California: American Society of Civil Engineers.

Darby, K. M., G. L. Hernandez, J. T. DeJong, R. W. Boulanger, M. G. Gomez, and D. W. Wilson. 2019. "Centrifuge Model Testing of Liquefaction Mitigation via Microbially Induced Calcite Precipitation." *J. Geotech. Geoenviron. Eng.*, 145 (10): 04019084. https://doi.org/10.1061/(ASCE)GT.1943-5606.0002122.

De Melo, D. L., A. Kendall, and J. T. DeJong. 2023. "Review of Life Cycle Assessment (LCA) Evaluation of Geotechnical Systems." *Geo-Congress 2023*, 583–592. Los Angeles, California: American Society of Civil Engineers.

DeJong, J. T., M. Burrall, D. W. Wilson, and J. D. Frost. 2017. "A Bio-Inspired Perspective for Geotechnical Engineering Innovation." *Geotechnical Frontiers 2017*, 862–870. Orlando, Florida: American Society of Civil Engineers.

DeJong, J. T., M. G. Gomez, A. C. M. San Pablo, C. M. R. Graddy, D. C. Nelson, M. Lee, K. Ziotopoulou, M. El Kortbawi, B. M. Montoya, T-H. Kwon. State of the Art: MICP soil improvement and its application to liquefaction hazard mitigation 104. 2022.

DeJong, J. T., B. M. Mortensen, B. C. Martinez, and D. C. Nelson. 2010. "Bio-mediated soil improvement." *Ecological Engineering*, 36 (2): 197–210. https://doi.org/10.1016/j.ecoleng.2008.12.029.

El Ghoraiby, M., H. Park, and M. T. Manzari. 2020. "Physical and Mechanical Properties of Ottawa F65 Sand." *Model Tests and Numerical Simulations of Liquefaction and Lateral Spreading*, B. L. Kutter, M. T. Manzari, and M. Zeghal, eds., 45–67. Cham: Springer International Publishing.

Faruqi, A., C. A. Hall, and A. Kendall. 2023. “Sustainability of bio-mediated and bio-inspired ground improvement techniques for geologic hazard mitigation: a systematic literature review.” *Front. Earth Sci.*, 11: 1211574. https://doi.org/10.3389/feart.2023.1211574.

Feng, K., and B. M. Montoya. 2015. “Drained shear strength of MICP sand at varying cementation levels.” *IFCEE 2015*, 2242–2251. San Antonio, Texas: American Society of Civil Engineers.

Fujita, Y., J. L. Taylor, T. L. T. Gresham, M. E. Delwiche, F. S. Colwell, T. L. McLing, L. M. Petzke, and R. W. Smith. 2008. “Stimulation of microbial urea hydrolysis in groundwater to enhance calcite precipitation.” *Environ. Sci. Technol.*, 42 (8): 3025–3032. American Chemical Society. https://doi.org/10.1021/es702643g.

Gomez, M. G., and J. T. DeJong. 2017. “Engineering properties of bio-cementation improved sandy soils.” *Grouting 2017*, 23–33. Honolulu, Hawaii: American Society of Civil Engineers.

Graddy, C. M. R., M. G. Gomez, J. T. DeJong, and D. C. Nelson. 2021. “Native bacterial community convergence in augmented and stimulated ureolytic MICP biocementation.” *Environ. Sci. Technol.*, 55 (15): 10784–10793. American Chemical Society. https://doi.org/10.1021/acs.est.1c01520.

Idriss, I. M., and R. W. Boulanger. 2008. *Soil liquefaction during earthquakes*. Oakland, California, United States: Earthquake Engineering Research Institute (EERI).

Jefferies, M., and K. Been. 2016. University of Southampton, United Kingdom.

Karol, R. H. 2003. *Chemical grouting and soil stabilization*. Civil and environmental engineering. New York, NY: Dekker.

Kortbawi, M. E. 2022. “Constitutive Modeling of Bio-Cemented Sands for Earthquake Engineering Applications.”

Kutter, B. L., M. T. Manzari, and M. Zeghal (Eds.). 2020. *Model Tests and Numerical Simulations of Liquefaction and Lateral Spreading: LEAP-UCD-2017*. Cham: Springer International Publishing.

Lee, M., M. G. Gomez, M. El Kortbawi, and K. Ziotopoulou. 2021. “Effect of light biocementation on the liquefaction triggering and post-triggering behavior of loose sands.” *J. Geotech. Geoenviron. Eng.*, 148 (1): 04021170. https://doi.org/10.1061/(ASCE)GT.1943-5606.0002707.

Li, L., R. D. Beemer, and M. Iskander. 2021. “Granulometry of Two Marine Calcareous Sands.” *J. Geotech. Geoenviron. Eng.*, 147 (3): 04020171. https://doi.org/10.1061/(ASCE)GT.1943-5606.0002431.

Lin, H., M. T. Suleiman, D. G. Brown, and E. Kavazanjian. 2016. “Mechanical behavior of sands treated by microbially induced carbonate precipitation.” *J. Geotech. Geoenviron. Eng.*, 142 (2): 04015066. https://doi.org/10.1061/(ASCE)GT.1943-5606.0001383.

Lu, N., and J. K. Mitchell (Eds.). 2019. *Geotechnical Fundamentals for Addressing New World Challenges*. Springer Series in Geomechanics and Geoengineering. Cham: Springer International Publishing.

Montoya, B. M., and J. T. DeJong. 2015. “Stress-Strain Behavior of Sands Cemented by Microbially Induced Calcite Precipitation.” *Journal of Geotechnical and Geoenvironmental*

Engineering, 141 (6): 04015019. American Society of Civil Engineers. https://doi.org/10.1061/(ASCE)GT.1943-5606.0001302.

Montoya, B. M., J. Do, and M. A. Gabr. 2021. "Distribution and Properties of Microbially Induced Carbonate Precipitation in Underwater Sand Bed." *J. Geotech. Geoenviron. Eng.*, 147 (10): 04021098. https://doi.org/10.1061/(ASCE)GT.1943-5606.0002607.

Montoya, B. M., R. Gerhard, J. T. DeJong, D. W. Wilson, M. H. Weil, B. C. Martinez, and L. Pederson. 2012. "Fabrication, Operation, and Health Monitoring of Bender Elements for Aggressive Environments." *Geotech. Test. J.*, 35 (5): 103300. https://doi.org/10.1520/GTJ103300.

Na, K., A. Cabas, and B. M. Montoya. 2023. "Resonant Column Testing Procedure for Microbial-Induced Carbonate-Precipitated Sands." *Geotech. Test. J.*, 46 (2): 20220056. https://doi.org/10.1520/GTJ20220056.

Nafisi, A., A. Khoubani, B. M. Montoya, and T. M. Evans. 2018. "The effect of grain size and shape on mechanical behavior of MICP sand I: Experimental study." 9.

Ribeiro, B. G. O., and M. G. Gomez. 2023. "Dissolution Behavior of Ureolytic Biocementation: Physical Experiments and Reactive Transport Modeling." *J. Geotech. Geoenviron. Eng.*, 149 (9): 04023071. https://doi.org/10.1061/JGGEFK.GTENG-11275.

Riveros, G. A., and A. Sadrekarimi. 2020. "Liquefaction resistance of Fraser River sand improved by a microbially-induced cementation." *Soil Dynamics and Earthquake Engineering*, 131: 106034. https://doi.org/10.1016/j.soildyn.2020.106034.

San Pablo, A. C. M., J. T. DeJong, and T. J. Carey. 2024. "Influence of biocementation treatment extent on dynamic system performance: A centrifuge liquefaction study." *Soil Dynamics and Earthquake Engineering*, 183: 108792. https://doi.org/10.1016/j.soildyn.2024.108792.

San Pablo, A. C. M., M. Lee, C. M. R. Graddy, C. M. Kolbus, M. Khan, A. Zamani, N. Martin, C. Acuff, J. T. DeJong, M. G. Gomez, and D. C. Nelson. 2020. "Meter-Scale Biocementation Experiments to Advance Process Control and Reduce Impacts: Examining Spatial Control, Ammonium By-Product Removal, and Chemical Reductions." *J. Geotech. Geoenviron. Eng.*, 146 (11): 04020125. American Society of Civil Engineers. https://doi.org/10.1061/(ASCE)GT.1943-5606.0002377.

Santamarina, J.C., Klein, A. & Fam, M.A. Soils and waves: Particulate materials behavior, characterization and process monitoring. J Soils Sediments 1, 130 (2001). https://doi.org/10.1007/BF02987719

Sharma, S. 2004. "CHARACTERISATION OF CYCLIC BEHAVIOUR OF CALCITE CEMENTED CALCAREOUS SOILS."

Sharma, S. S., and M. A. Ismail. 2006. "Monotonic and Cyclic Behavior of Two Calcareous Soils of Different Origins." *J. Geotech. Geoenviron. Eng.*, 132 (12): 1581–1591. https://doi.org/10.1061/(ASCE)1090-0241(2006)132:12(1581).

Stocks-Fischer, S., J. K. Galinat, and S. S. Bang. 1999. "Microbiological precipitation of $CaCO_3$." *Soil Biology and Biochemistry*, 31 (11): 1563–1571. https://doi.org/10.1016/S0038-0717(99)00082-6.

Terzis, D., and L. Laloui. 2017. “On the Application of Microbially Induced Calcite Precipitation for Soils: A Multiscale Study.” *Advances in Laboratory Testing and Modelling of Soils and Shales (ATMSS)*, Springer Series in Geomechanics and Geoengineering, A. Ferrari and L. Laloui, eds., 388–394. Cham: Springer International Publishing.

Vasko, A. 2013. “An Investigation into the Behavior of Ottawa Sand through Monotonic and Cyclic Shear Tests.”

Watson, P., Bransby, F., Delimi, Z. L., Erbrich, C., Finnie, I., Krisdani, H., ... & Westgate, Z. (2019). Foundation design in offshore carbonate sediments–building on knowledge to address future challenges. In *From Research to Applied Geotechnics* (pp. 240-274). IOS Press.

Xiao, P., H. Liu, Y. Xiao, A. W. Stuedlein, and T. M. Evans. 2018. “Liquefaction resistance of bio-cemented calcareous sand.” *Soil Dynamics and Earthquake Engineering*, 107: 9–19. https://doi.org/10.1016/j.soildyn.2018.01.008.

Yang, Z. X., and K. Pan. 2017. “Flow deformation and cyclic resistance of saturated loose sand considering initial static shear effect.” *Soil Dynamics and Earthquake Engineering*, 92: 68–78. https://doi.org/10.1016/j.soildyn.2016.09.002.

Ye, B., X. Ni, Y. Huang, and F. Zhang. 2018. “Unified modeling of soil behaviors before/after flow liquefaction.” *Computers and Geotechnics*, 102: 125–135. https://doi.org/10.1016/j.compgeo.2018.06.011.

Zamani, A., P. Xiao, T. Baumer, T. J. Carey, B. Sawyer, J. T. DeJong, and R. W. Boulanger. 2021. “Mitigation of Liquefaction Triggering and Foundation Settlement by MICP Treatment.” *Journal of Geotechnical and Geoenvironmental Engineering*, 147 (10): 04021099. American Society of Civil Engineers. https://doi.org/10.1061/(ASCE)GT.1943-5606.0002596.

Table 1. Soil Properties

Soil	Mineralogy	D_{50}	C_u	C_c	G_s	Measured e_{min}	Literature e_{min}	Measured e_{max}	Literature e_{max}
Ottawa F-65	Silica	0.206	1.71	0.99	2.65	0.53	0.51 (Kutter et al. 2017)	0.84	0.78 (Kutter et al. 2017)
30% LP 70% Ottawa F-65	30% Carbonate	0.218	1.59	0.98	2.68	0.61	No literature values	0.89	No literature values
Ledge Point (LP)	Carbonate	0.224	1.54	0.98	*2.76 (Cai and Rutherford 2023)	Not measured	*0.90 (Sharma 2004)	Not measured	*1.21 (Sharma 2004)

*Unsieved ledge point sand

Table 2. Treatment Scheme

Treatments per Specimen	Solution Volume	Bacteria Pellets	Yeast Extract (g/L)	Ammonium Chloride (mM)	Urea (mM)	Calcium Chloride (mM)
Augmentation	4 PV	2	0.2	100	10	-
Cementation	2 PV	-	0.2	100	250	250

Table 3. Test Matrix

		Uncemented				Cemented							
	ΔVs	0				150				300			
	Confinement	Loose 35%		Medium 60%		Loose 35%		Medium 60%		Loose 35%		Medium 60%	
Drained	100	100S	70S30C	100S		100S	70S30C			100S	70S30C		
	300	100S	70S30C										
	500	100S	70S30C										
	900	100S											
Undrained	100	100S	70S30C	100S		100S				100S			
	300	100S	70S30C										
	1000	100S											
	CSR												
Cyclic	0.08			100S									
	0.09	100S	70S30C										
	0.1	100S		100S	70S30C								
	0.12	100S	70S30C	70S30C	70S30C								
	0.13			100S									
	0.15	70S30C	70S30C	100S	70S30C								
	0.2					100S	70S30C						
	0.25					100S	70S30C						
	0.3					70S30C		100S					
	0.35					100S	70S30C	100S		70S30C	70S30C		
	0.4							100S				100S	
	0.45									70S30C	70S30C		
	0.5									100S		100S	
	0.55									100S	70S30C		
	0.6									100S		100S	
	0.7											100S	

Table 4. Drained Results Summary

Properties at End of Consolidation				Post Cementation Properties				Peak		20% Strain			
Soil Type	Confining Pressure, σ'_{3c} (kPa)	Relative Density, D_R (%)	State Parameter, ξ	ΔD_R Cementation	Achieved ΔV_S (m/s)	Average Calcite (%)	Std. Calcite (%)	Deviatoric Stress (kPa)	Friction Angle (deg)	Void Ratio	Mean Eff. Stress (kPa)	Friction Angle	ψ'_{max} (deg)
100S	300	Loose: 37 %	-0.02	0%	0	0.0%	-	683	32.2	0.73	522	31.7	0.5
100S	500	Loose: 37 %	-0.02	0%	0	0.0%	-	1130	32.0	0.72	868	31.5	0.5
100S	900	Loose: 35 %	0.00	0%	0	0.0%	-	1994	31.7	0.72	1552	31.3	0.4
100S	100	Loose: 39 %	-0.04	0%	0	0.0%	-	239	33.0	0.75	178	32.1	0.9
100S	100	Dense: 64 %	-0.12	0%	0	0.0%	-	334	38.7	0.71	180	33.8	4.9
100S	100	Dense: 56 %	-0.09	0%	0	0.0%	-	280	35.9	0.73	177	32.7	3.2
100S	100	Loose: 39 %	-	10%	168	1.8%	1.3%	255	34.1	0.74	181	33	1.1
100S	100	Loose: 42 %	-	12%	264	2.3%	0.2%	275	35.5	0.74	180	32.9	2.6
70S30C	100	Loose: 19 %	-0.03	0%	0	0.0%	-	268	35.1	0.86	182	33.7	1.4
70S30C	300	Loose: 28 %	-0.04	0%	0	0.0%	-	811	35.1	0.83	547	33.7	1.4
70S30C	500	Loose: 29 %	-0.03	0%	0	0.0%	-	1332	34.9	0.81	901	33.1	1.8
70S30C	100	Loose: 30 %	-	7%	152	1.1%	0.7%	268	35.1	0.85	182	33.6	1.5
70S30C	100	Loose: 37 %	-	14%	299	2.2%	0.8%	306	37.2	0.84	183	33.1	4.1

Table 5. Undrained Results Summary

Properties at End of Consolidation				Post Cementation Properties				Peak		20% Strain			
Soil Type	Confining Pressure, σ'_{3c} (kPa)	Relative Density, D_R (%)	State Parameter, ξ	ΔD_R Cementation	Achieved ΔV_S (m/s)	Average Calcite (%)	Std. Calcite (%)	Deviatoric Stress (kPa)	Friction Angle (deg)	Void Ratio	Mean Eff. Stress (kPa)	Friction Angle	ψ'_{max} (deg)
100S	100	Loose: 35 %	-0.03	0%	0	0.0%	-	39	39	0.73	552	31.4	7.3
100S	300	Loose: 36 %	-0.02	0%	0	0.0%	-	233	32.6	0.73	1208	31.2	1.4
100S	1000	Loose: 37 %	-0.01	0%	0	0.0%	-	665	31.4	0.73	1334	30.6	0.8
100S	100	Dense: 56 %	-0.09	0%	0	0.0%	-	1795	34	0.67	1995	34.0	0
100S	100	Dense: 45 %	-	12%	164	2.1%	0.6%	185	31.9	0.70	1019	30.7	1.2
100S	100	Dense: 41 %	-	12%	265	2.2%	0.2%	352	32.3	0.71	1079	30.0	2.3
70S30C	1000	Loose: 36 %	-0.02	0%	0	0.0%	-	1306	34.2	0.79	1079	33.4	0.8
70S30C	300	Loose: 30 %	-0.04	0%	0	0.0%	-	630	34.1	0.81	848	33.3	0.8

Table 6. Cyclic Results Summary

Properties at End of Consolidation				Post Cementation Properties								Pre Triggering Results				Post Triggering Results		
Soil Type	Loading CSR	Relative Density, D_R (%)	State Parameter, ξ	ΔD_R Cementation	Achieved ΔV_S (m/s)	Location of Observed Failure	Location of Minimum Calcite	Minimum Calcite (%)	Maximum Calcite (%)	Average Calcite (%)	Std. Calcite (%)	Cycles to r_u=0.475	Cycles to r_u=0.95	Cycles to 3% SASS	Cycles between 3% and r_u=0.95	Cycles to 5% SASS	Cycles to 9% SASS	Cycles from 3% to 9% SASS
100S	0.09	Loose: 34 %	-0.02	0%	0			0.0%	0.0%	0.0%	-	10.18	19.96	19.74	-0.22	19.76	20.67	0.93
100S	0.1	Loose: 27 %	0.00	0%	0			0.0%	0.0%	0.0%	-	5.26	7.79	7.8	0.01	7.85	8.92	1.12
100S	0.12	Loose: 30 %	-0.01	0%	0			0.0%	0.0%	0.0%	-	1.74	1.76	1.77	0.01	1.79	1.84	0.07
100S	0.1	Dense: 54 %	-0.08	0%	0			0.0%	0.0%	0.0%	-	27.18	53	53.57	0.57	54.58	57.7	4.13
100S	0.13	Dense: 61 %	-0.11	0%	0			0.0%	0.0%	0.0%	-	5.26	25.04	27.56	2.52	28.64	39.74	12.18
100S	0.15	Dense: 59 %	-0.10	0%	0			0.0%	0.0%	0.0%	-	2.11	2.99	3.55	0.56	3.7	6.7	3.15
100S	0.2	Loose: 29 %	-	5%	141	Top	Middle	0.8%	1.0%	0.9%	0.1%	18.24	35	35.56	0.56	36.59	38.68	3.12
100S	0.25	Loose: 30 %	-	5%	139	Top	Middle	0.7%	1.0%	0.9%	0.2%	2.23	6.01	6.65	0.64	7.59	9.68	3.03
100S	0.35	Loose: 26 %	-	5%	169	Top-Middle	Middle	0.8%	1.0%	0.9%	0.1%	0.95	1	0.72	-0.28	1.6	1.73	1.01
100S	0.3	Dense: 58 %	-	0%	147		Top	0.7%	0.9%	0.8%	0.1%	11.23	43.01	45.62	2.61	47.62	52.67	7.05
100S	0.35	Dense: 52 %	-	3%	117		Middle	0.4%	0.9%	0.6%	0.3%	0.96	1.01	1.56	0.55	2.57	3.72	2.16
100S	0.4	Dense: 59 %	-	5%	153	Top	Bottom	0.5%	1.1%	0.9%	0.3%	0.97	1.02	2.57	1.55	3.61	6.65	4.08
100S	0.5	Loose: 22 %	-	16%	443	Top	Top	2.8%	3.1%	3.0%	0.2%	10.25	40.03	45.64	5.61	48.71	52.69	7.05
100S	0.55	Loose: 23 %	-	14%	303	Top-Middle	Top	2.3%	2.9%	2.5%	0.4%	1.11	6.01	7.69	1.68	9.69	12.67	4.98
100S	0.6	Loose: 23 %	-	12%	220	Middle-Bottom	Bottom	0.9%	3.1%	2.2%	1.1%	0.98	1	1.56	0.56	1.7	4.7	3.14
100S	0.5	Dense: 60 %	-	10%	293	Top	Bottom	1.5%	2.4%	2.0%	0.5%	61.2	107.04	116.7	9.66	124.65	128.67	11.97
100S	0.6	Dense: 55 %	-	14%	318	Top	Bottom	2.1%	3.4%	2.8%	0.7%	0.16	23.07	47.74	24.67	65.66	68.72	20.98
100S	0.7	Dense: 58 %	-	17%	307	Bottom	Middle	2.7%	3.6%	3.2%	0.4%	15.23	151.19	231.67	80.48	249.69	253.75	22.08
70S30C	0.09	Loose: 21 %	-0.04	0%	0			0.0%	0.0%	0.0%	-	85.23	187.94	187.75	-0.19	187.78	188.7	0.95
70S30C	0.12	Loose: 20 %	-0.04	0%	0			0.0%	0.0%	0.0%	-	12.13	17.8	17.75	-0.05	17.78	17.83	0.08
70S30C	0.15	Loose: 29 %	-0.06	0%	0			0.0%	0.0%	0.0%	-	1.21	1.73	1.73	0	1.76	1.81	0.08
70S30C	0.09	Dense: 41 %	-0.10	0%	0			0.0%	0.0%	0.0%	-	55.19	146.95	146.74	-0.21	146.76	147.65	0.91
70S30C	0.1	Dense: 36 %	-0.08	0%	0			0.0%	0.0%	0.0%	-	18.2	38.96	38.78	-0.18	38.8	39.65	0.87
70S30C	0.13	Dense: 60 %	-0.15	0%	0			0.0%	0.0%	0.0%	-	9.24	15.98	15.77	-0.21	15.79	16.63	0.86
70S30C	0.2	Loose: 24 %	-	5%	142	Top	Top	1.9%	3.0%	2.4%	0.6%	20.24	48.01	48.65	0.64	49.59	49.68	1.03
70S30C	0.3	Loose: 21 %	-	9%	151	Top	Middle	0.4%	2.6%	1.4%	1.1%	1.75	2	1.74	-0.26	1.77	2.67	0.93
70S30C	0.35	Loose: 65 %	-	11%	327		Middle	1.6%	2.2%	1.9%	0.3%	0.94	1	0.75	-0.25	1.59	1.65	0.9
70S30C	0.45	Loose: 28 %	-	11%	295		Middle	0.9%	2.6%	1.7%	0.9%	1.96	2	1.74	-0.26	2.58	2.71	0.97
70S30C	0.55	Loose: 24 %	-	9%	290		Top	1.3%	1.6%	1.4%	0.2%	0.97	1.01	0.74	-0.27	1.59	1.64	0.9

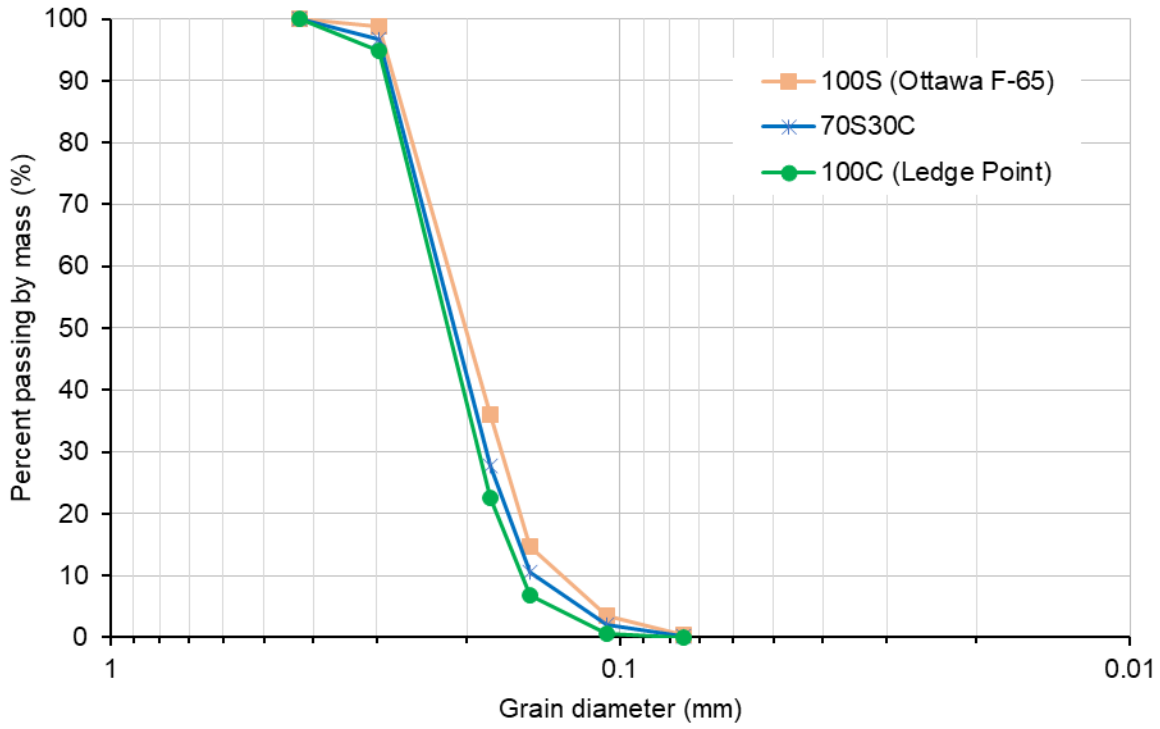

Figure 1. Gradations of 100S (Ottawa F-65), 70S30C, and sieved Ledge Point sands.

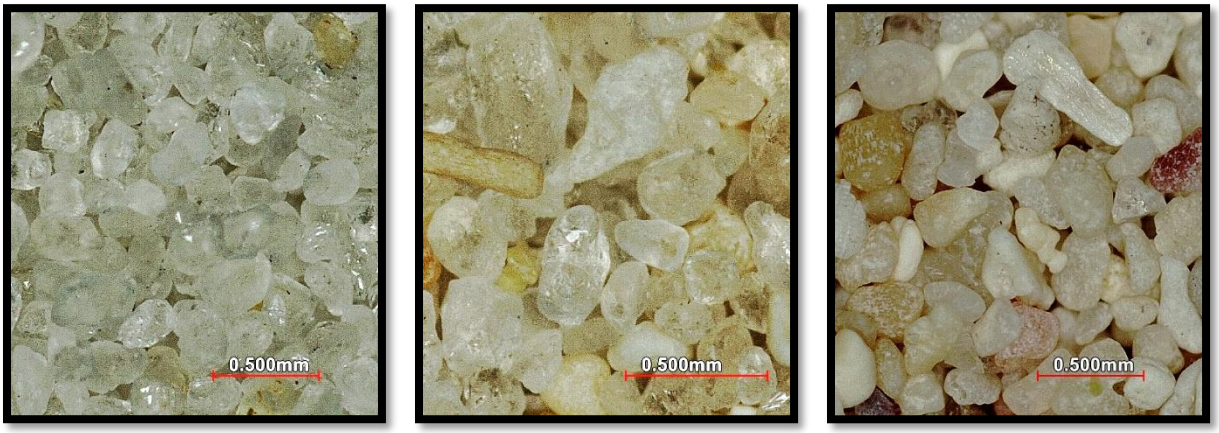

Figure 2. Enlarged images from left to right show 100S (Ottawa F-65), 70S30C sand, sieved Ledge Point sand.

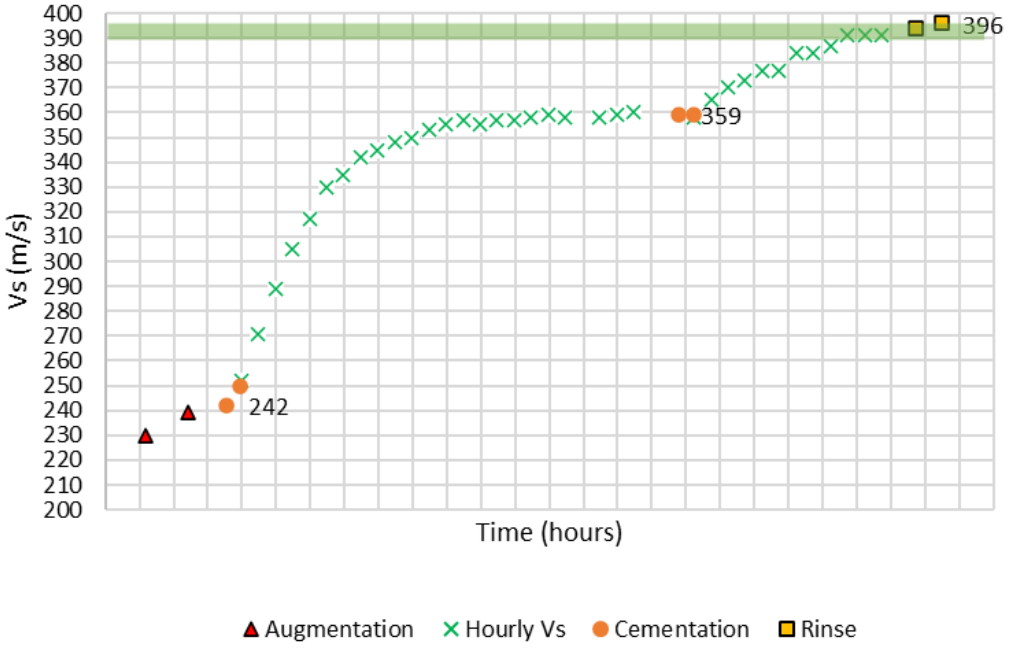

Figure 3. Shear wave velocity during the treatment process.

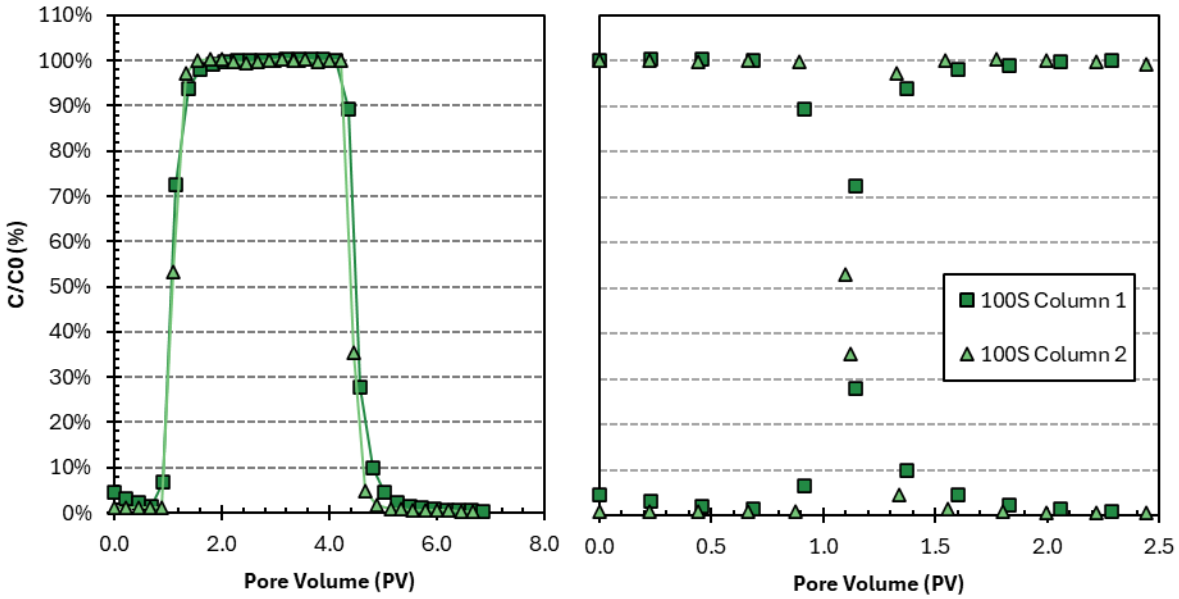

Figure 4. The bromide tracer breakthrough curve shows the normalized conductivity (C/C_0) versus injected pore volumes. This test was only completed on 2 identical columns to inform the volume of necessary treatment solution. The plot on the left shows the entire test while the plot on the right reset the pore volume to zero at 3 pore volumes when the DI water was started.

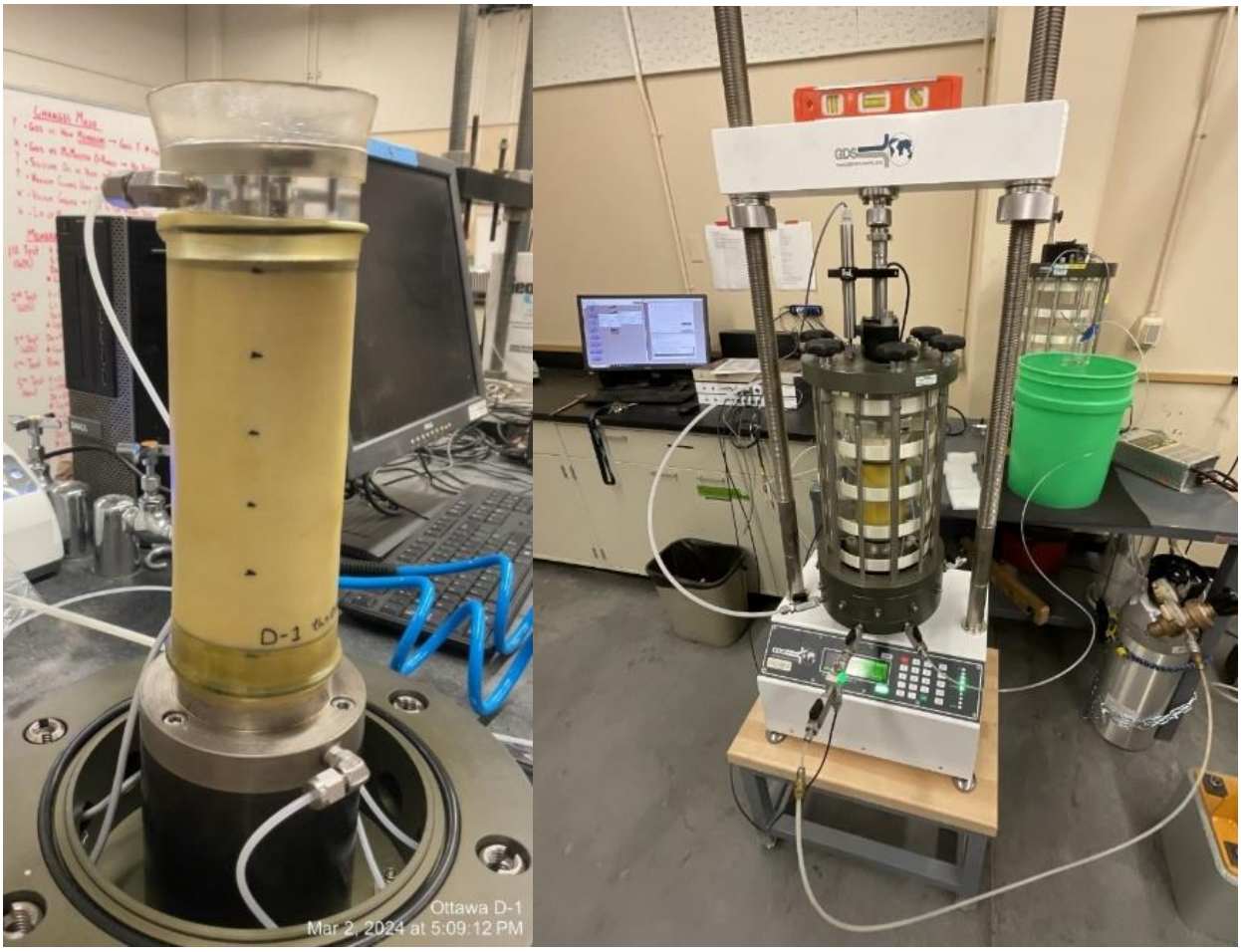

Figure 5. Triaxial setup: base pedestal with specimen (left), and specimen on load frame (right).

Figure 6. Specimen cut into segments for drying.

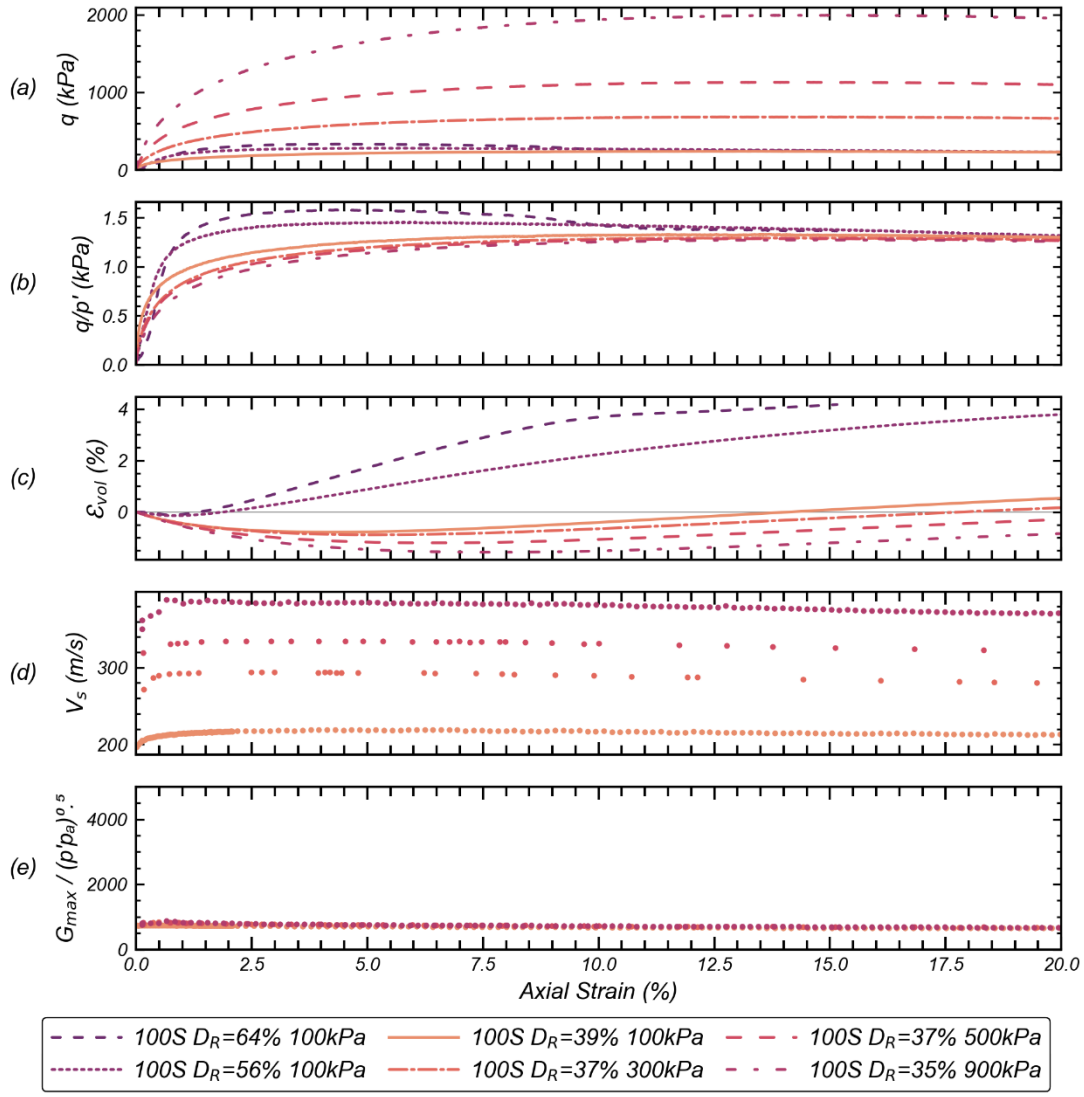

Figure 7. Isotropically consolidated drained tests on uncemented 100S sand.

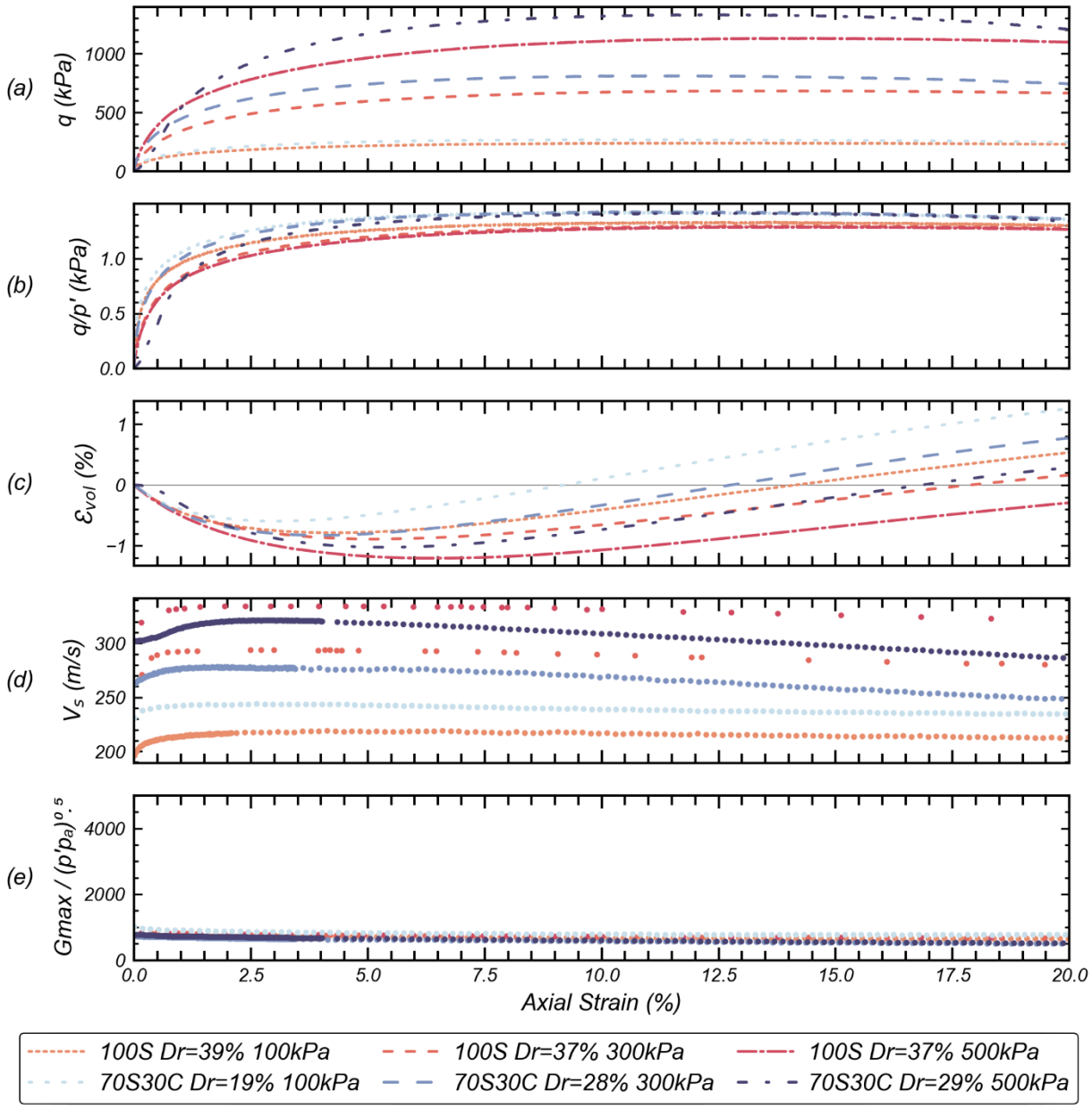

Figure 8. Isotropically consolidated drained triaxial tests comparing 100S sand and the 70S30C sand.

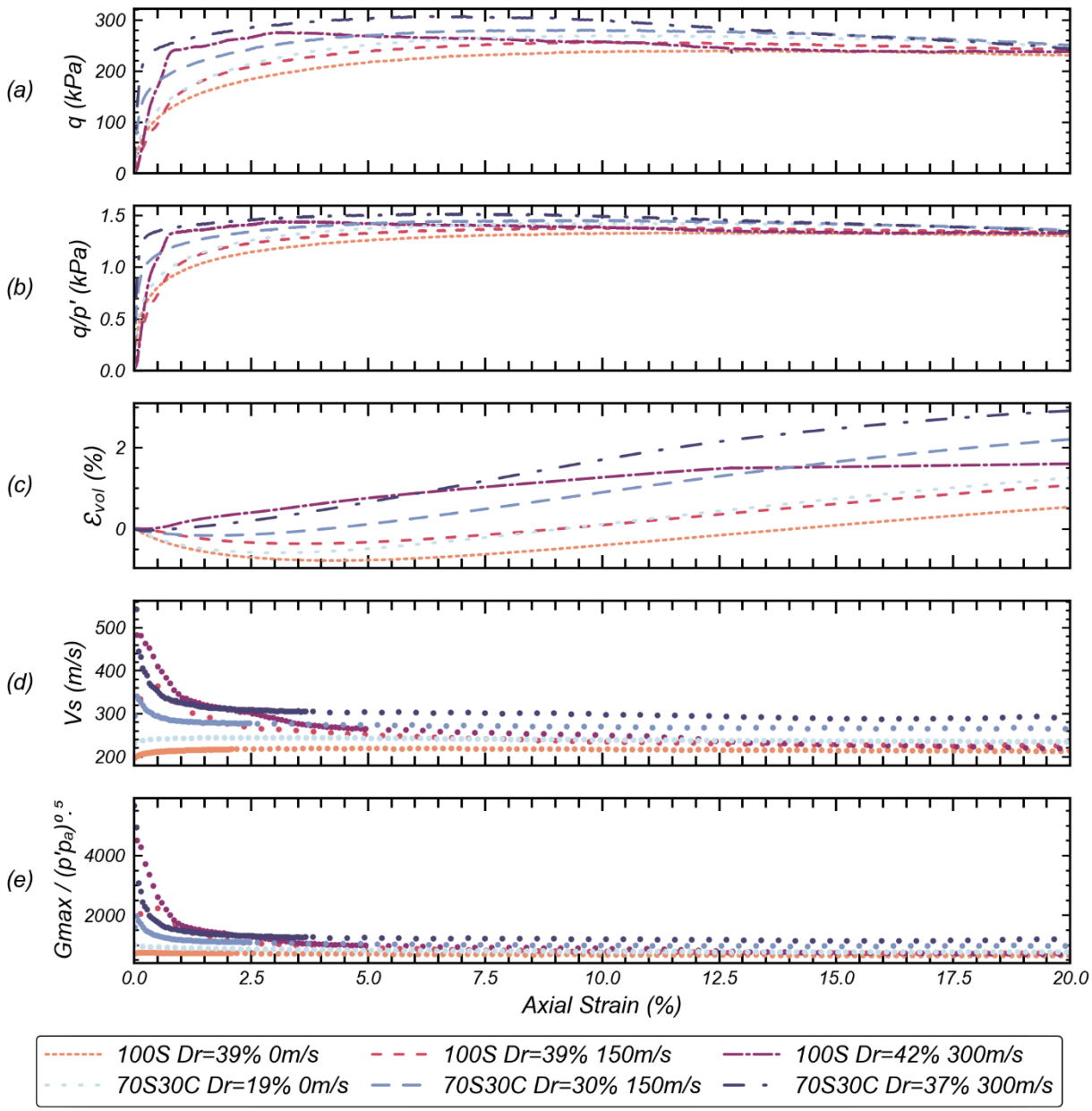

Figure 9. Isotropically consolidated drained tests comparing uncemented and bio-cemented specimens with both 100S and 70S30C sand. Specimens were prepared in a loose state, with shear wave velocities of 0 m/s (uncemented), 150 m/s, and 300 m/s.

Figure 10. Shear band observed in 100S moderately cemented specimen at 7% strain.

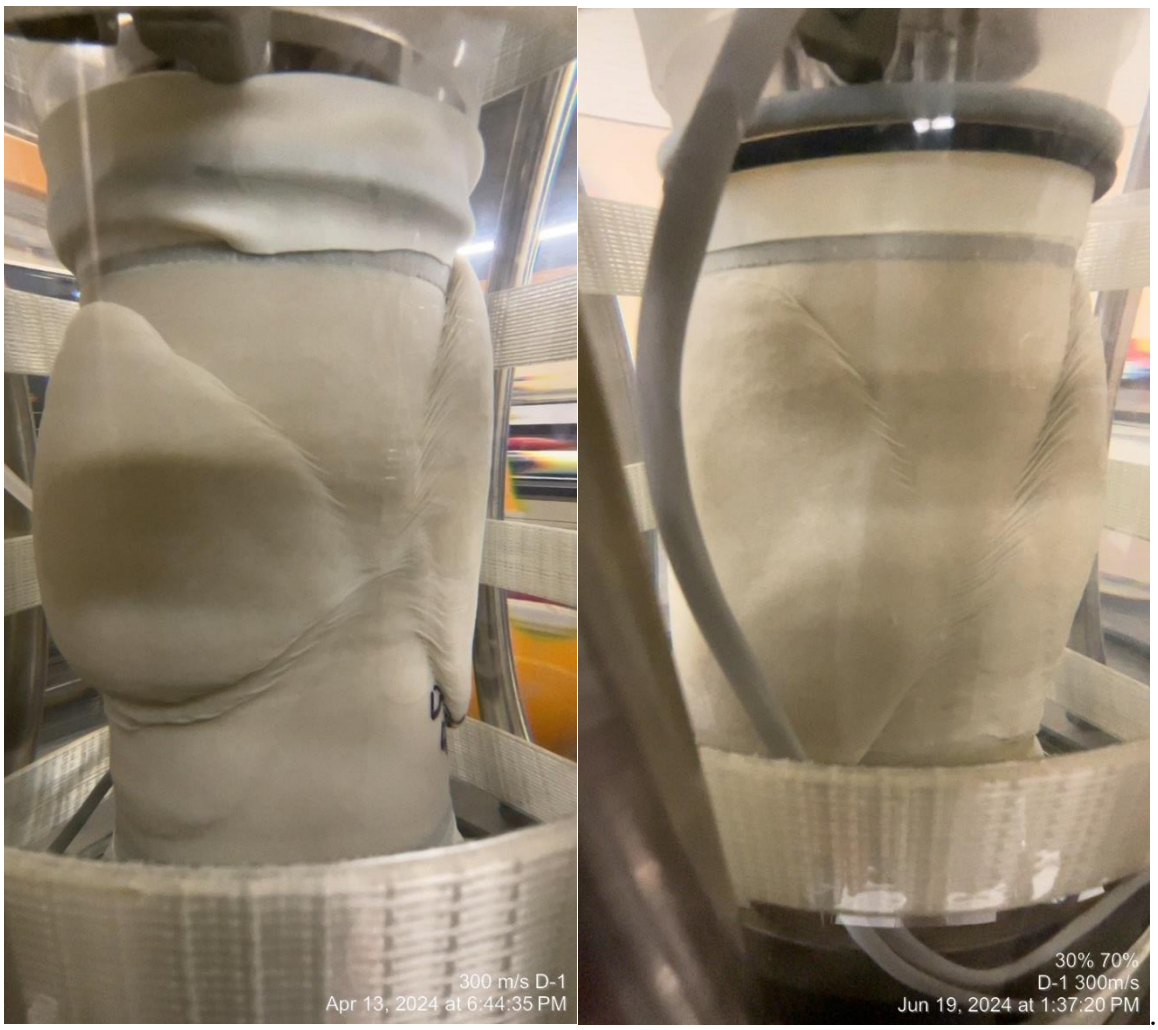

Figure 11. Shear band on loose 100S (left) and 70S30C (right) moderately cemented specimens.

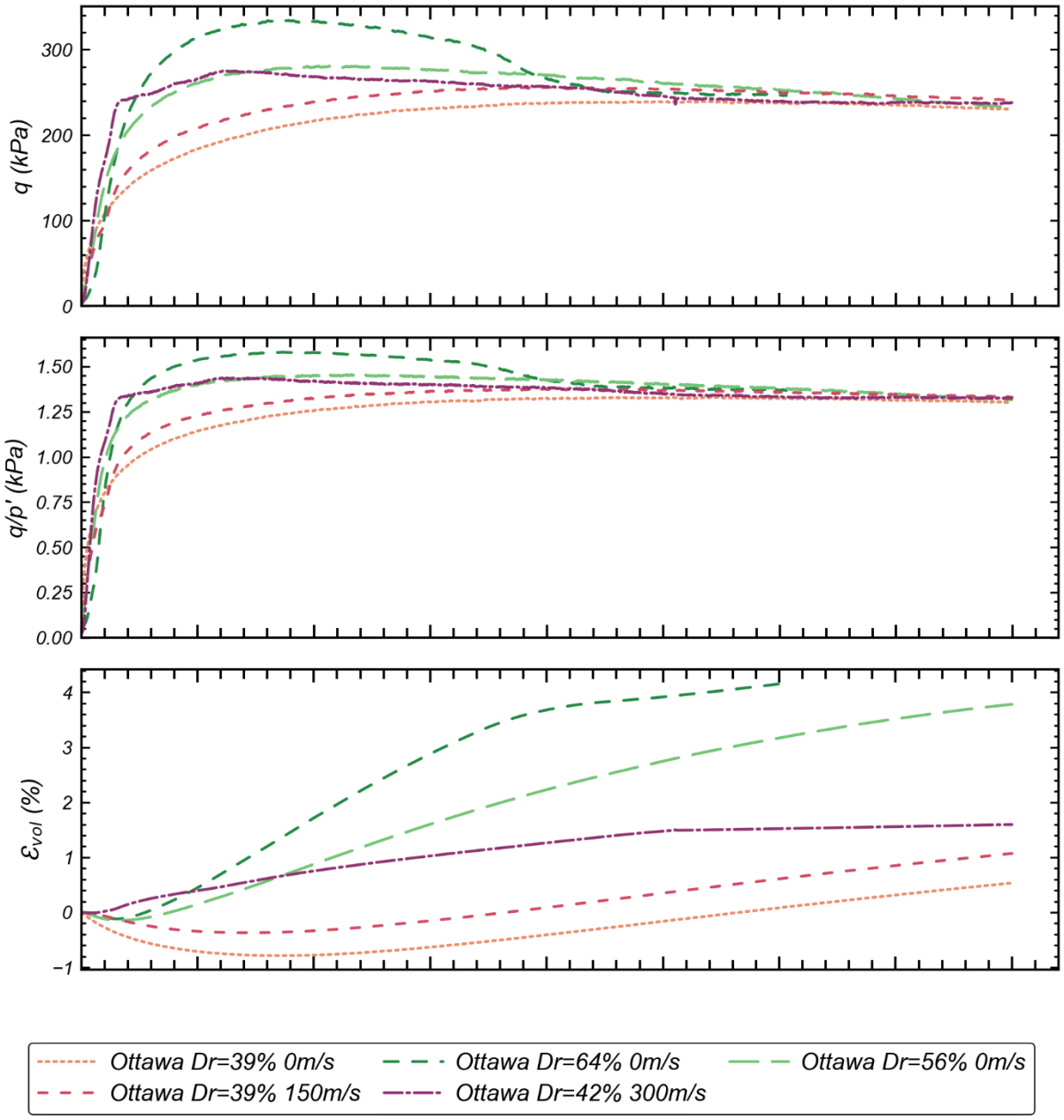

Figure 12. Comparing MICP treated loose specimens and uncemented dense specimens.

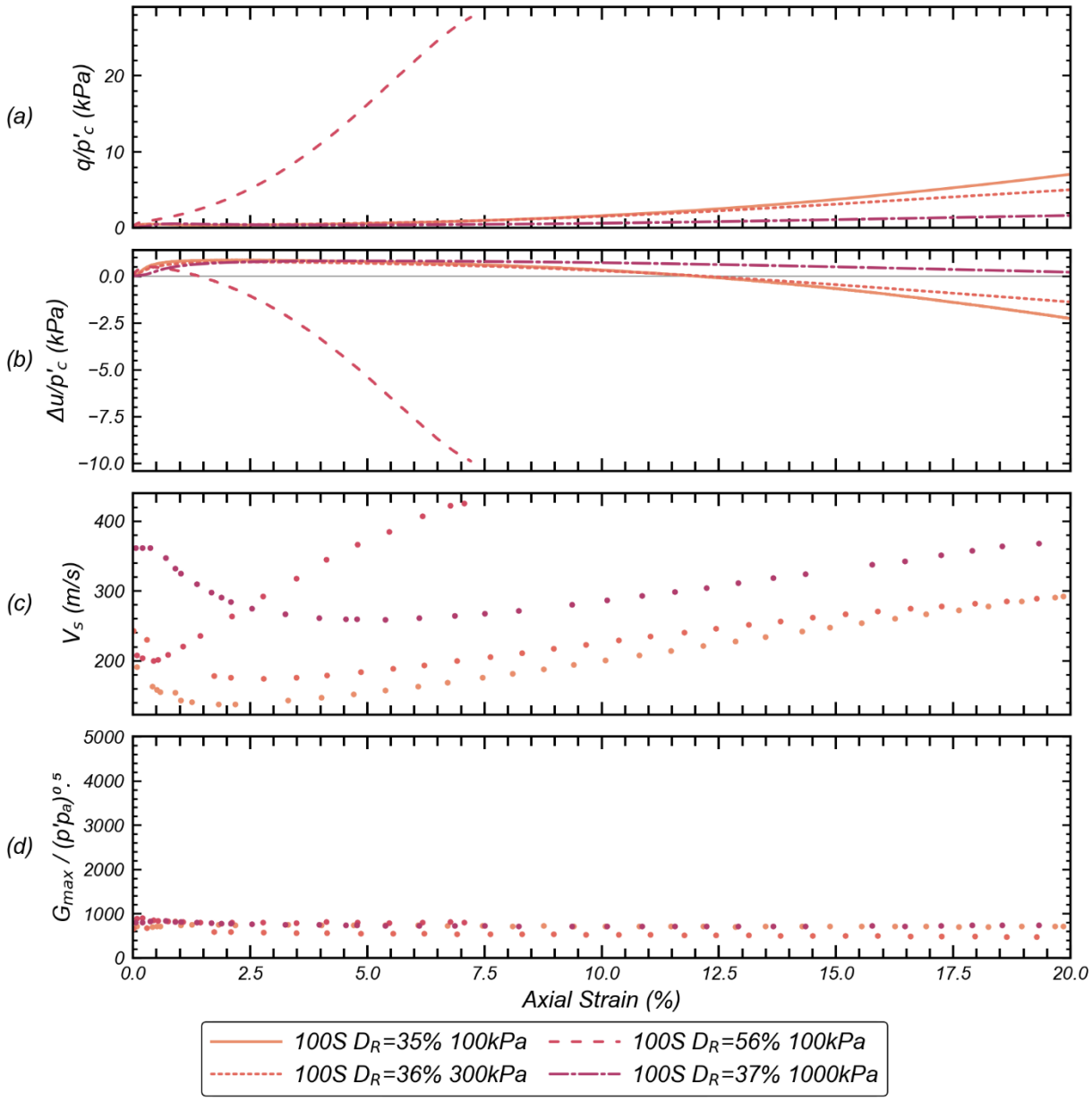

Figure 13. Isotropically consolidated undrained tests with uncemented 100S sand.

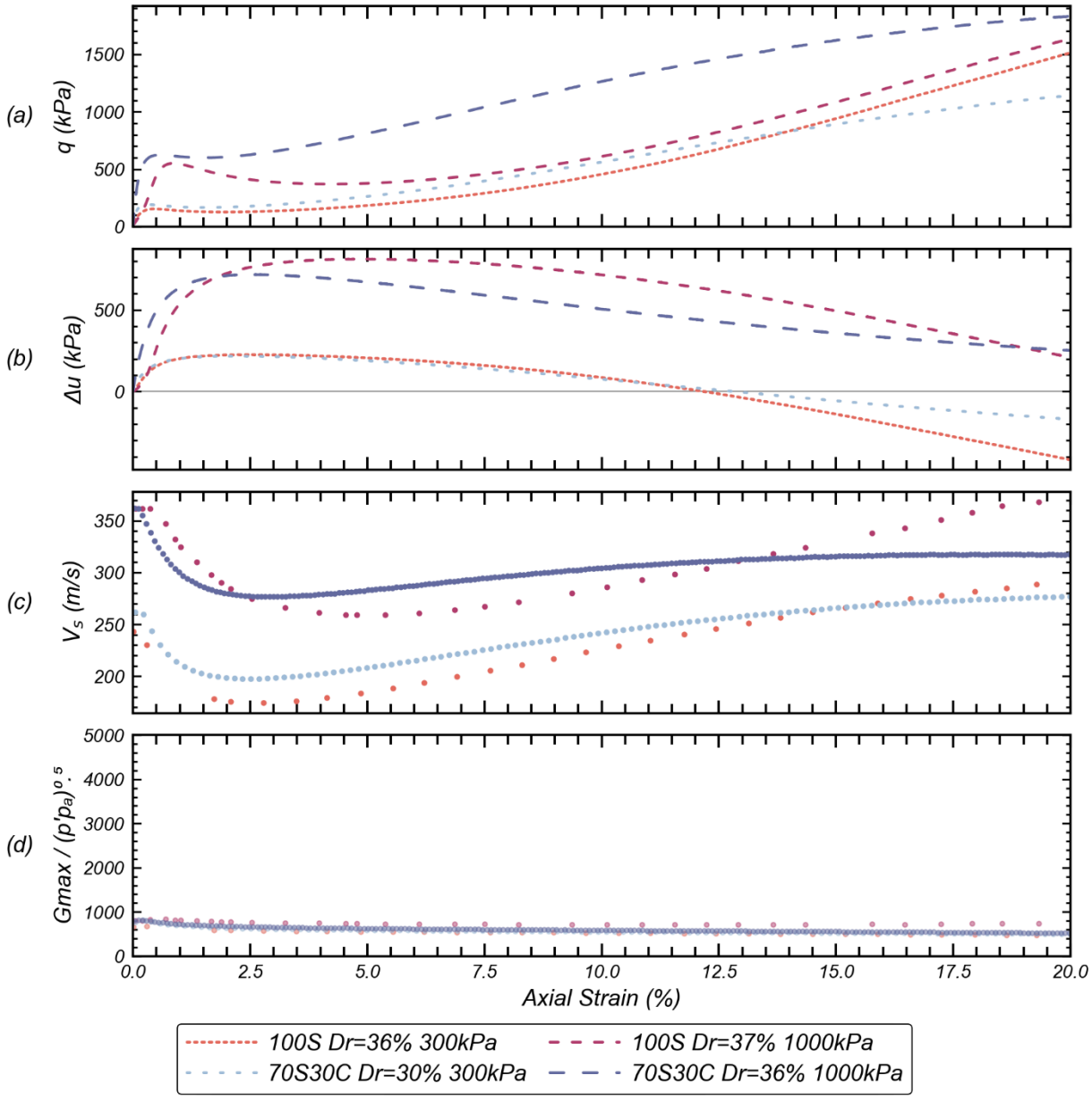

Figure 14. Isotropically consolidated undrained test comparing 100S and 70S30C sand at confining pressures of 300kPa and 1000kPa.

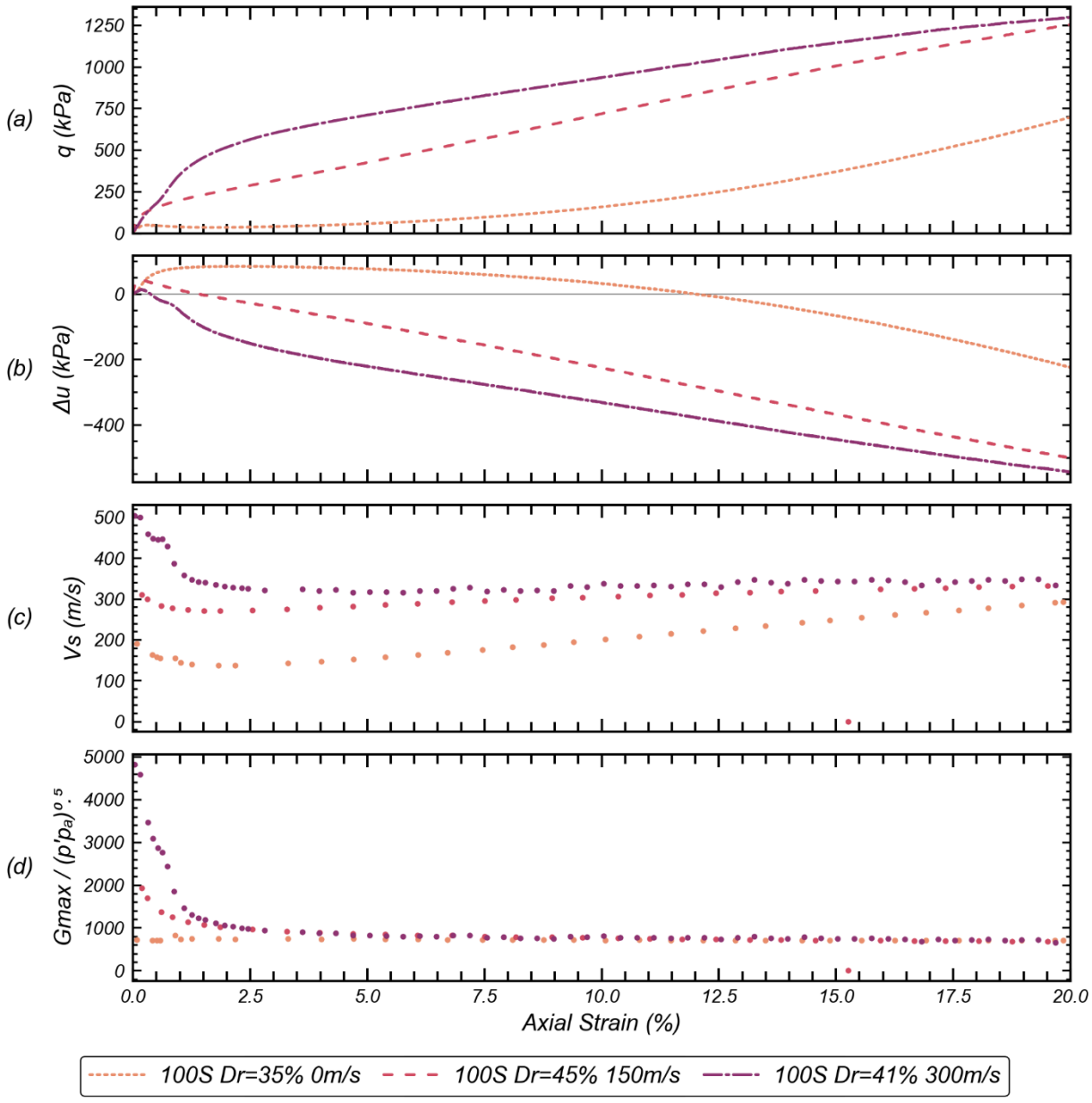

Figure 15. Isotropically consolidated undrained tests with Ottawa F-65 sand. Specimens were loosely prepared and cemented to 0m/s (uncemented), 150m/s, and 300m/s.

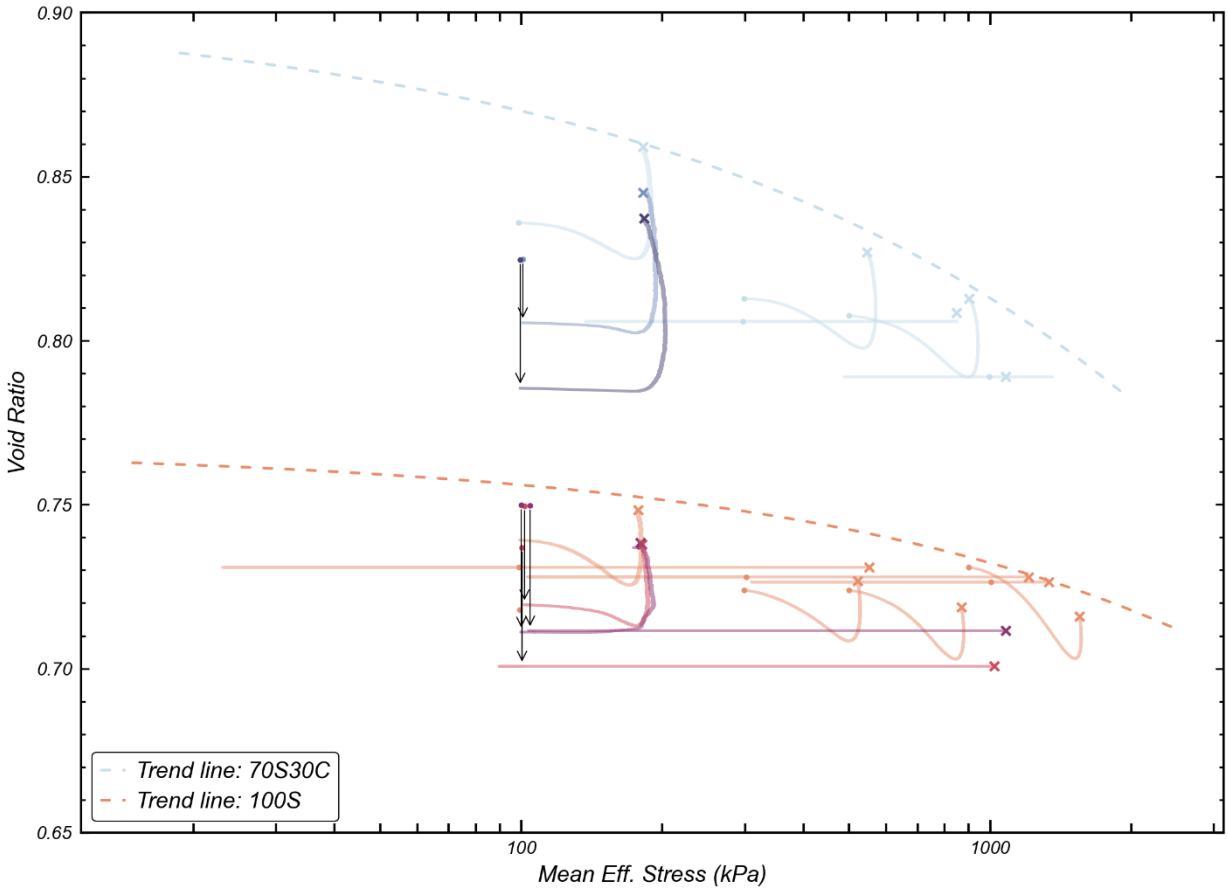

Figure 16. Critical state lines for 100S and 70S30C sand.

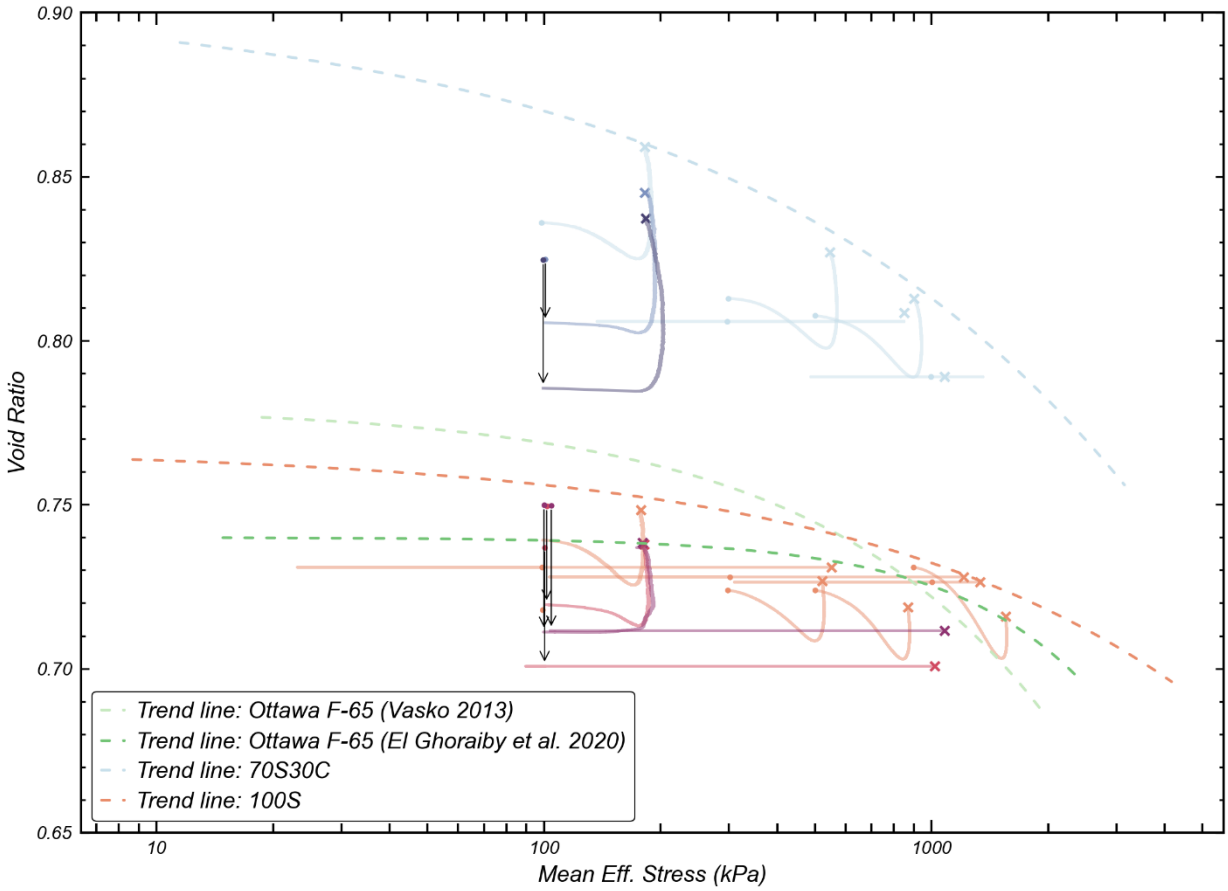

Figure 17. Critical state trends compared to literature values.

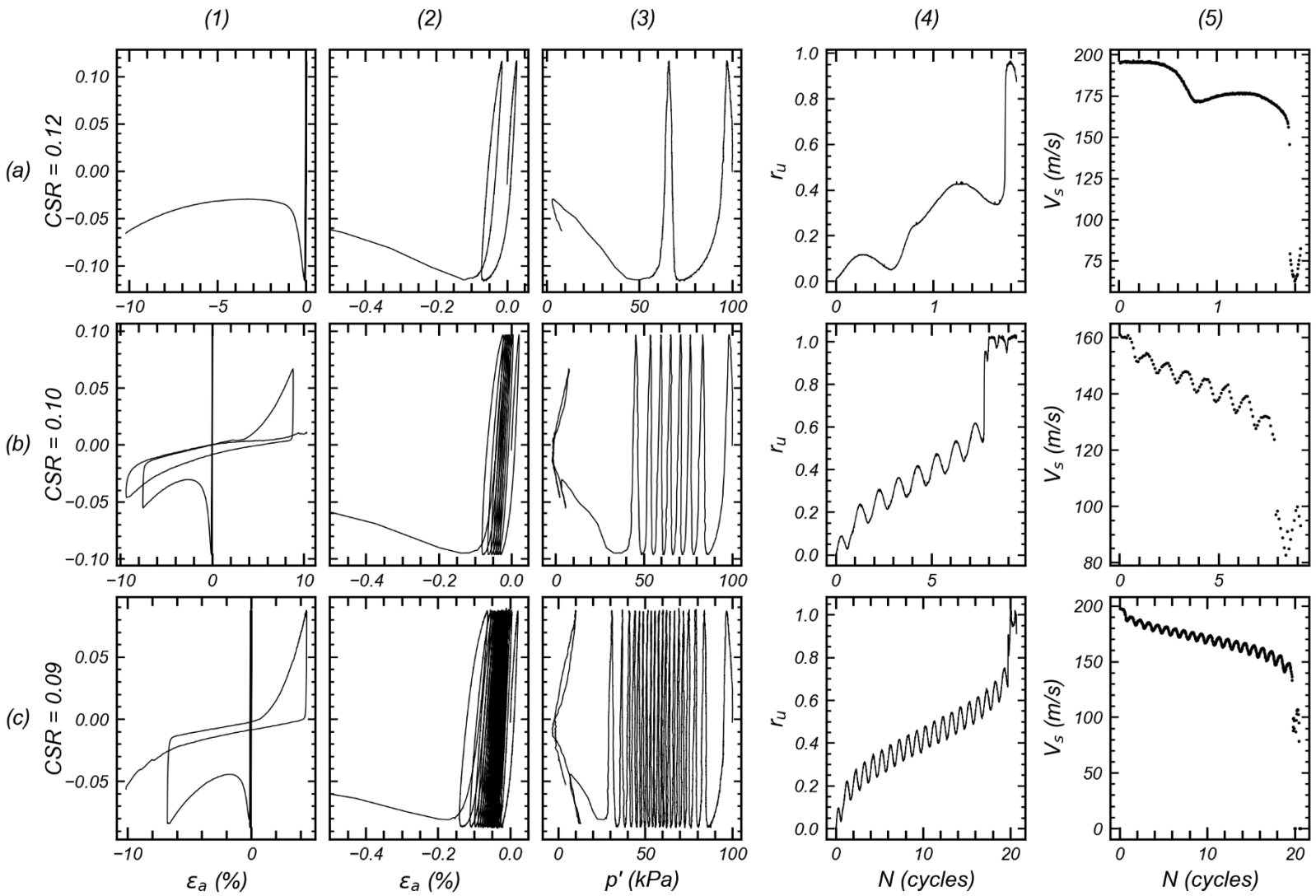

Figure 18. Uncemented loose 100S.

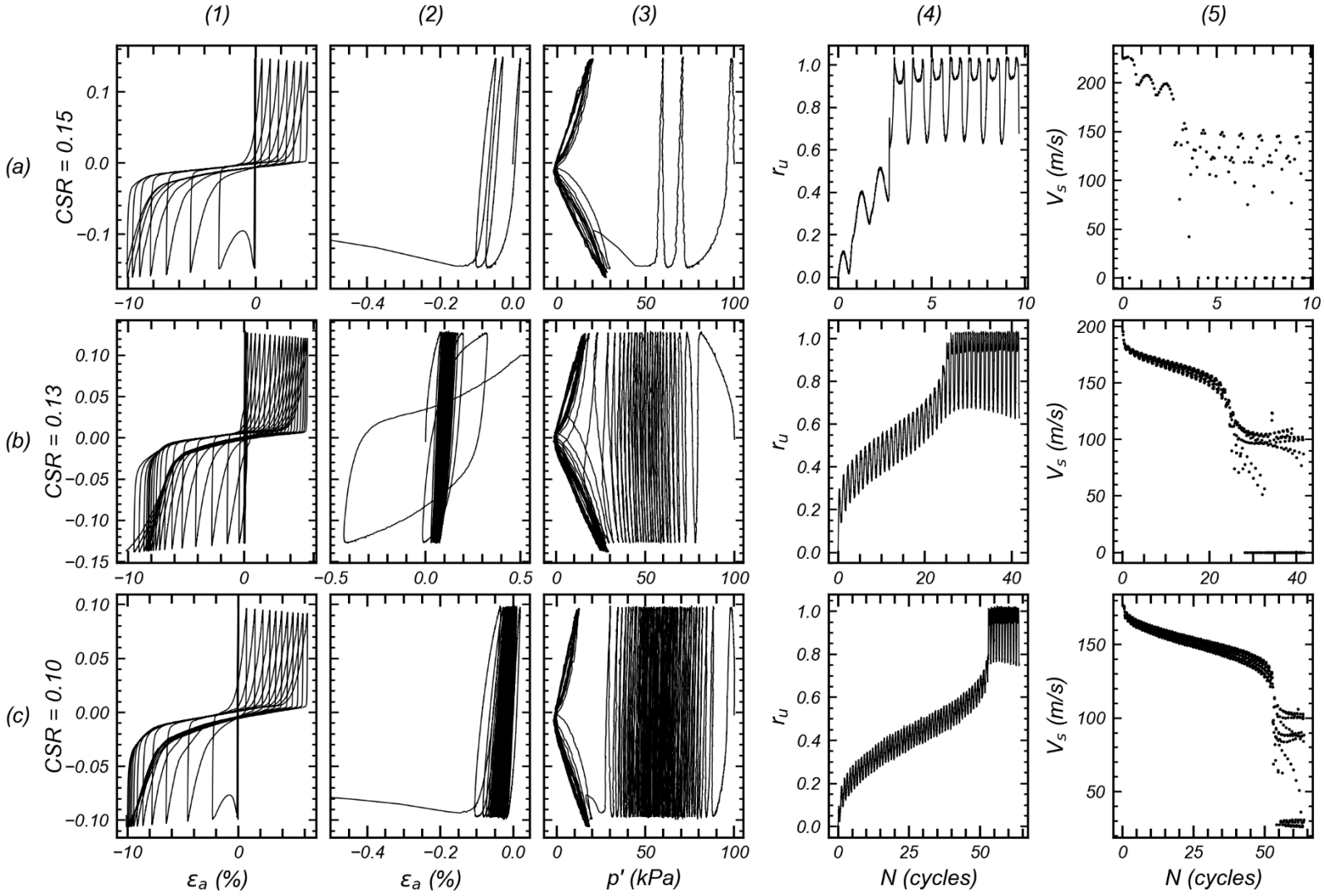

Figure 19. Uncemented dense 100S.

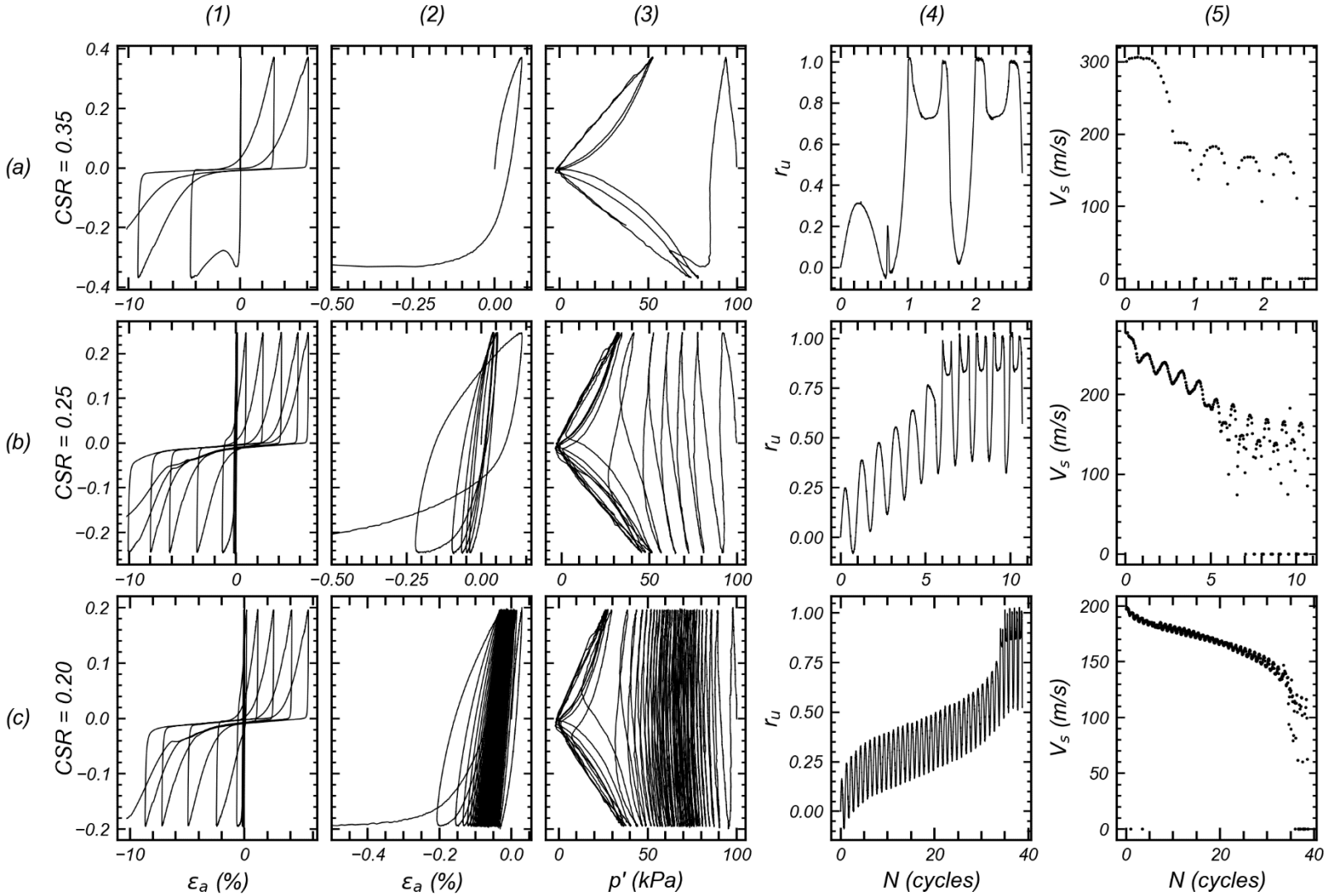

Figure 20. Loose lightly cemented 100S.

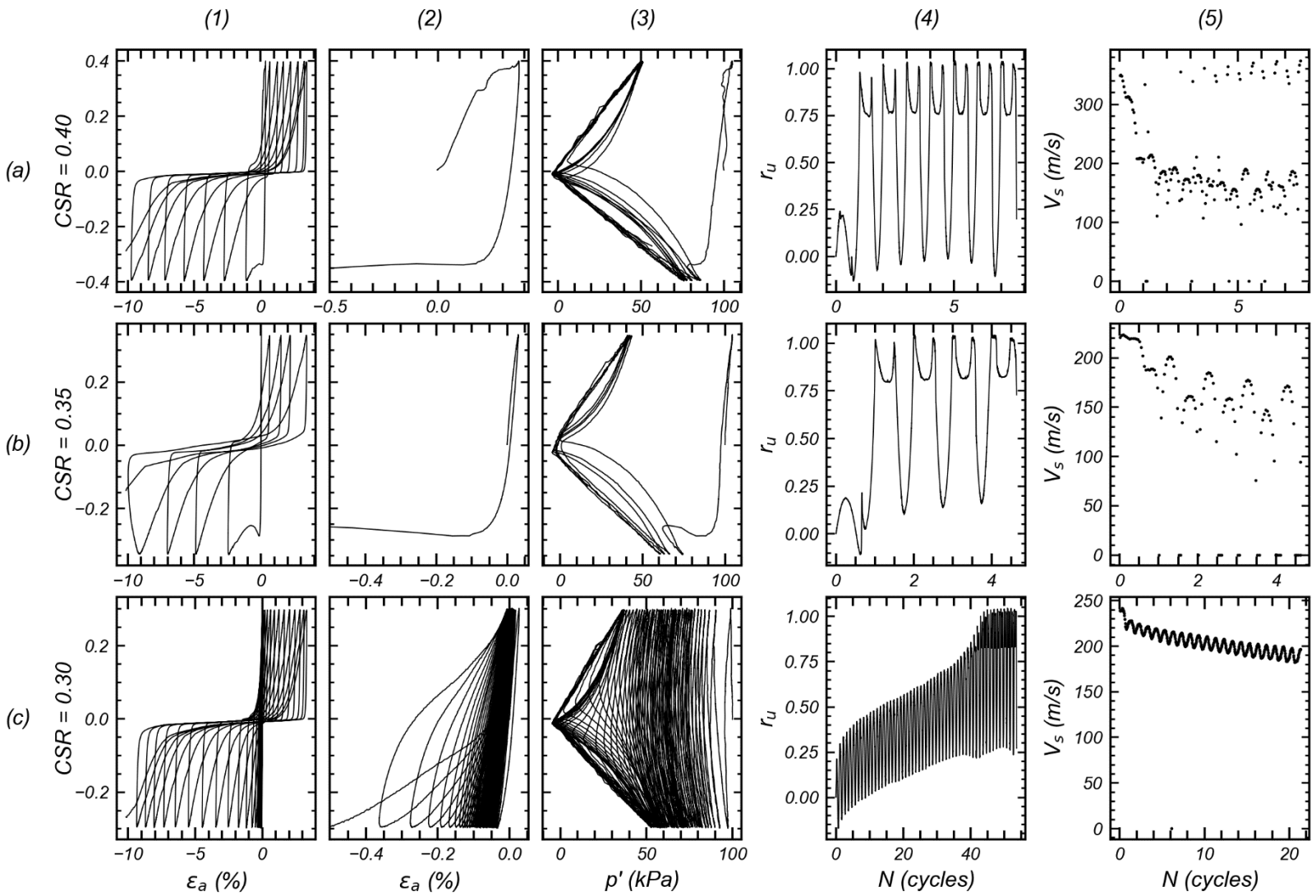

Figure 21. Dense lightly cemented 100S.

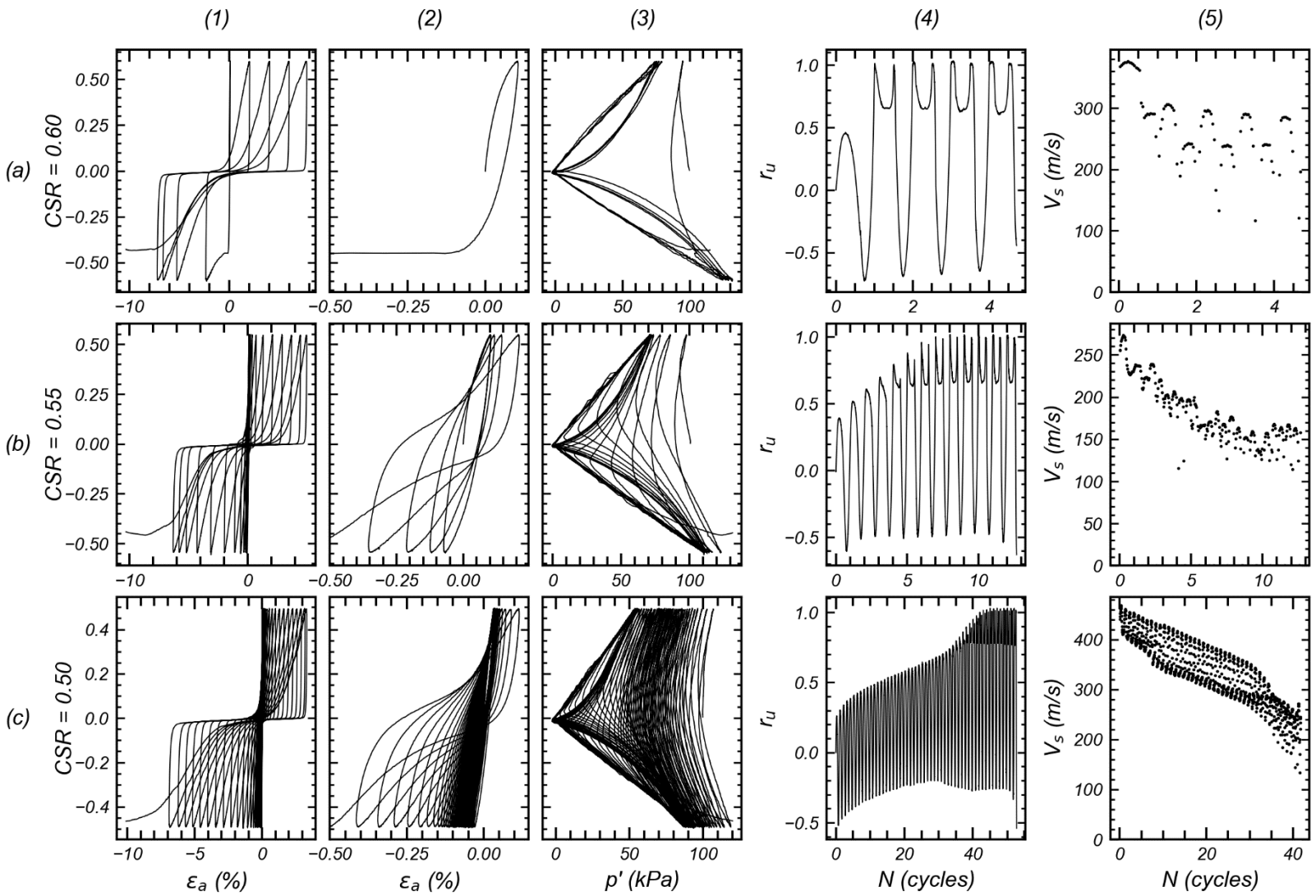

Figure 22. Loose 100S Moderately Cemented.

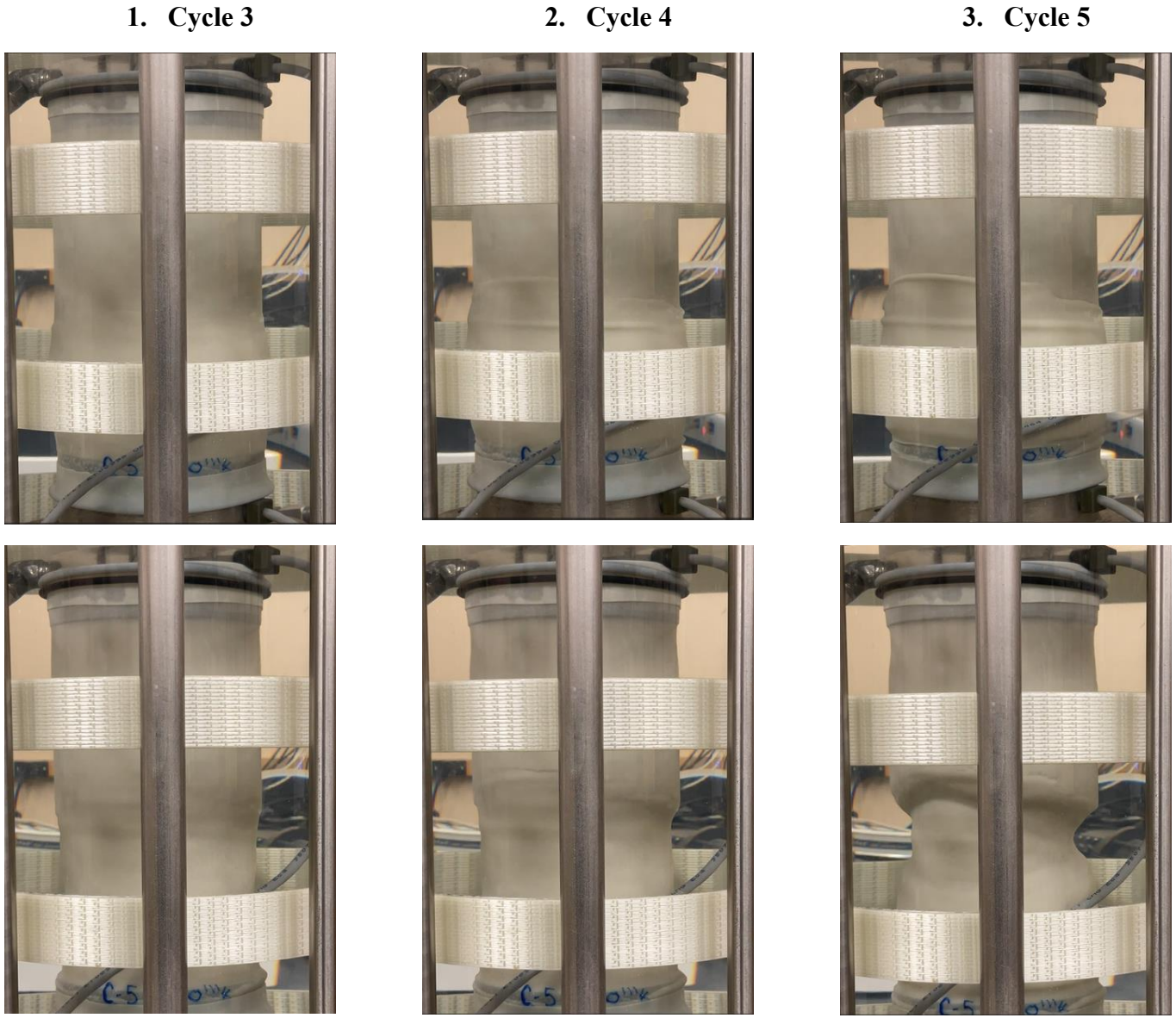

Figure 23. Photos of progressive failure.

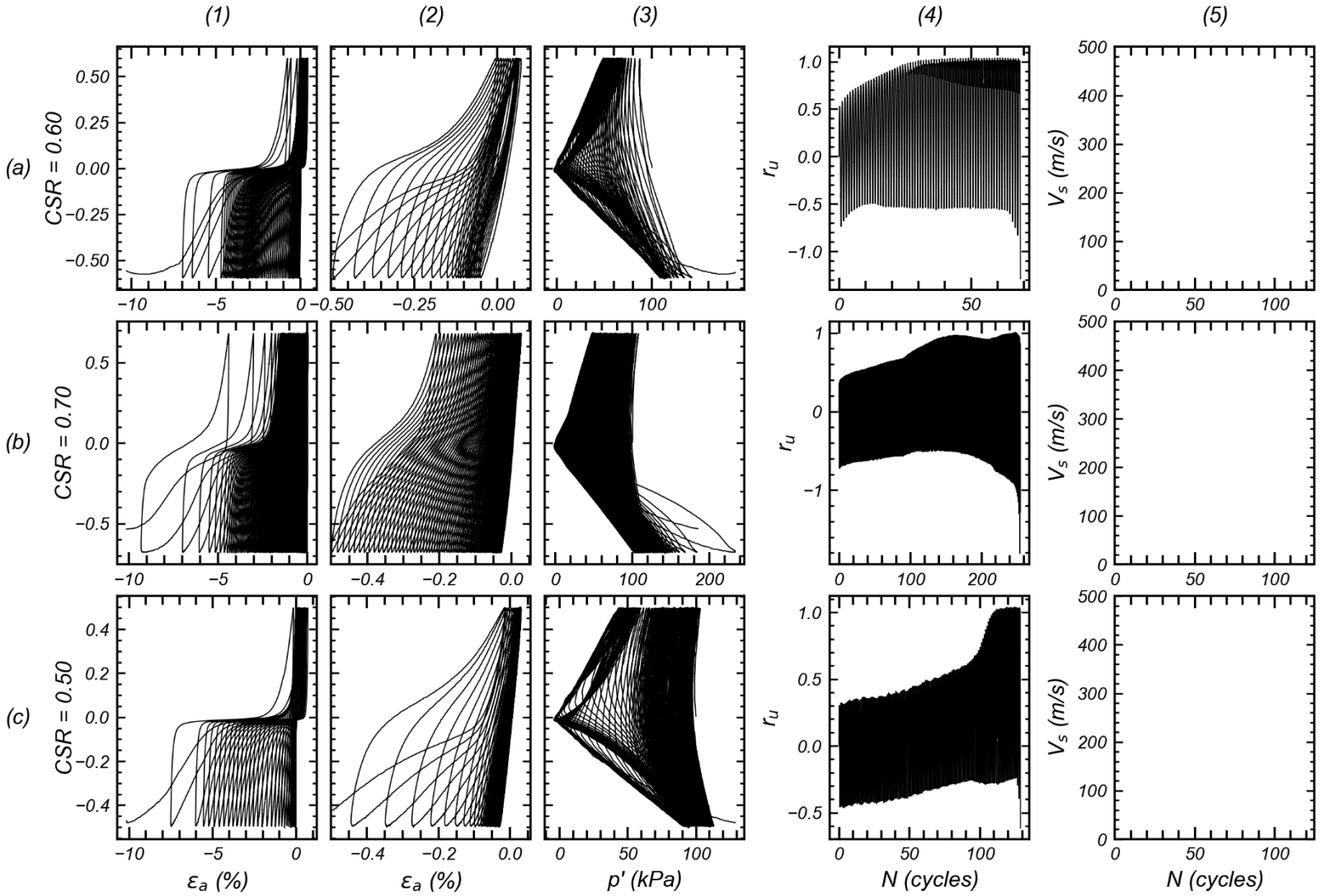

Figure 24. 100S moderately cemented dense. The Vs during shearing are not available for these tests.

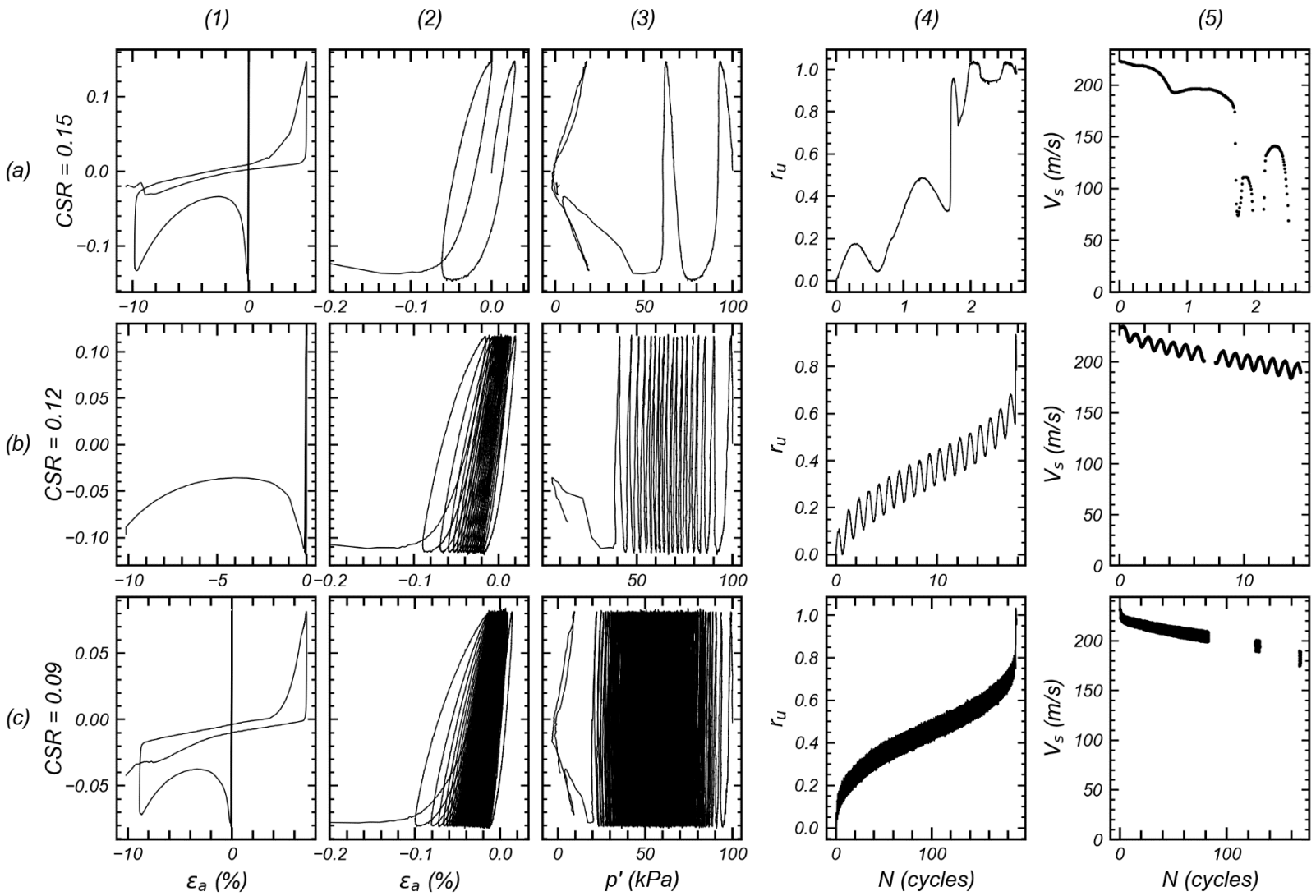

Figure 25. Loose uncemented 70S30C.

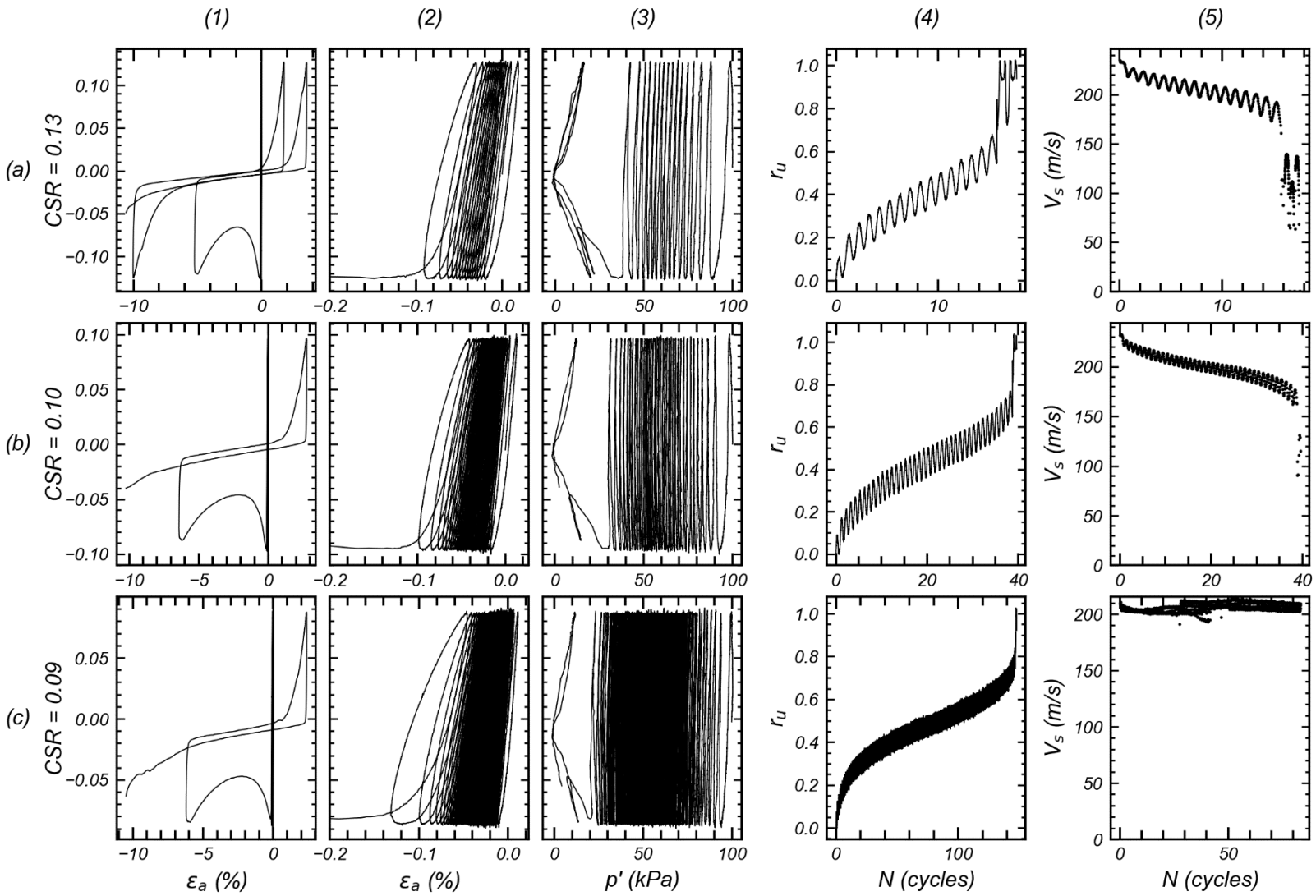

Figure 26. Dense uncemented 70S30C.

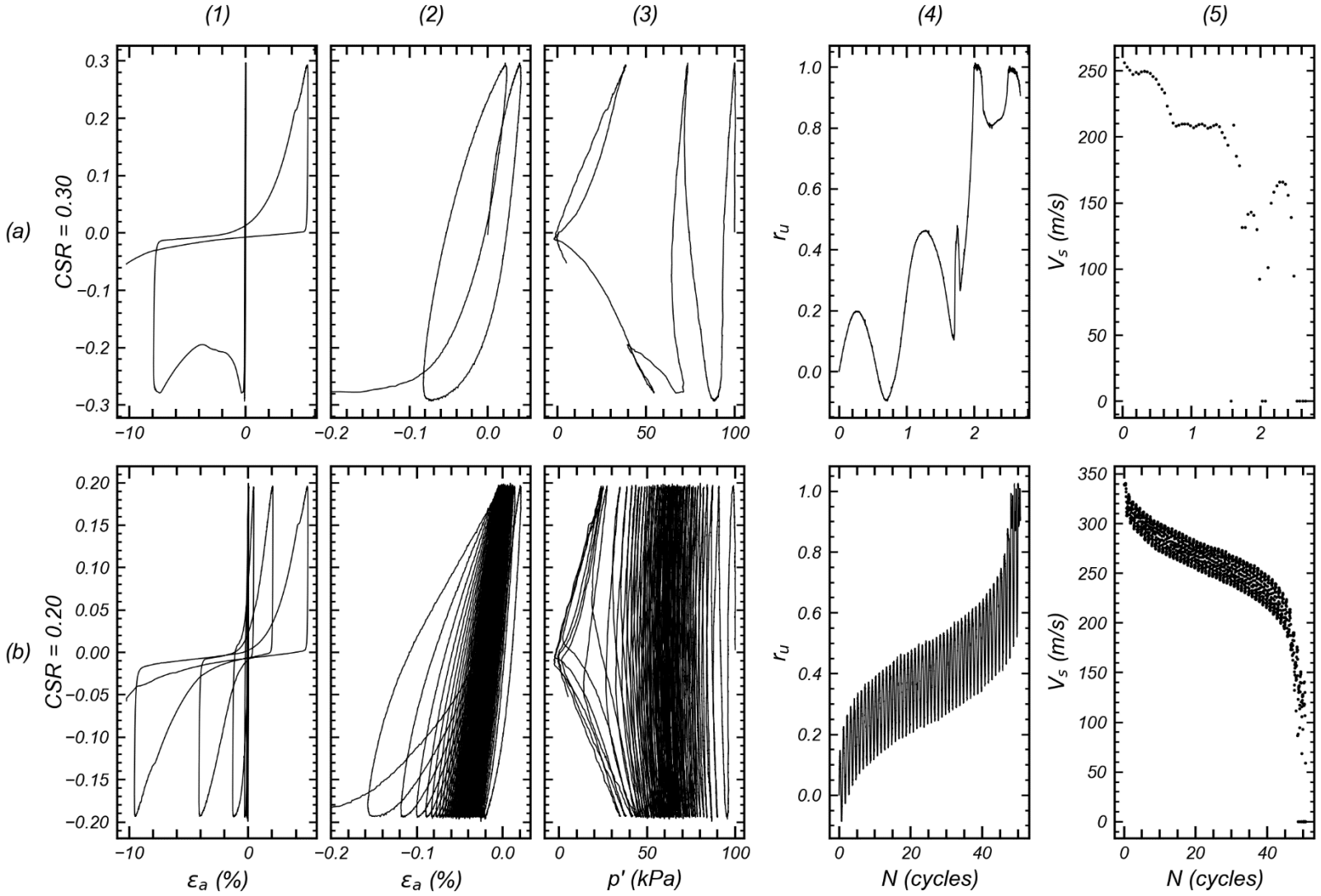

Figure 27. Lightly cemented 70S30C.

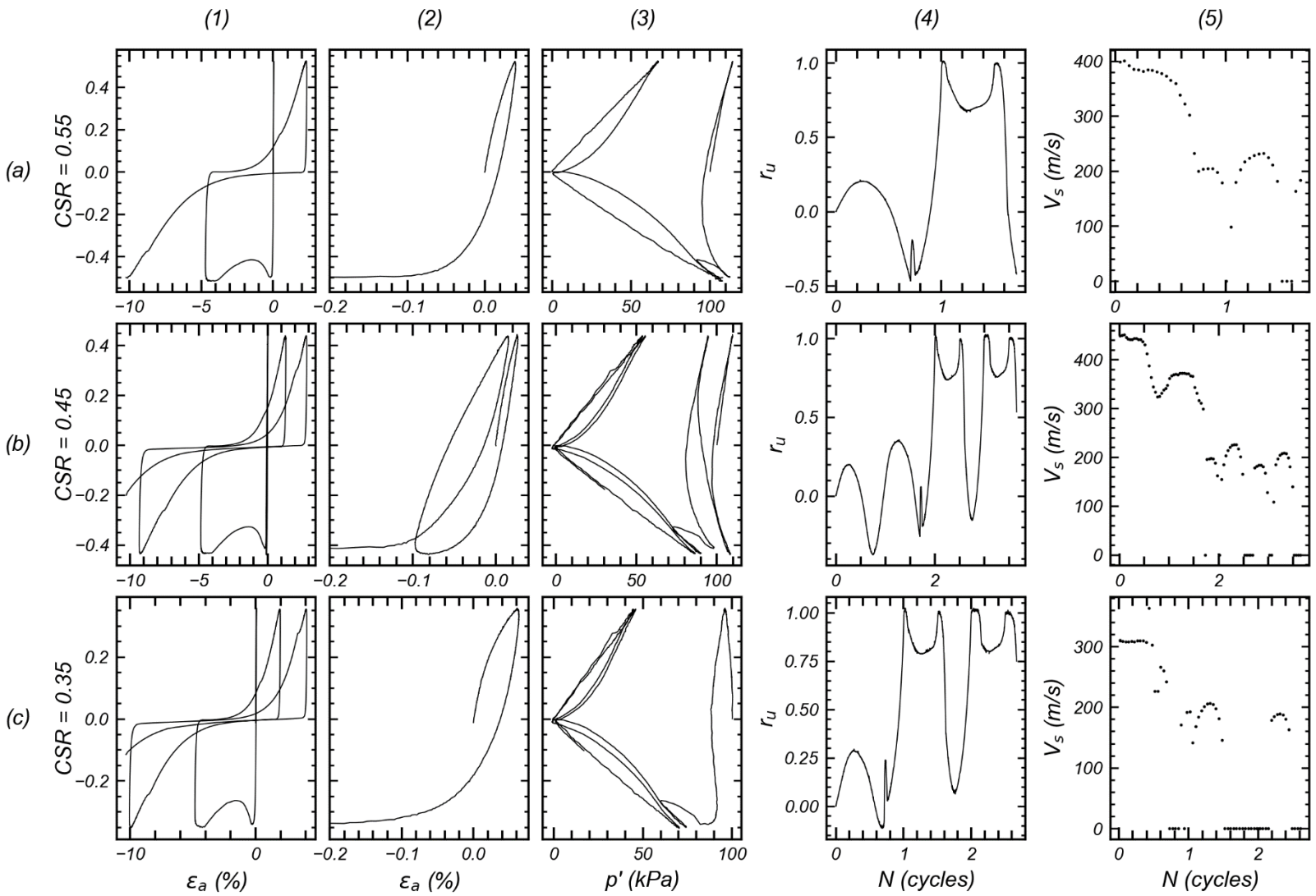

Figure 28. Moderately cemented 70S30C.

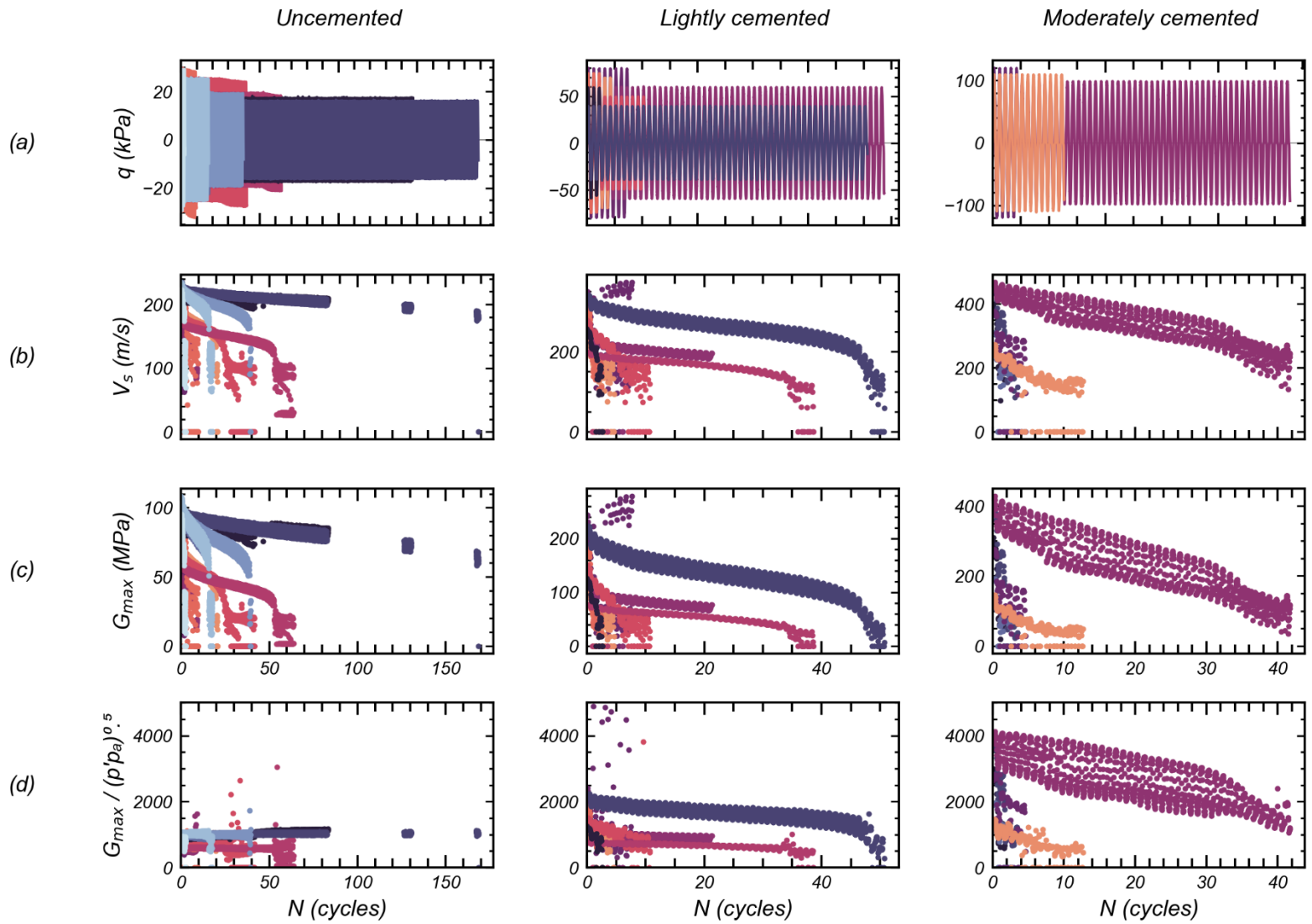

Figure 29. Overall cyclic trends of V_s and G_{max} for uncemented, lightly cemented, and moderately cemented specimens. The soil type is represented with cool colors for 70S30C and warm colors for 100S specimens.

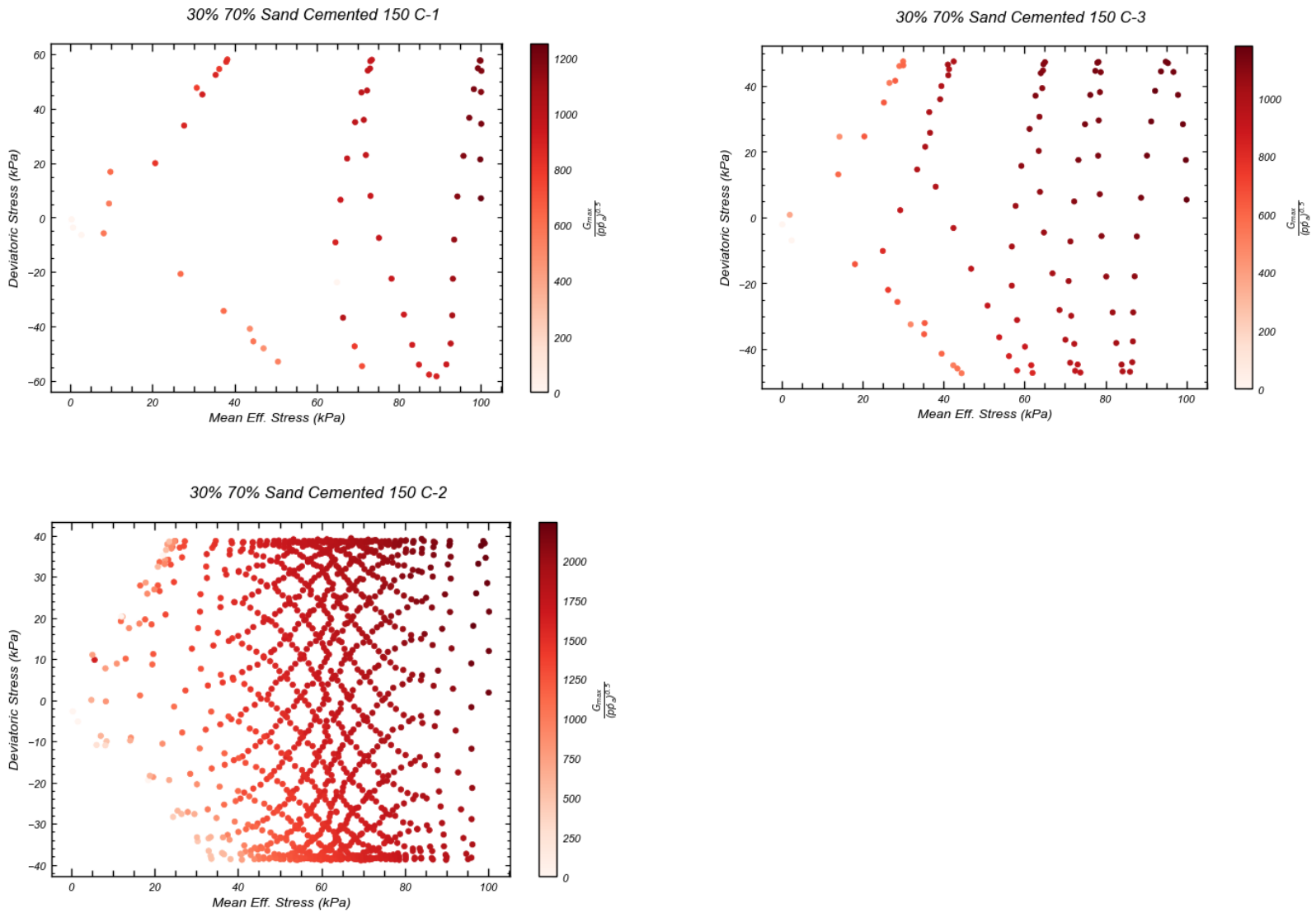

Figure 30. Deviatoric stress versus mean effective stress with color mapping of normalized G_{max}.

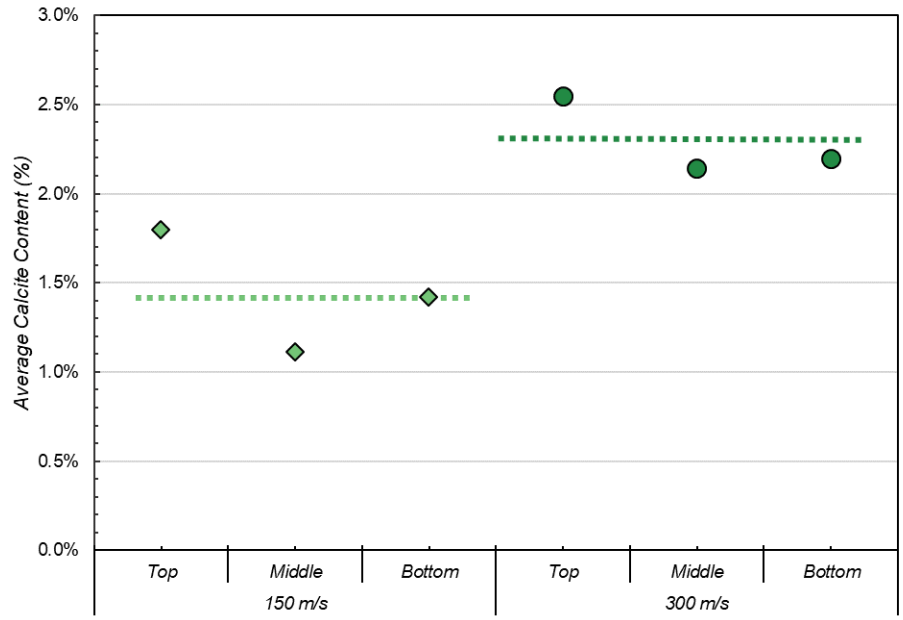

Figure 31. Average calcite content by spatial variability.

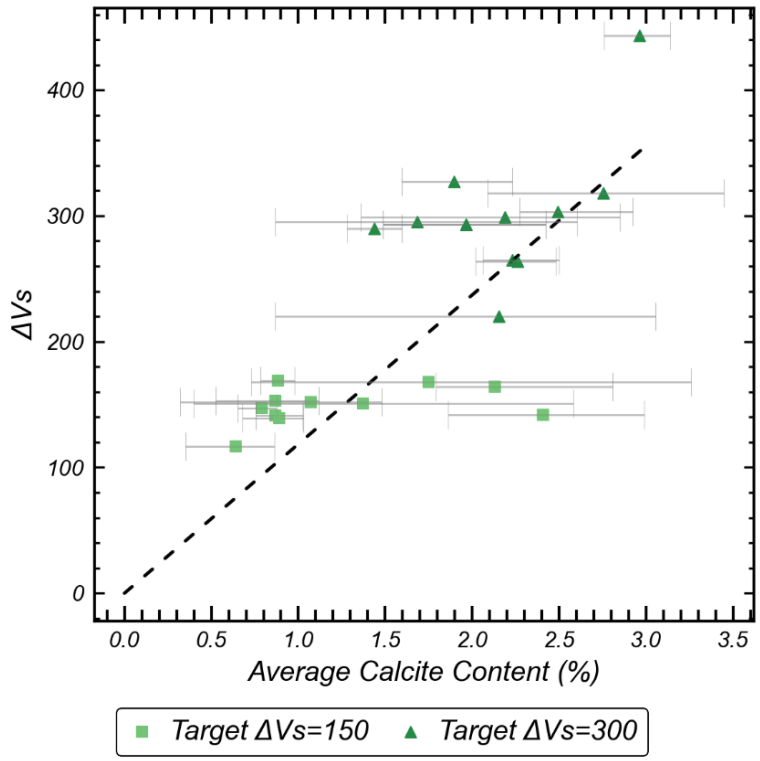

Figure 32. Shear wave velocity versus calcite content for each specimen. Grey error bars indicating minimum and maximum variability. Dashed line shows 1% calcite to 100 m/s shear wave velocity (not a linear regression from data).

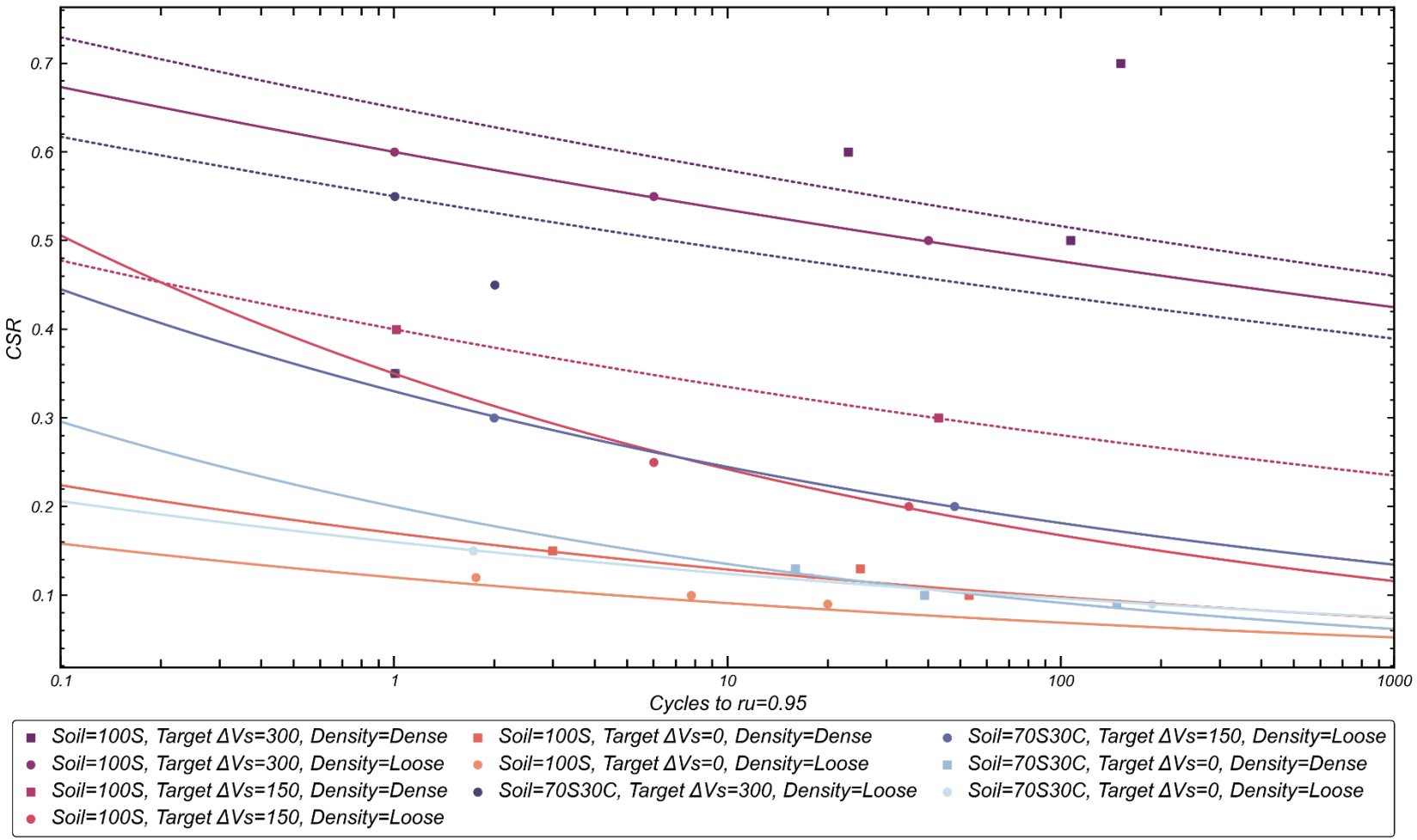

Figure 33. Cycles to r_u of 0.95

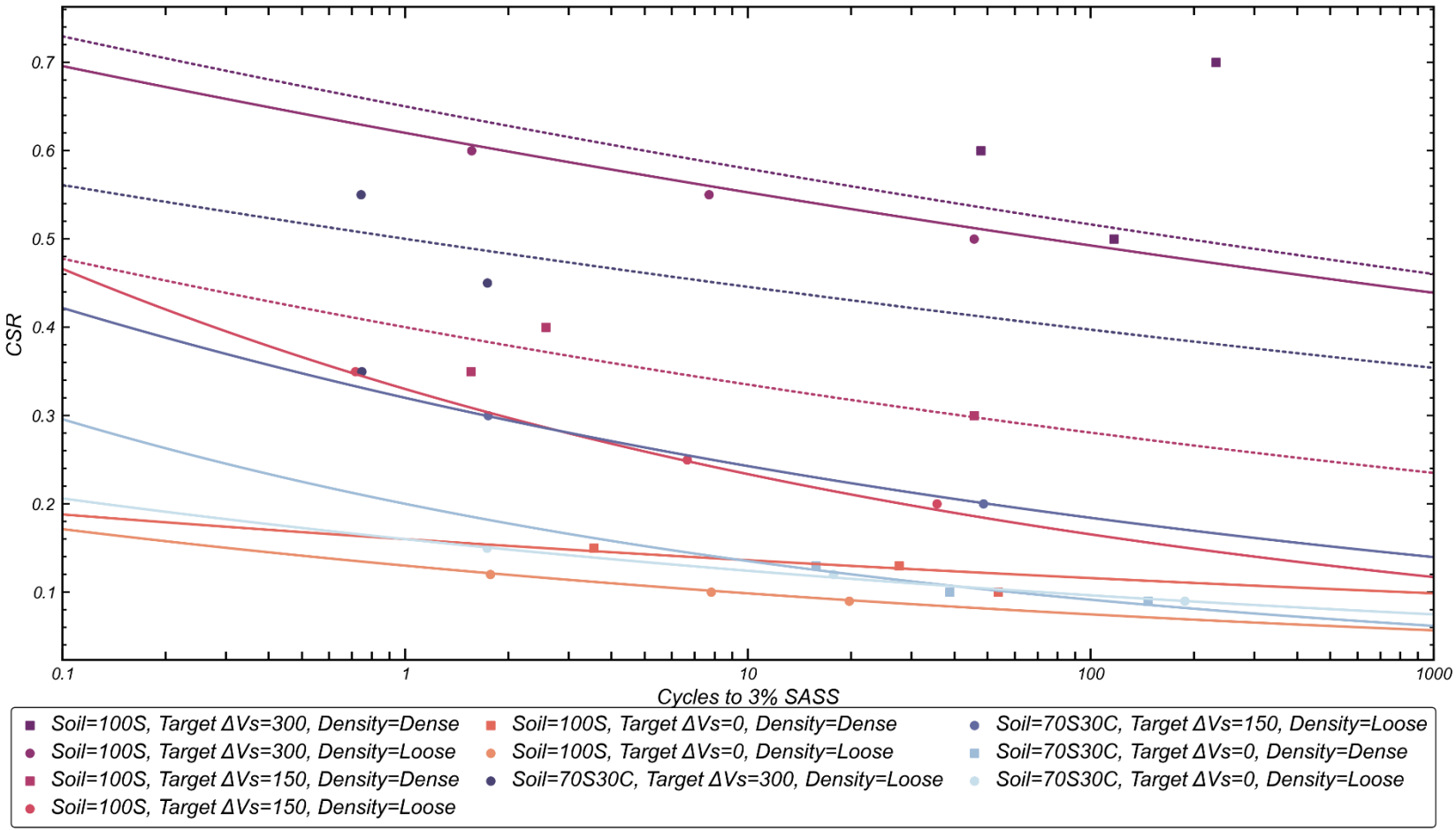

Figure 34. Cycles to 3% strain

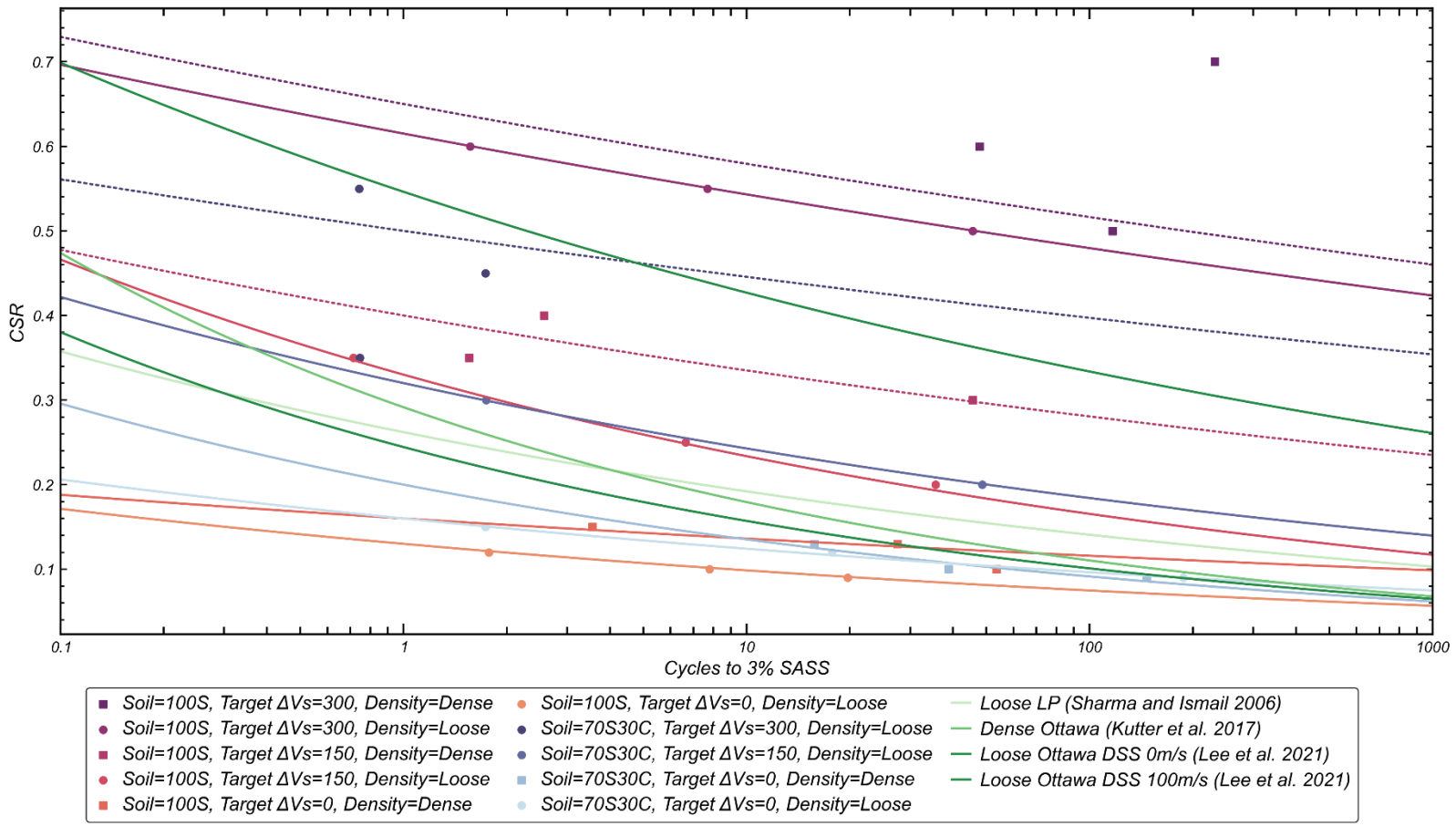

Figure 35. Cycles to 3% strain (DSS data converted to TX equivalent values using Eq. 13)

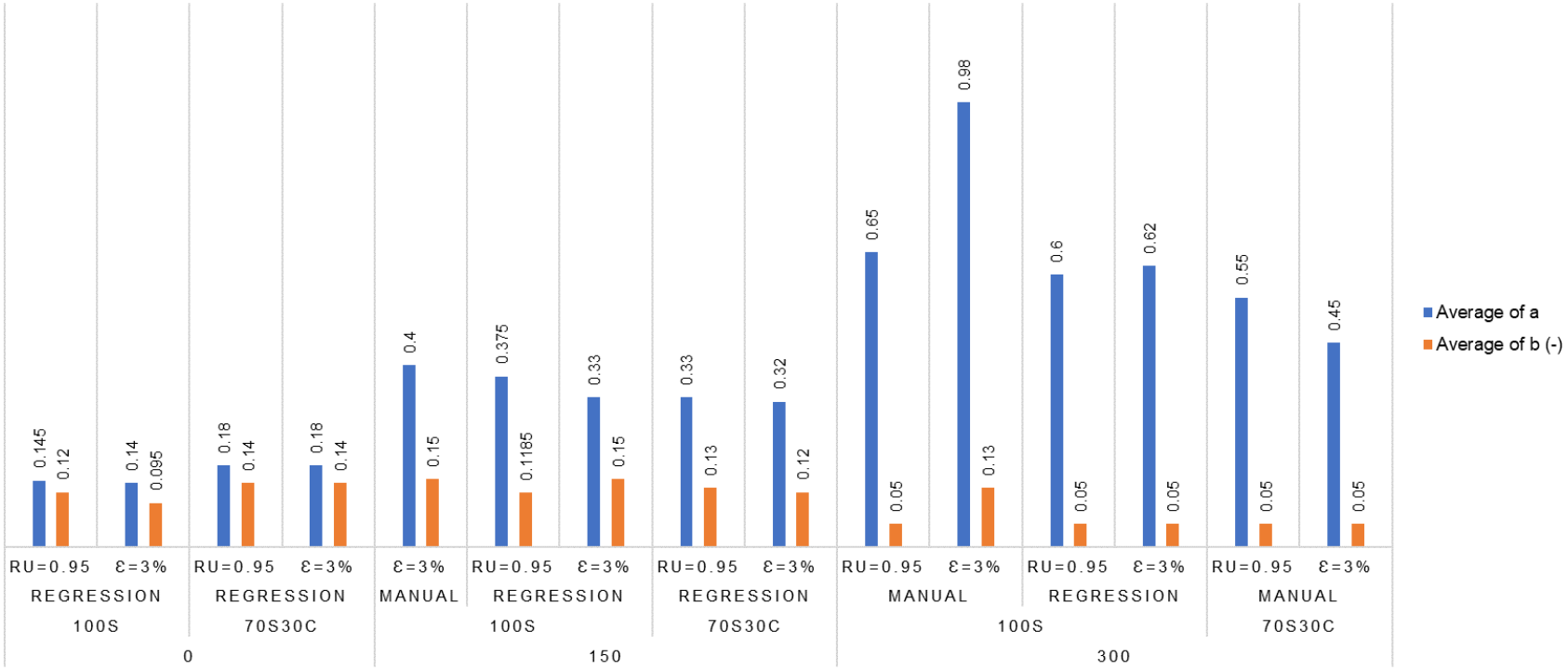

Figure 36. CSR curve fitting parameters.

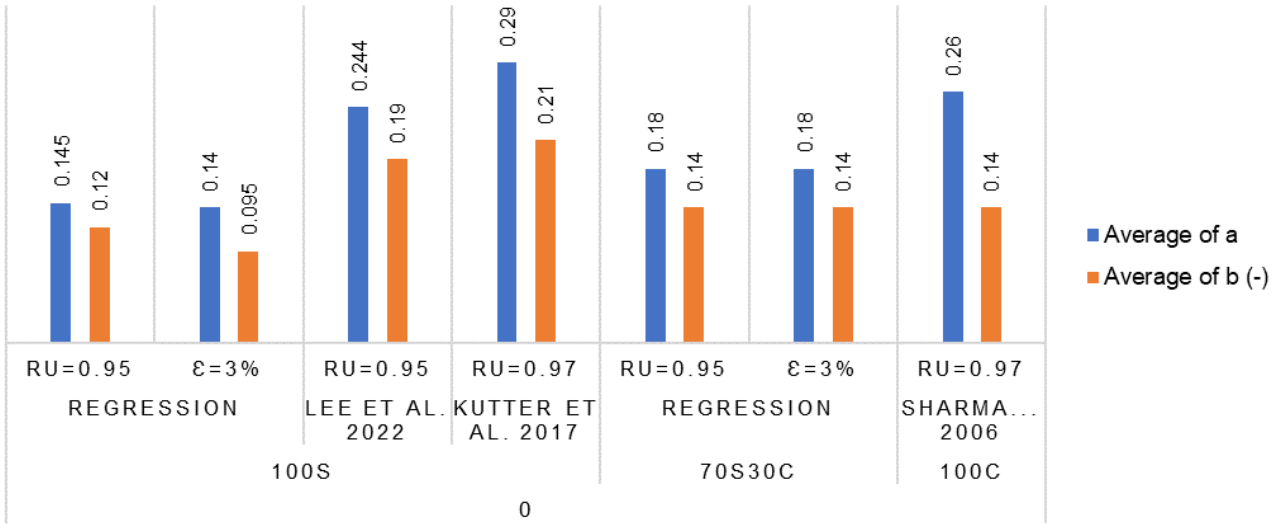

Figure 37. Uncemented comparison to literature

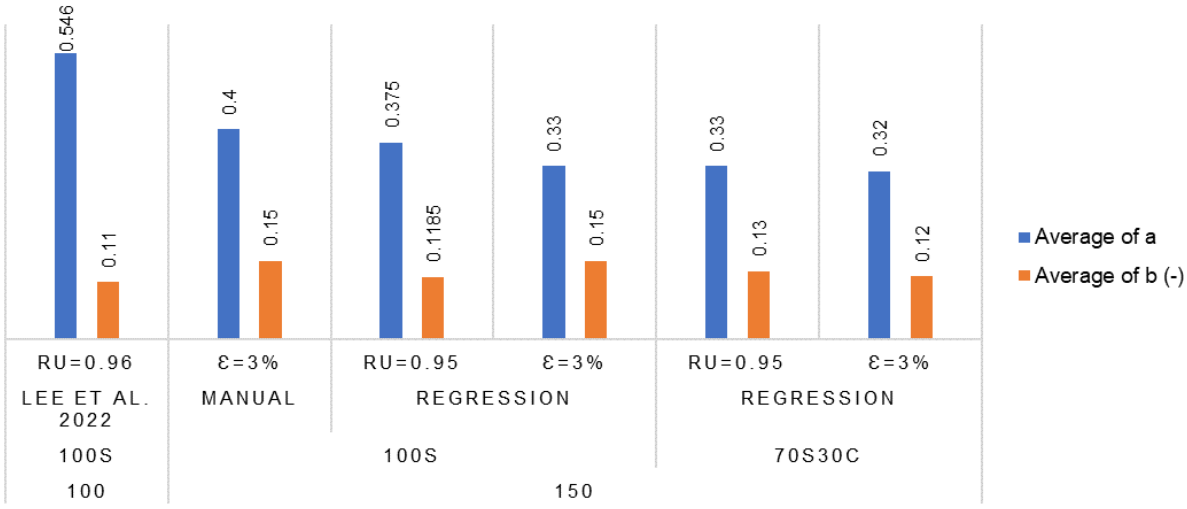

Figure 38. Lightly cemented comparison to literature

APPENDIX A – SAMPLE PREPARATION AND EXECUTION

General Notes

- Fill pumps
    - Cell Pump should be full (since volume is added to bring the cell up to pressure)
    - Back pressure pump should be 1/2 or ¾ full (to allow the sample to consolidate or dilate).
- Purge and attach pump hoses

Purging Pumps

- To purge the pump, tilt the pump up and open the larger connection port. Set pressure to flow water out. If a hose is attached, you can view the bubbles escaping up the hose.

Connecting Hoses

- To make sure no air is trapped when attaching hoses.
- Turn the pump to a target pressure of 5kPa and let a little come out as you attach the hose.
- Hand tighten and add 1/8th turn with a wrench (not more)

Purging Base Pedestal

- To purge the base let water flow from the base port on one side to the base port on the other side.
- Open valve in pore pressure transducer block to purge PPT.

- Zeroing
    - Any pump sensors (pressure/volume) can only be zeroed on the pump
    - All other sensors can be zeroed on the computer

Updating Software

Note: This procedure is developed from the GDS Lab Manual, Video, and experience. It has not worked yet without intervention from GDS support but seems to be most probable to work in the future.

1. Update Computer
    a. You may have to log out and log into an admin account to perform the update.
    b. Then log out and back into the user account.
2. Uninstall the current GDS Lab software.
    a. This will need an admin login to be entered
3. Go into C: and erase the GDS Lab Folder.
4. Unplug the purple dongle USB & USB to the main hardware plug
    a. This is a crucial step!
5. Install new software
    a. This can be retrieved from GDS Lab website
    b. This will need admin login to be entered

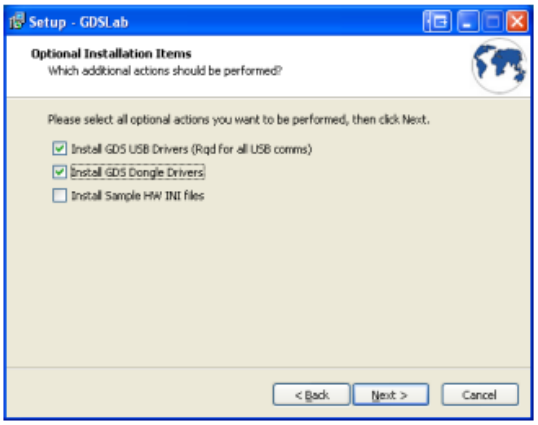

5) It is recommended the following Optional Installation Items are always selected during GDSLab set-up:
   - ☑ GDS USB Drivers
   - ☑ GDS Dongle Drivers

Following this final selection choice **Next** should be clicked, initiating the installation of GDSLab.

6. When the FTDI CDM Driver window pops up
   a. Select extract and then install
7. Go into USB drive and copy .ini file into new C: GDS Lab folder
8. Go back to USB drive and run file called "DeployToPlugins.bat"
   a. This will need admin login to be entered
9. Reconnect purple dongle and hardware USBs
10. Open GDS Lab and create new station
    a. As described in "Running a test" section of GDSLab Manual

Sample Preparation

Wet Preparation

- Purge base
  - Attach hose to specimen base and pump water up onto the base. Allow water to purge down through other baseline as well.
  - Spread the meniscus all around the base with your finger as needed.
- Add porous stone
  - Slide porous stone over the base from the side and let it settle. Dropping it straight onto the base might catch air bubbles.

Dry Preparation

- Use light compressed air to blow water out of base and top cap lines

For Both Wet and Dry

- Check membrane for holes
  - Hold up to the light and stretch for inspection
- Put membrane on base
  - Lubricate around the base where membrane will sit
  - Stretch membrane over the base
  - Slip 1 O-ring onto the base and slide down to remove air bubbles.
    - This uses the assistance of O-ring stretcher
  - Add a second O-ring and space a little above the first to hold the membrane in place.


- Put form over membrane
    - Add two O-rings to the top of the form
- Wrap membrane over the top of the form
- Apply vacuum to membrane
    - 10-20 kPa should be sufficient
    - If the membrane is not completely up against the form, start over.



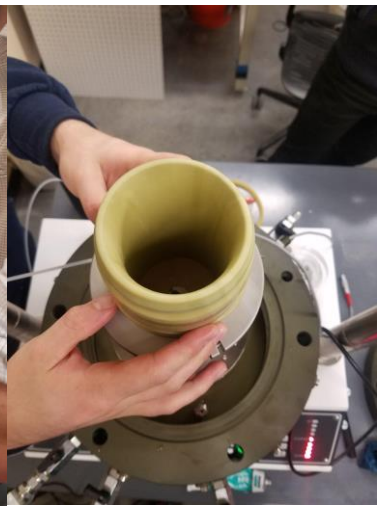

- Add soil sample – The following will not go into great depth on air pluviation. Reach out for more details.

Pluviation


    - Make sure it is flush with the top of the form
- Add porous stone to the top of sample
- Top cap
    - Lubricate sides where membrane will touch
    - Lubricate and place plastic extension sealer thing on top of cap
    - Place cap on top of the porous stone
    - Pull membrane up on cap
    - Slide gaskets up and over membrane


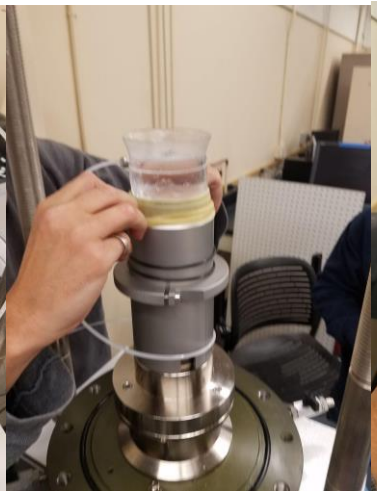


- Tests sample for leaks
    - Add vacuum back pressure to sample

        - This can be done by applying -15 kPa and later consolidating the specimen of ramping the vacuum to the target consolidation confinement.
        - For cemented specimens the vacuum was ramped to -100kPa, effectively consolidating the specimen.
    - If it is holding air, the volume should not change much
        - If a pore pressure transducer is attached: The vacuum valve can be turned off and you can observe if the specimen is losing pressure or not.
    - Leave backpressure on to add stability to the sample
- Remove form
- Measure specimen diameter and height, bring vacuum to more than -20 kPa for measurement
    - Measurements can be done with a PI tape or caliper.
        - It is my opinion that caliper measurements are more consistent.
        - Measurements were recorded at five height increments and two perpendicular orientations. The final diameter was the average of the 12 measurements minus the membrane thickness.

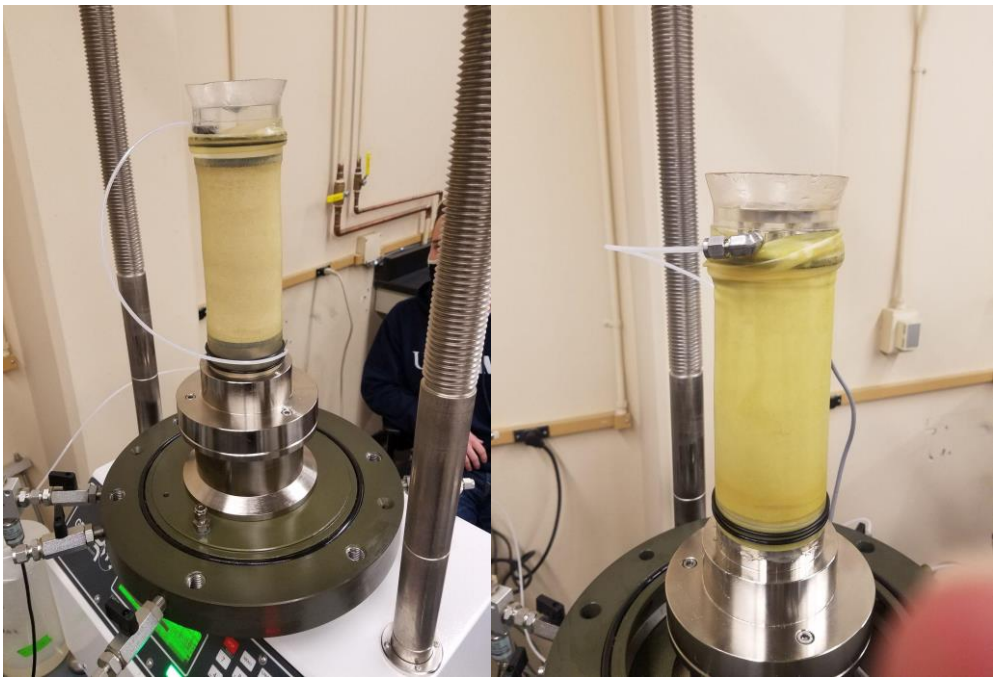

Adding Cell

- Add bird cage (aka the cell)
    - First
        - Lubricate the extension cap where it attaches to the cap and plastic sheath
        - Check that correct load cell and extender piece is in place
        - Place load cell ram in the up and locked position
        - Check seal on frame has gasket and is lubricated

- After
    - Add bolts and tighten enough to compress gasket
    - Set stroke to 60mm of stroke (50 above, 10 below) and zero
        - This can best be visualized by opening the Displacement Frame settings in GDS Lab
        - Could vary based on test type, i.e. extension, cyclic
    - Lower crossbar and attach to ram
        - Make sure cross bar is level
        - Then remove ram lock
        - Add big nuts above cross bar
- Seat extension to cap (GDS Helpsheet 47)
    - Manually raise specimen until cap and extension comes together (approximately 3mm/min). Alternatively lower cross bar.
    - Watch load to increase to approximately <0.01 kN
    - Check if it is seated by adding suction through atmospheric tube
    - Leave atmospheric tube open (I usually close it later before running the tests "optional")
- Add LVDT
    - Place where it will not have compatibility issues
    - 40mm of travel total. Lower till depressed approximately -2mm (extension "no damage to sensor if over extended) + allows 35mm(compression) and set max to 37 which stops LVDT 3mm before completely compressed
        - Zero LVDT displacement on computer

- Fill cell with deionized water
    - Add to bottom
    - Make sure top valve is open for air to escape and close when filled with water

- Increase cell water to 20kPa-50kPa and check if it is holding pressure

Carbon Dioxide saturation

(Based on recommendations from Appendix B.4.1 of Jefferies and Been 2019)

- Release vacuumed pressure on sample
- Attach CO2 to bottom and place tube from top cap into water to monitor flow
- Release CO2 at approximately 1-5 bubble per second rate
- Let bubble for 1-2 hours
- Add water to sample (Fresh DI and de-aired water)
  - Pump water from the bottom up through the sample using 5kPa pressure target
  - Let flow through the sample for approximately 2-3 pore volumes or whatever desired

Final Checklist

Inspect **top to bottom** before allowing computer control to avoid damage to equipment.

- ✓ Big nuts are on cross bar
- ✓ Ram lock and support rod are removed
- ✓ LVDT is in a good place that will allow it to not collide with anything and has appropriate travel
- ✓ If extension or cyclic test: Displacement does not allow for load cell to hit top of cell
- ✓ Cell has bolts and are tightened
- ✓ All pieces along ram look tight
- ✓ Base piston is appropriately placed
- ✓ Pore pump is attached to top cap
- ✓ All valves on cell are in appropriate positions and nothing is leaking

GDS Lab

Computer Setup

- Click Data save
    - Click Single directory
    - Time Format linear or custom
    - Check box to save calculated data
    - Type: Triaxial
    - Docked means the load cell is in contact with the top cap: select yes
- Click Sample
    - At minimum, add sample height and diameter

Dry Samples

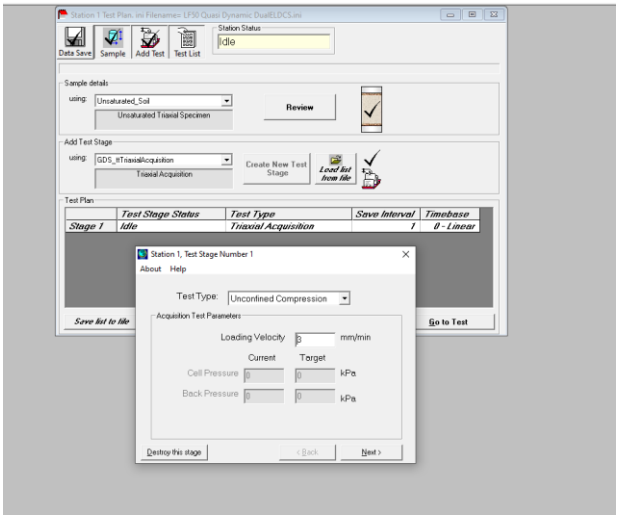

Saturated Samples

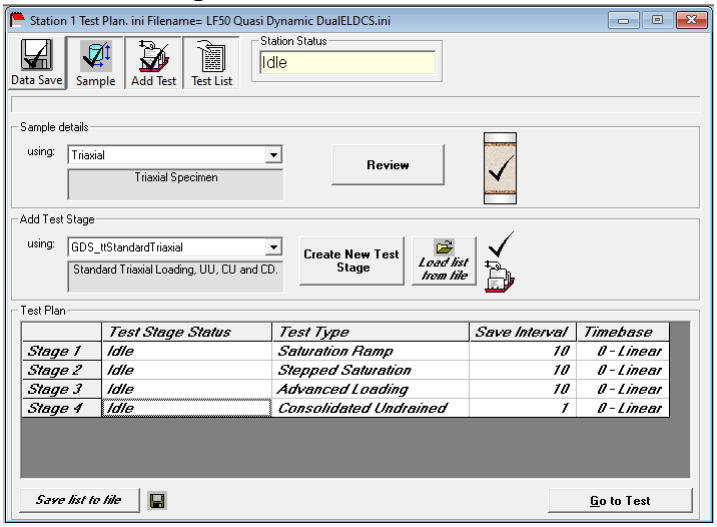

General triaxial modules

- Note that the save interval can be different for different modules to reduce data

Saturation

- Ramp pressure to 100kPa below the believed saturation point
    - Slow enough to not disturb sample
- Make sure effective pressure prior to ramp is above 50kPa so minor axial stresses cannot shear the specimen. In this example, the cell pressure starts at 50 to give the sample aproximately 43kPa effective stress.
- Select preferred axial control: deviatoric, load cell or no control
- For A100 at Dr=40% Saturared at Cell pressure = 550kPa so ramp to 450kPa before stepping
- Note: It is best to end test after ramp and automatically go into autosaturate phase
- To calculate the estimated B-value measure the Vs and estimate the value utilizing Black and Lee (1973)

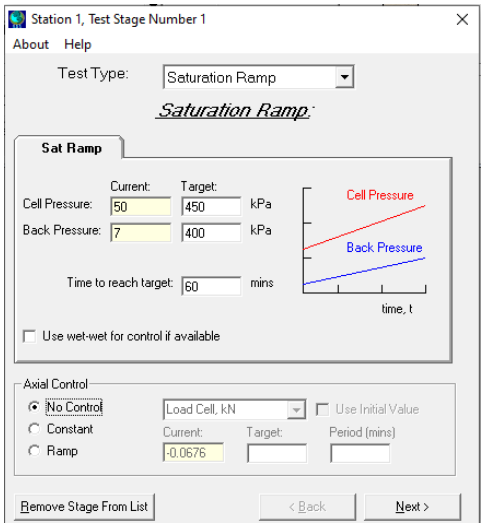

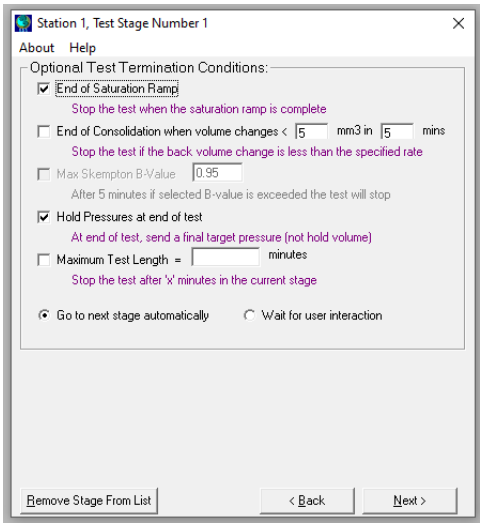

- Use automatic saturation
    - Cell pressure increments of 30kPa
    - Effective stress between increments to 50kPa
    - Set deviatoric Stress to stay constant at 0 kPa or no control

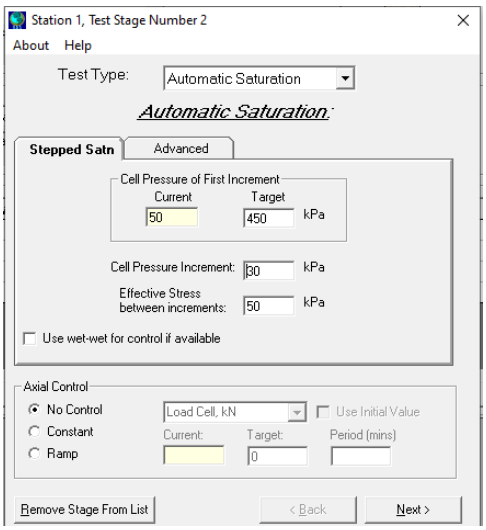
Station 1, Test Stage Number 2
About Help
Test Type: Automatic Saturation
Automatic Saturation:
Stepped Satn Advanced
Cell Pressure of First Increment
Current Target
50 450 kPa
Cell Pressure Increment: 30 kPa
Effective Stress between increments: 50 kPa
Use wet-wet for control if available
Axial Control
No Control Load Cell, kN Use Initial Value
Constant Current: Target: Period (mins)
Ramp 0
Remove Stage From List < Back Next >

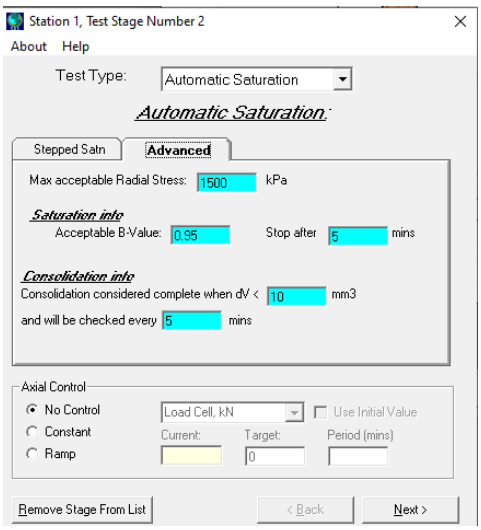
Station 1, Test Stage Number 2
About Help
Test Type: Automatic Saturation
Automatic Saturation:
Stepped Satn Advanced
Max acceptable Radial Stress: 1500 kPa
Saturation info
Acceptable B-Value: 0.95 Stop after 5 mins
Consolidation info
Consolidation considered complete when dV < 10 mm3
and will be checked every 5 mins
Axial Control
No Control Load Cell, kN Use Initial Value
Constant Current: Target: Period (mins)
Ramp 0
Remove Stage From List < Back Next >

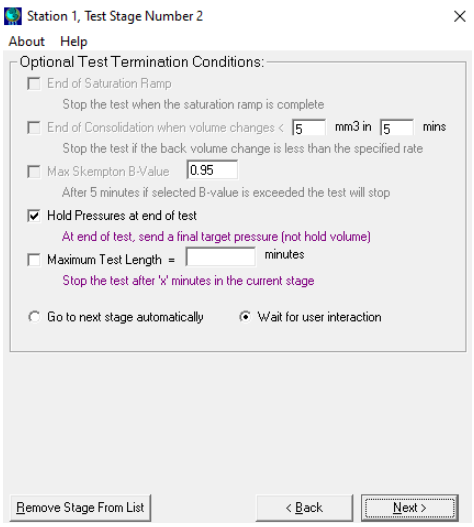
Station 1, Test Stage Number 2
About Help
Optional Test Termination Conditions:
End of Saturation Ramp
Stop the test when the saturation ramp is complete
End of Consolidation when volume changes < 5 mm3 in 5 mins
Stop the test if the back volume change is less than the specified rate
Max Skempton B-Value 0.95
After 5 minutes if selected B-value is exceeded the test will stop
Hold Pressures at end of test
At end of test, send a final target pressure (not hold volume)
Maximum Test Length = minutes
Stop the test after 'x' minutes in the current stage
Go to next stage automatically Wait for user interaction
Remove Stage From List < Back Next >

Consolidation

- Set up consolidation phase

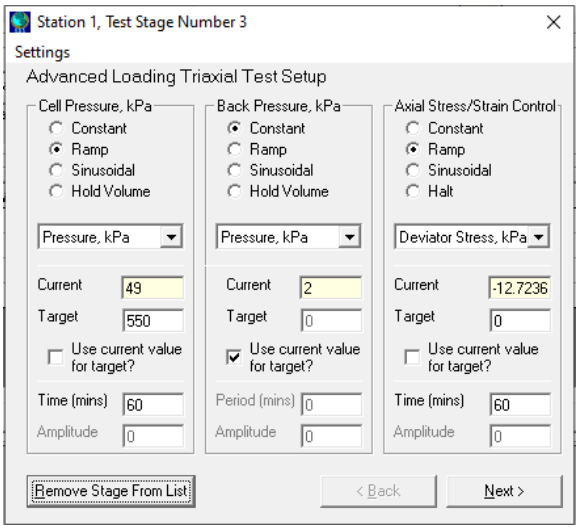

Shearing

- Use one of the triaxial shearing modules to perform UU, CD, CU
- While shearing, make sure sample is not moving horizontal in a way that could torque on the cap

<u>Consolidated Drained</u>

- Shear rate for 100A – 0.125 mm/min (20% in 4 hours)

<u>Consolidated Undrained</u>

- Shear Rate for 100A – 0.25 mm/min (20% in 2 hours)
- Close valve to sample to eliminate systematic response outside of cell

Cleanup

- Save test procedure to test folder
- Ran Advanced loading to bring all the pressures back to zero
- Start draining cell
- Remove LVDT
- Remove cross bar
- Remove cell

APPENDIX B – TREATMENT PROTOCAL

This treatment protocol was developed with information used at University of California Davis and the University of Washington. Bits and pieces were taken from both procedures to build the most robust treatment for triaxial specimens.

Growing Bacteria

Mother Culture

- *Sporosarcina pasteurii* (*S. pasteurii*, ATCC 11859) was stored in vial form in -80°C freezer
- These can be made from pellets and used to restart future culture if it dies or becomes contaminated
- To start a culture, use a sterile scraper and sterile technique to move some culture from the vial to petri dish with agar growth medium
- Frozen pellets should not be frequently used to make more pellets for freezing as too many cycles of regrowing culture increases the chance of contamination

Growth Medium (1 L batch)

- Add all ingredients into separate flasks
    - Tris + ~250ml water to Erlenmeyer flask
    - Ammonium + ~250ml water to Erlenmeyer flask
    - Yeast + rest of ~500ml water to liter flask or autoclavable vessel of choice
- Recipes available upon request
- Autoclave all ingredients separately
    - 25-30 minutes on liquid mode
- Mix together in a L bottle
    - Make sure they have cooled first so it does not volatilize

Inoculate Growth Medium

- Agar petri dishes contain a modified agar designed to support *S. Pasteurii*
- Using a Bunsen burner and scraper, use a sterile technique to move bacteria from the petri dish to the growth medium
- Incubate agar plate at 28°C for 24-36 hours before storing at 4°C

Pellet Method

- The process involves inoculating a flask of growth medium as seen above
- The bacteria is allowed to multiply for 36 hours in a 28°C water bather with circular agitation
- Autoclave at least 500 mL of isotonic saline solution (9 g/L NaCl in deionized water)
- Transfer 50 mL of cell mixture into one 50 mL falcon tube for each pellet you wish to create (each concentrated cell pellet will be about 10 mL at completion)
    - Spin in a centrifuge at a max speed of 3300-3600 RPM, at 10°C for 30 minutes
        - If it can be spun faster, the time can be reduced

    - One 4ml sample of bacteria can be frozen for later analysis
- Remove tubes and pour off the "clear" supernatant while keeping the pelleted cells in the tube
- Add 40 mL of autoclaved isotonic saline solution and mix well, making sure to dislodge cells at bottom of the tube
- Centrifuge this mixture again for 15 minutes
- Examine the supernatant
    - If acceptably colorless (stronger tints of orange indicate that some yeast extract remains and has not been fully removed), pour off supernatant and proceed to next step
    - If cells need more rinsing, repeat above steps again until clear
- As the final step, create a pellet by adding 10 mL of isotonic saline solution to cells and mix well.
- Measure and record OD_{600} of pellet, as well as the OD_{600} of the pellet diluted 100-fold. On the tube, mark the date, type of cell, and OD_{600}.
- Store in the refrigerator (NOT THE FREEZER) and use within 4 days.

Augmentation and Cementation

Before Augmentation

- Prepare a solution of ammonium chloride, yeast, and 1 pellet
    - The chemical amounts are specified in the *Recipe* attachment
    - During the preparation process, leave some of the water to the side for rinsing chemicals out of the weighing dish

Sample Preparation

- Air Pluviation to achieve target relative density
- After placing the top cap on the sample, apply a vacuum of -85kPa to stabilize the specimen
- Add the triaxial cell around the specimen and gradually replace the vacuum with a cell water pressure of 100 kPa
    - There is a discrepancy between the 85kPa and 100kPa where volume change of the sample is not captured
    - 100 kPa will not only be more stable but also mimic the confinement applied in other studies
- Pump DI water through the specimen at 20 ml/minute

Bromide Tracer Test

- Perform a bromide tracer test before inoculating. This will help us know the pore volume and chemical transport properties (recommended by Mike Gomez).
- Perform at least once to ensure proper treatment volume
- Follow instructions in the *Bromide Passive Tracer Protocol updated document*

Augmentation

- Measure shear wave velocity
- Inject a total of ~4 PV injection solution (8PV 250mL for the 30mL pore volume DSS).
    - Assuming a PV is 250mL
    - For all flow rates, use 20ml/min
        1. We want the maximum flow rate to distribute treatment throughout the sample evenly
    - Collect a 7mL sample of injection fluid
    - The five phase augmentation injection method used by Lee et al. (2021) and Gomez et al. (2019)
        1. 1 PV (pore volumes) is injected from bottom to top
            - All effluent is discarded since it contains the initial pore fluid
            - One 7mL sample is collected
        2. 1 PV (pore volumes) is injected from bottom to top
            - All effluent is collected
        3. 2 PV is injected from top to bottom
            - All effluent is collected

           Mix all the effluent into this injection solution
        4. 1 PV is injected from bottom to top
            - All effluent is collected and mixed back with the remaining injection fluid
        5. 1 PV is injected from top to bottom.
            - All effluent is collected
            - One 7mL sample is collected then the effluent can be discarded.
- Measure shear wave velocity
- Wait for more than 1 hour
    - Allow for cells to attach to soil
- OD_{600} is then measured 3 times for each of the three samples collected

Cementation

- Measure Vs
- Prepare enough treatment solution for experiments (0.8 L each column ~ 2 PVs)
    - Prepare an extra 100mL solution to avoid sucking air bubbles when treating
    - 2 columns with DI (0.8 L+0.1L) and lab-grade chemicals
    - Chemical amounts found in *Recipe Spreadsheet*
    - Make sure to add calcium chloride first and place it in a cold-water bath to dissipate heat, as it is an exothermic reaction, to prevent catalyzing urea hydrolysis
    - No yeast extract on the first cementation because it is already in the augmentation injection. Yes, yeast for the following cementations.
    - Check pH
- Obtain a 2 mL sample of treatment solution (baseline condition)
    - Check Urea content. It might be good to understand if something goes wrong.
- Dump out effluent that has been collected in the reservoir

- Pump treatment solution from the bottom up through the sample
    - Sample flow rate as augmentation, 10 ml/min
    - 15 minutes for DSS
- Take an aqueous sample of fluid estimated to be in the middle of the sample as it is pumped out
    - Note effluent volume
    - Freeze for later measurements
        1. For urea and pH measurements (2 mL sample total – 1x)
        2. Take the pH of the samples
        3. Follow the *Urea Cuvette Protocol* to measure urea content
            - Ideally, perform OD_{422} instead of cuvette
- Measure Vs again
- Wait 18 hours and repeat the process until target ΔVs is achieved. (12-24 hours is also okay depending on the activity rate of the bacteria).

Saturation

- Check if upstream tubes need to be replaced to eliminate loose calcite in the lines
    - This never had to be done as the tubes did not clog.
- Prepare 800ml (2PV?) per column DI de-aired water
- Saturate at a constant flow rate

Sharing

- Consolidation (same as with uncemented samples)
- B-Value check (same as with uncemented samples)
- Loading (same as with uncemented samples)

After Testing

- Dry specimen
    - Cut the specimen into seven sections and place on a baking sheet
    - A visual inspection of the intact cementation can be performed by poking the specimen
- From each dried specimen section, homogenize the material and select samples for calcite content measurements
- Follow the *Calcite Chamber Procedure* and *Waste Containers* protocol to perform calcite content

Measuring Shear Wave Velocity

- The waveform should be set to a square wave with a 0.1 ms period
- Shear wave velocity should be stacked until the signal noise is small (usually 10-30 stacks separated by 0.1-1 seconds apart

Augmentation Injection Solution									
2L DI or 4 pore volumes per column									
Chemical	Concentration (mM)	Molar mass (g/mol)	Mass needed for Single Batch (g)	Mass needed for Double Batch (g)	Mass measured (g)	Mass measured (g)	Mass measured (g)	Mass measured (g)	Mass measured (g)
Batch Type					Single Double	Single Double	Single Double	Single Double	Single Double
Urea	10	60.06	0.60	1.20					
Ammonium Chloride	100	53.49	5.35	10.70					
Yeast Extract (g/L)	0.2	-	0.20	0.40					
Bacteria Pellet	-	-	Pellets	Pellets					
Ph	-	-	-	-					

Cementation									
560 ml or (2PV + 100ml) per specimen									
Chemical	Concentration (mM)	Molar mass (g/mol)	Mass needed for Single Batch (g)	Mass needed for Double Batch (g)	Mass measured (g)	Mass measured (g)	Mass measured (g)	Mass measured (g)	Mass measured (g)
Batch Type					Single Double	Single Double	Single Double	Single Double	Single Double
Urea	250	60.06	8.41	16.82					
Ammonium Chloride	100	53.49	3.00	5.99					
Yeast Extract (g/L)	0.2	-	0.11	0.22					
Calcium Chloride	250	110.99	15.54	31.08					
Ph	-	-	-	-					

Cementation									
560 ml or (2PV + 100ml) per specimen									
Chemical	Concentration (mM)	Molar mass (g/mol)	Mass needed for Single Batch (g)	Mass needed for Double Batch (g)	Mass measured (g)	Mass measured (g)	Mass measured (g)	Mass measured (g)	Mass measured (g)
Batch Type					Single Double	Single Double	Single Double	Single Double	Single Double
Urea	100	60.06	3.36	6.73					
Ammonium Chloride	100	53.49	3.00	5.99					
Yeast Extract (g/L)	0.2	-	0.11	0.22					
Calcium Chloride	100	110.99	6.22	12.43					
Ph	-	-	-	-					